LINEAR AND NONLINEAR ELECTRO-OPTICS IN A SEMICONDUCTOR

by

Haipeng Zhang

B.A., Electrical Engineering, South China University of Technology, 2006
M.S., Electrical Engineering, University of Colorado, 2010

A thesis submitted to the
Faculty of the Graduate School of the
University of Colorado in partial fulfillment
of the requirement for the degree of
Doctor of Philosophy
Department of Electrical, Computer, and Energy Engineering
2012

This thesis entitled:
Linear and Nonlinear Electro-optics In a Semiconductor
written by Haipeng Zhang
has been approved for the Department of Electrical, Computer, and Energy Engineering

____
(Prof. Steven T. Cundiff)

____
(Prof. Rafael Piestun)

Date_______________

The final copy of this thesis has been examined by the signatories, and we
Find that both the content and the form meet acceptable presentation standards of scholarly work
in the above mentioned discipline.

Zhang, Haipeng (Ph.D., Electrical Engineering)
Linear and Nonlinear Electro-optics In a Semiconductor
Thesis directed by Professor Steven T. Cundiff

Numerous investigative efforts have been made to study the properties of semiconductor materials, which are the foundation of modern electronics. In this dissertation, we study semiconductor electro-optics in both linear and nonlinear regimes. Three main topics are presented. First, we describe transverse electroreflectance (ER) and electroabsorption (EA) experiments using a rapidly oscillating radio-frequency (RF) bias and electrodes that are insulated from the semiconductor sample. This technique produces an effectively uniform transverse electric field in a metal-semiconductor-metal structure. Then a pulsed terahertz emitter that uses the RF biasing technique is described. The effectively uniform electric field generated by the RF technique allows excitation of a large laser spot, lowering the photo-excited carrier density for a given pulse energy and increasing the efficiency of terahertz generation. The last part focuses on quantum interference control in a semiconductor. Measurement of ballistic current injection and coherent control of the photo-excited carrier density through the interference of one- and two-photon absorption in the presence of a static electric field, are described. These experiments and results provide better understanding of electro-optical properties in semiconductor materials.

Acknowledgements

First I am deeply grateful to my adviser, Professor Steven Cundiff, for providing tremendous support and encouragement through my graduate career. I thank him for giving me such a great opportunity to explore exciting science in his wonderful labs and for offering thoughtful and patient guidance.

I am very thankful to Professor Rafael Piestun, as well as Professor Daniel Dessau, Professor Juliet Gopinath, and Professor Robert McLeod, on my thesis committee, for their support and advices.

I would like to thank all the group members of the Cundiff lab, past and present, for their precious friendship and enormous help. Particularly I thank Jared Wahlstrand, for guidance early in my career as a graduate student, for teaching me valuable knowledge and techniques in lab, and for his proof-reading help and encouragement with this thesis. I'm also grateful to SooBong Choi, Xingcan Dai and Alan Bristow, for helpful discussion and guidance.

I also owe a great debt of gratitude to the JILA shop staff. I would like to especially thank David Alchenberger for his support in clean-room facilities and sample preparation, as well as Terry Brown and Paul Beckingham, for their help in building custom circuits and electronic devices.

Finally, I express my gratitude to my parents and my beautiful fiancée Boya, for their love and support.

Contents

Chapter

Appendix

Figures

Figure

CHAPTER 1

Introduction

The research presented in this thesis goes under the general heading of 'linear and nonlinear optical properties of a semiconductor.' This field, which has been studied extensively during the past fifty years, encompasses the study of light-matter interaction in a semiconductor. The subfield concerns the optical properties of a semiconductor in the presence of a strong electric field that changes slowly compared with the optical duration. The set of experiments described in this thesis focused on three main topics: field induced change in reflectivity or absorption in gallium arsenide (GaAs), photoconductive generation of electromagnetic radiation in terahertz (THz) frequency range, and nonlinear optical coherent control of photocurrent and carrier density.

1.1 Electroreflectance and electroabsorption based on Franz-Keldysh effect

Electroreflectance (ER) and electroabsorption (EA) based on the Franz-Keldysh effect are widely used characterization techniques for semiconductor materials. A modulated electric field induces a resonance in the differential reflectance or absorption spectrum for photon energies near the band structure critical point of a semiconductor. To give a rough physical picture, when the electric field is applied, the electron- and hole-wavefunctions turn into Airy functions rather than plane waves. The interference between electron- and hole-wavefunctions leads to oscillations in the reflectance or absorption spectrum. This effect is named after the German physicist Walter Franz and Russian physicist Leonid Keldysh, who developed theories of it nearly simultaneously [1,2].

There have been two periods of intense interest in the Franz-Keldysh effect. The first was around 1966–1974 during the development of modulation spectroscopy (ER and EA), and the second occurred in the late 1980's when modulation spectroscopy and analysis of Franz-Keldysh oscillations was applied to the study of heterostructures. Practically, ER and EA are used to find the band structure critical points and/or determine the effective mass of a semiconductor. EA modulators based on the Franz-Keldysh effect are also widely used in today's optical communication systems. In previous studies, a variety of techniques have been developed for ER and EA experiments. Among these techniques, one of the most commonly used was Schottky barrier ER [3,4] introduced by Aspnes. The bias is applied between a doped semiconductor substrate and a transparent electrode on the surface. Later the Schottky barrier technique was replaced by experiments using heterostructures to produce a more uniform electric field. Another widely used technique is called electrolyte ER, which uses the interface between a doped semiconductor and a liquid electrolyte [5]. People also developed a photoreflectance technique which relies on the screening of the surface field of a semiconductor by photocarriers [6]; this technique requires no electrical contacts. Another important technique is transverse ER or EA with a bias voltage modulated symmetrically about ground in order to have a uniform electric field, introduced by Rehn and Kyser [7], which has the advantage of enabling studies of the polarization dependence of the optical field with respect to the static electric field.

A transverse biasing scheme is required to do interesting nonlinear experiments, e.g., coherent control of carrier population [8]. However, the electric field distribution in the transverse M-S-M (metal-semiconductor-metal) structure is not uniform as expected. Since ER and EA are perfect tools for characterizing the field uniformity, in this thesis research, we studied both ER and EA in the transverse geometry. The ER and EA results from a GaAs sample with transverse electrodes and DC bias reveal a highly nonuniform electric field distribution due to carrier-trapping defects [9]. We developed a novel technique that uses a rapidly oscillating bias with a frequency near half the laser repetition rate and a sample with insulated electrodes. The technique produces an effectively uniform electric field under relatively high illumination (up to 160mW average optical power), and is very useful in ultrafast experiments that require a uniform transverse electric field, examples will be discussed in Chapter 4 and 5. Because it allows the study of materials with relatively high conductivity, the technique might find use in modulation spectroscopy as well.

1.2 Photoconductive terahertz generation

The use of ultrashort laser pulses for the generation and field-resolved detection of electromagnetic pulses in the terahertz (THz) frequency range has gained widespread popularity in recent years due to the wide range of applications in science and technology [10,11,12,13]. This technique has provided powerful tools for a variety of applications, including THz time-domain spectroscopy (THz-TDS), high speed device characterization, THz imaging [12,14] and ranging [15]. Electromagnetic radiation in the THz range has several distinct advantages: the THz radiation can penetrate a wide range of non-conducting materials, it is safe for biological tissues because it is non-ionizing (i.e. much safer than X-ray), and images formed with THz radiation can have relatively good resolution compared with microwaves. Furthermore, many materials have unique spectral fingerprints in the THz frequency range, which makes THz radiation especially useful for medical imaging and security scanning. The special frequency range of the THz radiation also allows for measurements on materials that are difficult to probe. For example, by using reflections from buried interfaces, defects in electronic devices can be found and imaged precisely.

There are two commonly used techniques for generation of THz radiation based on using ultrashort laser pulses. One is optical rectification, which based on the fact that when short optical pulses pass through a nonlinear crystal (such as ZnTe or GaP) they will induce electrical polarization proportional to the intensity, and the transient polarization is the source of THz radiation [16,17,18]. The other technique, photoconductive THz generation, usually uses a metal-semiconductor-metal (M-S-M) structure that is biased with an electric, and sometimes also a magnetic, field. The laser pulses illuminate the semiconductor and give rise to a current transient that leads to electromagnetic radiation in THz frequency range [19,20,21]. Of the two methods, optical rectification has the advantage of simplicity compared to the photoconductive emitter. However, under the same illumination power, the peak THz field generated from optical rectification is usually smaller than that from the photoconductive emitter.

For the second project in this thesis (discussed in Chapter 4), we used the RF biased M-S-M structure as a THz photoconductive emitter. In the past few years, the saturation of THz power from a photoconductive emitter with increasing illumination power has been studied [22,23]. The key limitation of the optical power-to-THz conversion efficiency is ultrafast screening of the applied electric field by photo-injected carriers [23]. In our experiment, we adopted the RF bias system and the insulated electrode sample that were used to generate an uniform transverse electric field in our previous ER experiment [24]. The uniform field obtained from the RF technique allows us to improve the power saturation threshold by using a large excitation spot, and thus promises better THz generation efficiency.

1.3 Coherent control of current injection and carrier density

Photocurrent can be generated in a semiconductor not only by driving optically injected carriers with an external DC bias, but also by direct optical injection. A carrier population can be optically injected into an undoped and unbiased bulk semiconductor through two different pathways connecting the same initial and final states (i.e. through one- and two-photon absorption), and the quantum interference between the two pathways gives rise to an asymmetric distribution of photocarriers in k-space, which leads to a ballistic charge current. This effect, predicted [25,26] and experimentally demonstrated [27,28] in the 1990's, is known as quantum interference control (QUIC). These optically driven currents have proven useful in studying ultrafast current relaxation processes [29,30]. Under certain conditions this QUIC technique can generate even ballistic spin-polarized currents [31]. By measuring the QUIC current injection in a semiconductor device, the carrier-envelope-phase offset frequency of a mode-locked Ti:sapphire laser can be detected [32,33] and stabilized [34,35], an important application for optical frequency metrology.

A two-color excitation scheme was used in the early experiments [27,28] to generate photocarriers through one- and two-photon absorption in an unbiased GaAs sample. The quantum interference between the one- and two-photon absorption processes, which connect the same initial and final states in the valence and conduction bands, leads to an asymmetric distribution of carriers in k-space. By controlling the relative phase between the two-color excitation pulses (with frequency ω and 2ω), one can arrange for constructive interference in one direction in k-space and destructive interference in the opposite direction. This leads to a ballistic current whose sign and amplitude can be coherently controlled by adjusting the relative phase of the ω and 2ω pulses [27,28]. Typically low-temperature grown GaAs (LT-GaAs) is preferred for QUIC current injection due to its subpicosecond carrier lifetime. Short lifetime prevents internal discharge of the charge built up by the QUIC current [28], and thus helps improve the signal-to-noise ratio. In this dissertation, we use a similar two-color excitation scheme to measure the ballistic current injection in an erbium-doped GaAs (GaAs:Er) which has a short carrier lifetime comparable with that of LT-GaAs, and show that the QUIC signal size from the GaAs:Er is the same order of magnitude as from a low-temperature grown GaAs.

For coherent control of ballistic current, the ω and 2ω fields only modify the distribution of photocarriers in k-space, without changing the total number of carriers. In contrast, in a process arising from the imaginary part of the second-order nonlinear susceptibility $\chi^{(2)}$, the ω and 2ω fields can also be used to change the total density of carriers, rather than their k-space distribution, allowing coherent control of the overall carrier density. By using phase controlled optical pulses with frequency ω and 2ω and a (111)-oriented bulk GaAs sample, Fraser *et al.* showed [36,37] that the photo-injected carrier density can be controlled coherently through quantum interference between the transition amplitudes associated with one-photon absorption of 2ω and two-photon absorption of ω connecting the same initial valence band and final conduction band states.

In this thesis, we demonstrate that a constant electric field can convert the always present third order nonlinear susceptibility $\chi^{(3)}$ to an effective $\chi^{(2)}$, which enables coherent control of carrier population without requiring a non-zero $\chi^{(2)}$. We present experimental results from both an all-optical pump-probe measurement and with electrical detection.

1.4 Thesis organization

This dissertation includes 6 chapters. The next chapter, Chapter 2, gives an introduction to the radio-frequency (RF) bias and detection technique, which is a general technique that encompasses most of the experiments of this thesis. First the transverse M-S-M structure and the non-uniform electric field distribution in this geometry is discussed. Then a description of our RF bias technique that uses a rapidly oscillating bias across electrodes insulated from a GaAs sample is given. The resulting uniform field distribution is essential for most of the experiments described in the following chapters.

Chapter 3 is focused on electroreflectance (ER) and electroabsorption (EA) experiments. First an introduction is made to the Airy function theory based on parabolic band approximation for Franz-Keldysh effect. Then a description of the experimental setup and results for ER experiments in bulk semi-insulating GaAs (SI-GaAs) is given, for both DC bias and RF bias techniques. The results indicate that by using the RF bias technique we can achieve a uniform field distribution in the transverse M-S-M structure. EA experiments and results from a thin GaAs epilayer are also discussed.

Chapter 4 discusses terahertz (THz) generation from a photoconductive emitter. A brief introduction to photoconductive THz generation from bulk GaAs and electro-optic sampling detection is given first, following by a review of the limiting factor of the THz generation efficiency: the ultrafast screening of the applied bias. Then our RF technique for THz generation, which improved the generation efficiency by minimizing the carrier screening effect, is discussed in detail. The results are also compared with the conventional DC bias THz emitter. In addition, results of THz generation from an LT-GaAs sample are also presented.

Chapter 5 is concerned with the coherent control of ballistic current and the overall carrier density. We start with an introduction to quantum interference control and $\chi^{(2)}$-enabled population control, following by a theory which predicts electric field-induced population control. Then measurements of field-induced population control, including the all-optical pump-probe scheme, and the electrical measurement, are presented. The experimental results of ballistic current injection via QUIC in an erbium doped GaAs are also included.

Chapter 6 summarizes the thesis and offers a brief discussion of future work. Several appendices follow, containing additional information about the RF technique and sample preparation that are not covered in the main text.

CHAPTER 2

Radio frequency (RF) bias and detection technique

To provide a basic understanding of the most important experimental technique in this thesis, an overview of the RF bias and detection technique is presented in this chapter. First we start with an overview of the physics of semi-insulating GaAs (SI-GaAs) with a transverse electrode geometry, in particular the highly non-uniform electric field distribution, the so called 'trap-enhanced electric field,' found when a bias is applied across this structure. This overview is followed by a description of our sample with an insulating layer (SiO_2) between the SI-GaAs surface and metal electrodes. The purpose of using this special sample structure is to achieve a more uniform field distribution. Furthermore, ultrafast carrier screening of the applied electric field is discussed. Finally, our RF bias and lock-in detection system is presented; the rapidly oscillating bias field enables the production of an effectively constant field in ultrafast optical experiments.

2.1 Background and motivations

The electro-optical properties of semiconductor materials have been studied for several decades. It has been found that the electric field induced change in the absorption or reflectivity spectrum of a semiconductor has peaks near band structure critical points. Thus, by modulating an applied DC field and measuring the change in the absorption or reflectivity spectrum using phase-sensitive (lock-in) detection techniques, one can learn about the band structure of materials. These techniques are known as electro-absorption or electro-reflectance. A variety of techniques have been developed to generate and modulate electric fields in a semiconductor.

One of the most commonly used techniques involves using the built-in electric field in the depletion region of a doped semiconductor (e.g. GaAs) [3,4]. Contact between a transparent metal film and a doped semiconductor can produce a Schottky barrier, and by applying a bias between the doped semiconductor substrate and the electrode, one can obtain a strong and uniform electric field in the thin depletion layer. In the 1980s, the Schottky barrier technique was improved in experiments in which a heterostructure is grown with an intrinsic layer surrounded by thin doped layers [38]; this produces a more uniform electric field. As will be shown in the next three chapters, producing a uniform electric field is essential for many ultrafast experiments. Typically electro-reflectance experiments are performed in this longitudinal geometry, with a constant built-in depletion field parallel to the optical wave vector.

Another way to apply bias is known as the transverse electrode geometry [7,39,40,41]; it was first reported by Rehn and Kyser [7]. In this geometry, two widely spaced (typically a few hundred μm) metal electrodes are both on the same side of a semiconductor (GaAs) surface, and thus the applied electric field is perpendicular to the light wave vector. Although this scheme is less common than using longitudinal electrodes, this transverse geometry offers the following advantages: (1) it is relatively easy to fabricate, with no need for transparent electrodes; (2) one can vary the polarization of the optical field with respect to the electric field direction; (3) it can be used with an undoped semiconductor. There are a few disadvantages: (1) high voltage is required because of the relatively large separation between electrodes; and (2) the field distribution in GaAs with metal electrodes deposited directly on the surface has been found to be strongly nonuniform [9]. As will be described in this thesis, the ability to generate a uniform electric field along the optical field enables a variety of different experiments on electroreflectance (ER), electroabsorption (EA), THz generation, and coherent control. In the following parts of this chapter, the physics of the field distribution and our technique for achieving a uniform field in a transverse electrode GaAs sample will be discussed in detail.

2.1.1 Introduction to trap-enhanced electric field

Enhanced electric field near the anode edge of a metal-semiconductor-metal (M-S-M) structure, the so-called ‘trap-enhanced electric field’, was first reported in a terahertz generation experiment [9]. Photoconductive antennae based on M-S-M structures have been used as sources of terahertz (THz) radiation for almost three decades. Physically, THz emission from a photoconductive antenna relies on the light-induced conductivity change in a biased semiconductor substrate. Creation of photocarriers by an ultrashort optical pulse leads to a current transient in the biased M-S-M structure that gives rise to a single-cycle electric field transient with a temporal length of less than a picosecond, which corresponds to a broad frequency spectrum extending into the THz frequency range. THz spectroscopy allows the study of a variety of applications, including chemical detection.

Enhanced THz radiation near the positive biased electrode edge (the anode) has been found in previous studies of THz generation using GaAs M-S-M structures [42]. Terahertz radiation 50 times stronger can be obtained from illumination near the anode than from illumination near the cathode [42]. As shown in Figure 2.1, our measurement of the peak electric field of the THz pulse as a function of illumination position from a GaAs M-S-M structure (DC biased) shows strong enhancement of THz electric field when the laser pulse is focused near the anode edge, which is consistent with a previous study by Ralph and Grischkowsky [9]. At modest bias voltages, they interpret the enhanced THz signal as most of the applied potential drops within a few microns of the anode.

Detailed study and modeling showed that the strong electric field enhancement at the anode of the transverse M-S-M structure is due to carrier-trapping impurities [9,43]. The origin of the field inhomogeneity can be traced to the fabrication process of SI-GaAs. Typically SI-GaAs substrates are taken from liquid encapsulated Czochralski grown ingots, and the semi-insulating character comes from a careful balance between the residual shallow acceptor impurities and the so-called EL-2 donor defects. The EL-2 is a deep donor found in GaAs with excess As concentration, and the surplus As atoms are found to occupy Ga host lattice sites, forming antisites, As_{Ga}. These defects, at a concentration of around 10^{16} cm^{-3}, have the ability to fully compensate moderate concentrations of acceptors (around 10^{15} cm^{-3}) which results from the unintentional doping with carbon. Thus in SI-GaAs, the charge density is determined by the EL-2 defect and the residual acceptors. Normally the shallow acceptors are fully ionized, but the deep EL-2 donor can be partially ionized, and always acts as a strong electron trap [9].

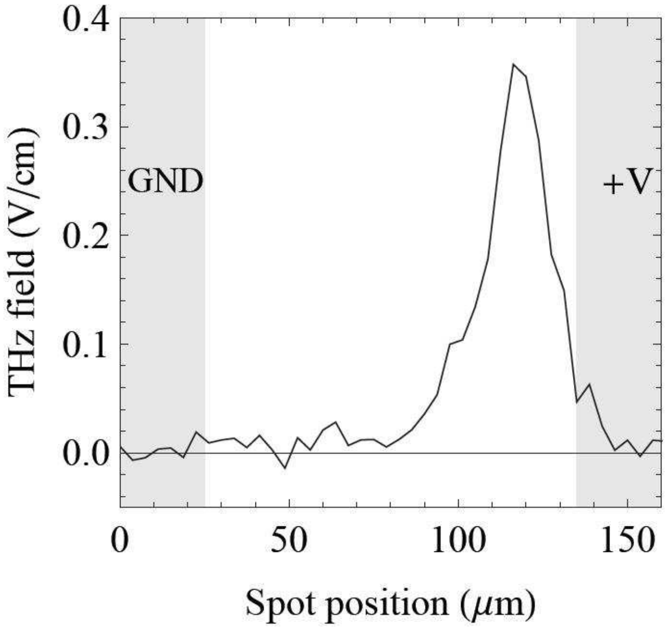

Figure 2.1: Measured THz signal in SI-GaAs with electrodes on the surface as a function of illumination position for an electrode bias of 40 V. Details of this measurement will be described in Chapter 4.

In the transverse M-S-M geometry used in most THz experiments, metal electrodes are in direct contact with the SI-GaAs surface; when a bias is applied electrons are readily injected from the cathode. Injection of free carriers under a moderate bias leads to an accumulation of electrons and a depletion of holes near the anode edge, which is strongly affected by electron velocity saturation and geometric effects [9]. A schematic plot for the carrier-injection process in a transverse M-S-M structure is shown in Figure 2.2.

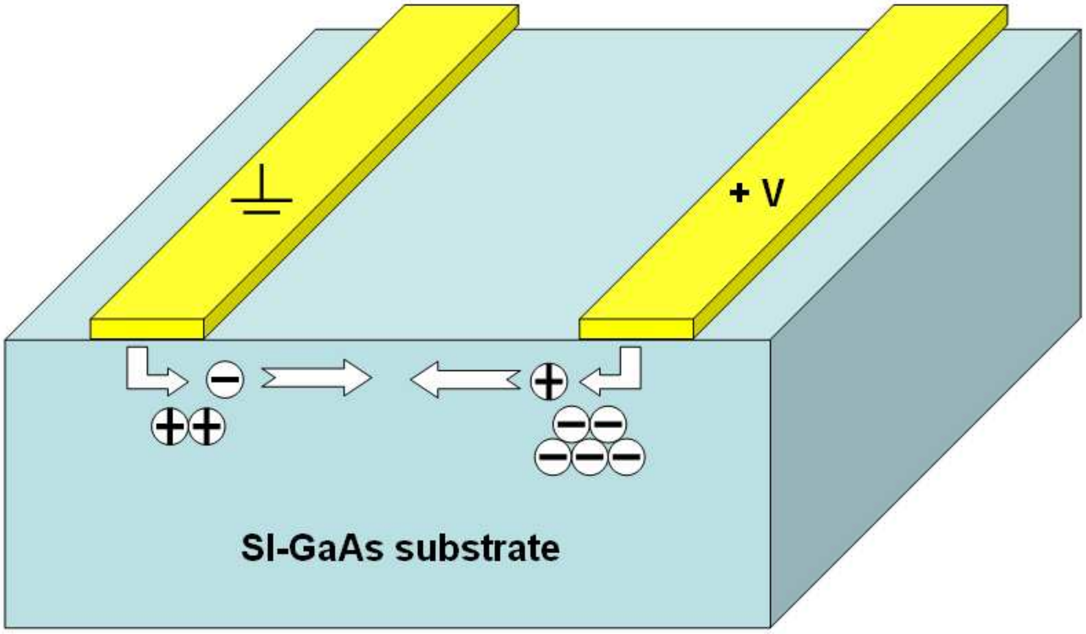

Figure 2.2: Schematic of carrier-injection in a biased metal-semiconductor-metal (M-S-M) structure. Electrons accumulate near the cathode.

Although the free carriers are not sufficient to directly change the field distribution significantly because of their relatively low density, it has been shown that a small change in free carrier density results in a large change in trap occupancy. With increasing electron density near the anode, the EL-2 traps which have a larger capture cross section for electrons than holes, tend to become almost fully occupied by electrons and thus become charge neutral. Without compensation from the EL-2 traps, the ionized acceptors form a space-charge region which only depends on the net acceptor concentration. In this space-charge region, which is known as the trap-enhanced electric field (TEF), the field strength can be enhanced by factor of a few hundred compared to the rest of the gap between electrodes [9].

In contrast, the cathode experiences only small electron depletion, since electrons can be readily injected from the electrode. Furthermore, the accumulation of holes near the cathode is small due to the fact that hole velocity saturation requires a stronger field. Thus, a space charge region which can strongly affect field distribution doesn't exist near the cathode.

2.1.2 Transverse sample geometry with insulated electrodes

The large trap-enhanced fields just described enable efficient THz generation with low optical excitation level, but many experiments, e.g., field-induced population control and THz generation experiments discussed in Chapter 4 and 5, would benefit from having a uniform electric field in the M-S-M structure. The highly inhomogeneous TEF near the positive biased electrode in semi-insulating materials limits applications, e.g., field inhomogeneity will wash out the Franz-Keldysh oscillations which will be discussed in Chapter 3. In order to achieve a uniform field distribution in transverse electrode geometry, we developed a technique which does not require electrical injection of carriers into the semiconductor, preventing the TEF from forming.

There are two types of sample structures we used in our experiments. Shown in Figure 2.3 (a) is the sample mainly used in electroreflectance and THz generation experiments (discussed in Chapter 3 and 4, respectively). We first evaporate a 100 nm thick layer of silicon dioxide on the SI-GaAs surface as an insulating layer, and then Ti:Au electrodes of roughly 200 nm thickness are patterned on top of the insulating layer using photolithography. The electrodes are separated by a 100 μm gap. Figure 2.3 (b) shows the thin sample used in the coherent control experiment, discussed in Chapter 5. Ti:Au electrodes of roughly 200 nm thickness are evaporated on a transparent sapphire disk first using photolithography, and then a 1 μm thick SI-GaAs epi-layer is attached to the sapphire disk by transparent wax. The wax also acts as a insulating layer between the metal electrodes and the sample. As discussed in the previous section, when free carriers are injected from the electrodes, TEF forms from uncompensated acceptors due to increasing occupancy of deep traps. Thus the deleterious effects of the traps can be avoided if the insulating layer between the electrodes and the SI-GaAs surface prevents free electrons from injecting into SI-GaAs.

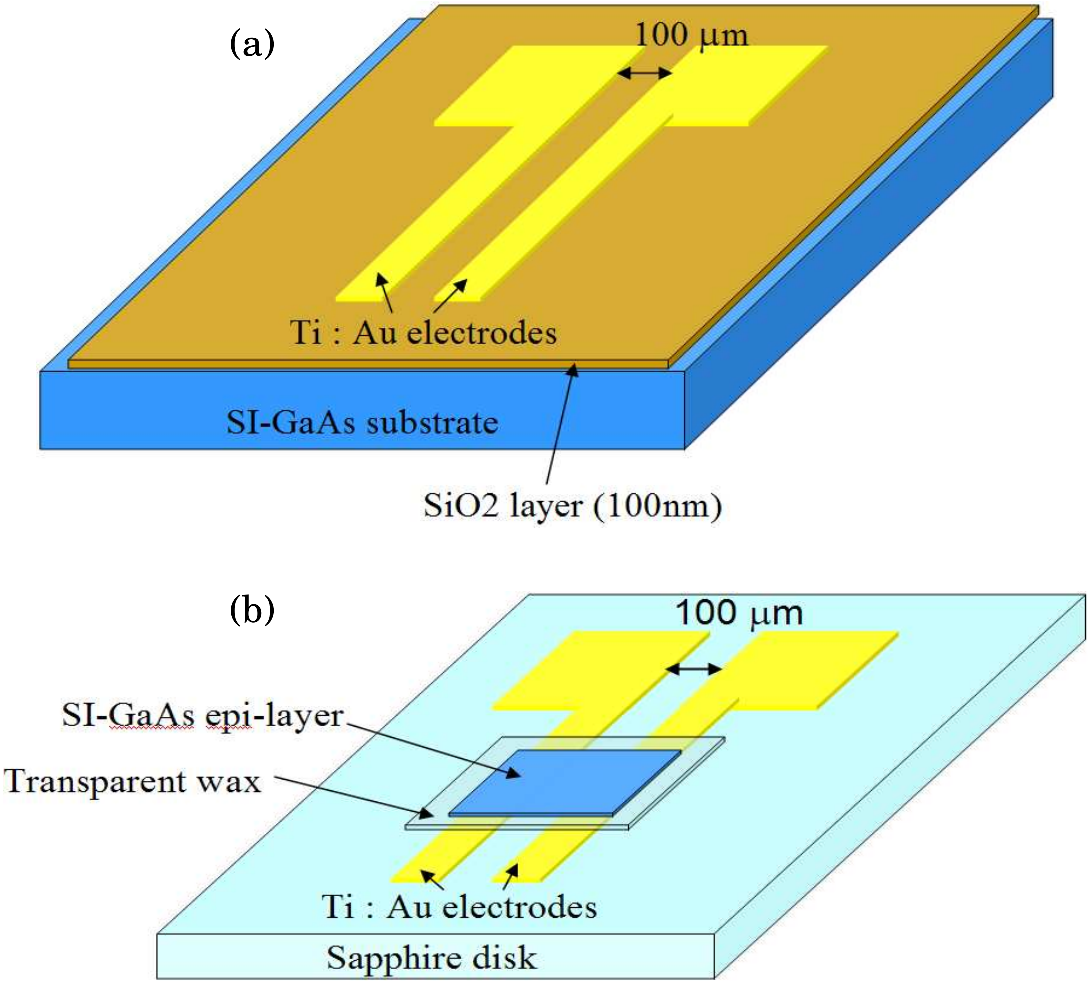

Figure 2.3: SI-GaAs sample with insulated electrodes. (a) Structure used in the electroreflectance and THz experiments. (b) Structure used in the coherent control experiment.

2.1.3 Photo-injected carrier screening of the applied electric field

In the experiments described in later chapters, the semiconductor is illuminated by a laser. The insulating SiO_2 layer prevents free-electron injection from the electrodes, yet it introduces a different problem – screening of the applied electric field by photoexcited carriers. Since the metal electrodes are insulated from the SI-GaAs surface, photoexcited electron-hole pairs can not be swept out by the electrodes, and they are confined inside the SI-GaAs substrate; the photoinjected electrons and holes will be separated by the applied bias field, building up an internal field which cancels out the external one in a process known as Coulomb screening.

The screening time is roughly equal to the dielectric relaxation time in GaAs. The dielectric relaxation time can be derived from the Poisson equation. For a small disturbance of charge density $\Delta N(t)$ in the charge equilibrium of a semiconductor, from the Poisson equation,

$$\frac{dE}{dx} = -\frac{\Delta N(t)}{\varepsilon\varepsilon_0}, \tag{2.1}$$

where $\varepsilon\varepsilon_0$ is the dielectric permittivity of the medium. The continuity equation gives

$$\frac{\partial(\Delta N(t))}{\partial t} = \nabla \cdot J = \mu N \frac{\partial E}{\partial x}. \tag{2.2}$$

Here, because we are treating the case of quasi neutrality, we have neglected all terms in $\nabla \cdot J$ from the gradient in the carrier concentration (diffusion), N is the total carrier concentration, and μ is the carrier mobility. The rate of change of the disturbance in carrier density can be found from combining Eq. (2.1) and Eq. (2.2),

$$\frac{\partial(\Delta N(t))}{\partial t} = -\frac{eN\mu}{\varepsilon\varepsilon_0}\Delta N(t)\,, \tag{2.3}$$

which gives a simple solution

$$\Delta N(t) = \Delta N(0)\cdot\exp(\frac{t}{\tau_d})\,. \tag{2.4}$$

Here $\tau_d = \frac{\varepsilon\varepsilon_0}{Ne\mu} = \varepsilon\varepsilon_0\rho$ is the dielectric relaxation time and ρ is the resistivity. The time period over which screening occurs is roughly the dielectric relaxation time. Details of the geometry would also enter into a more sophisticated calculation. As the screening field is directly proportional to the photocarrier density ΔN, after an external field is suddenly turned on, the electric field inside the sample decays roughly exponentially at rate 1/ τ_d. A schematic plot is shown in Figure 2.4.

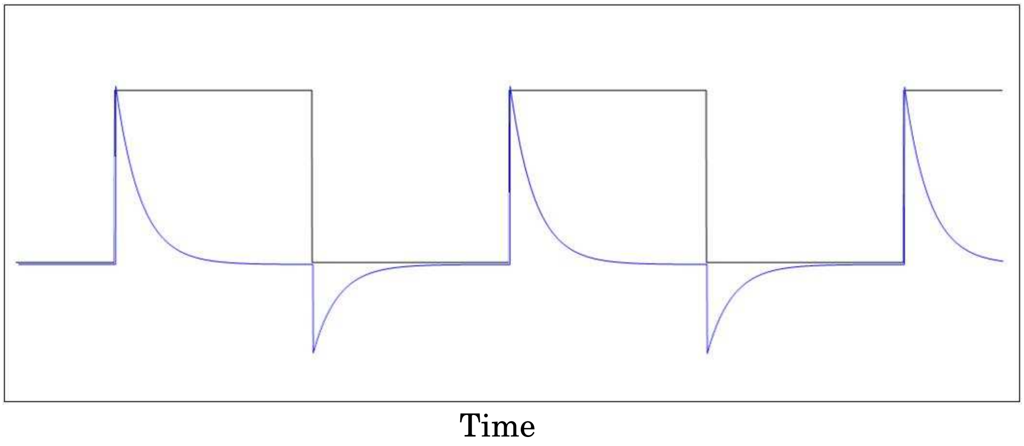

Figure 2.4: The applied bias field (black) and the actual field inside the SI-GaAs (blue) due to carrier screening.

Neglecting the dark resistivity (for SI-GaAs, this is typically on the order of $10^8 \Omega \cdot \mathrm{cm}$, which yields a dielectric relaxation time of $10^{-4} s$ [44]), $\rho = 1/[e \cdot (n\mu_n + p\mu_p)]$ is inversely proportional to the density of photoexcited carriers. Here for GaAs at room temperature, $\mu_n = 8500\ \mathrm{cm}^2/\mathrm{V} \cdot \mathrm{s}$ is electron mobility, and $\mu_p = 400\ \mathrm{cm}^2/\mathrm{V} \cdot \mathrm{s}$ is hole mobility. With increasing photocarrier density, ρ decreases, and the screening time is shorter. Thus the faster one modulates the bias field, the more light one can use before screening affects the experiment. At typically used modulation frequencies in the range of kHz (which are suitable for the highest-performing lock-in amplifiers), an extremely low illumination level is required (as well as high dark resistivity) [7,40], lowering the signal-to-noise ratio. A radio frequency bias enables measurement using stronger illumination, as well as enabling study of higher conductivity materials [45]. In the following section, we present the combination of RF bias and a synchronized train of short light pulses, which helps us to get an effectively uniform electric field (around 30 kV/cm), and makes experiments under much higher optical power (more than 100 mW on average) possible.

2.2 Radio frequency bias generation and synchronization with laser pulses

In order to avoid strong photo-excited carrier screening in our insulated electrode sample, a rapidly oscillating bias with modulation frequency in the radio frequency (RF) range is needed. A diagram of the RF bias generation apparatus is shown in Figure 2.5. Details of the apparatus, including the RF signal levels and parts used, are described in Appendix A.

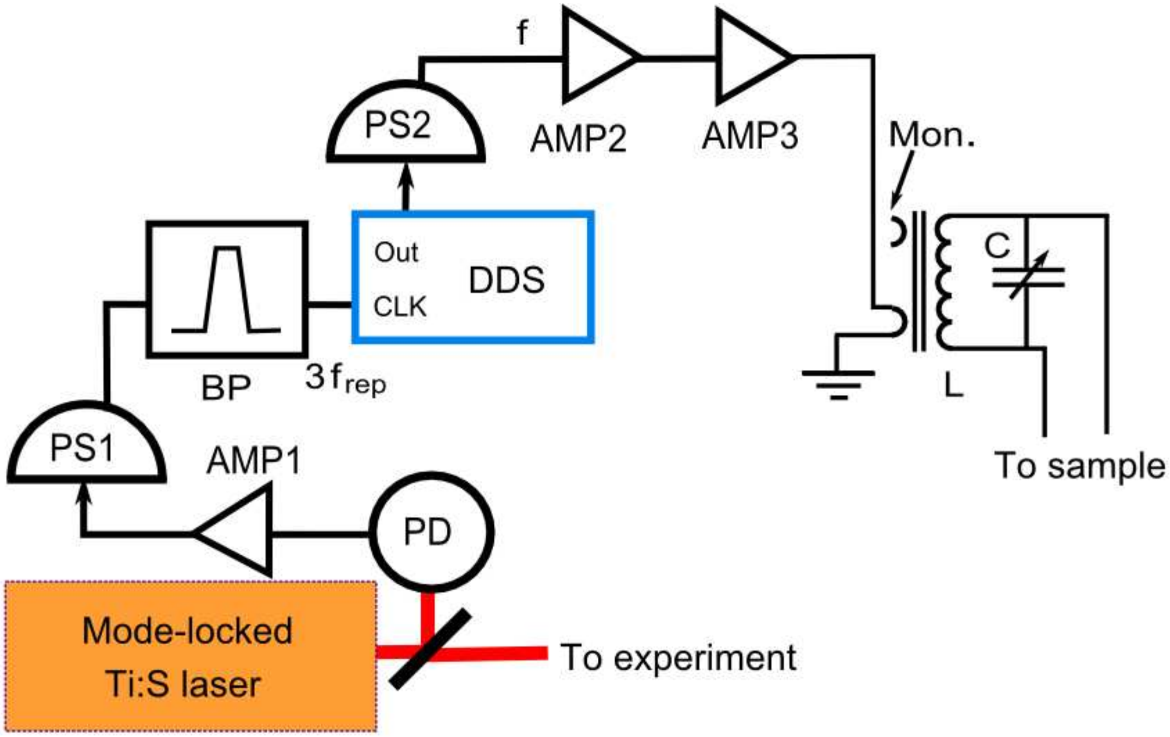

Figure 2.5: RF bias generation apparatus. The modulation frequency f is derived from the laser repetition rate f_{rep} using direct digital synthesis (DDS). An LC circuit enhances the voltage across the electrodes. BP: band pass filter, PD: photodetector, AMP: RF amplifier, PS: power splitter, and Mon.: monitor for tuning the circuit.

It will be shown below that to make detection of the signal in the experiments easier, it is desirable to oscillate the electric field at a frequency near the repetition rate of the laser. We use mode-locked Ti:sapphire lasers (for the field-induced coherent control case we use an optical parametric oscillator pumped by a Ti:sapphire laser) with repetition rate f_{rep} = 89 MHz (f_{rep} = 76 MHz for the pump laser in the field-induced coherent control experiment). First of all, a high speed photodetector is used to detect the Ti:sapphire laser harmonics. The output signal of the photodetector is then sent through a bandpass filter which passes only the third harmonic of the laser repetition rate ($3f_{rep}$). This $3f_{rep}$ signal is used as a clock for a direct digital synthesizer circuit (DDS), the output of which is a frequency of either f = f_{rep} + 1 kHz (for THz generation and field induced coherent control experiments) or $f = ½ f_{\mathrm{rep}} + 1$ kHz (for electro-reflectance experiment). The DDS requires the clock frequency to be at least three times the output frequency. A detailed analysis will be presented in the next section to explain the reason for choosing a different frequency f for electro-reflectance and THz generation experiments. The purpose of deriving f from f_{rep} by using a DDS circuit is to prevent drifting of the modulation frequency, which is the difference between f_{rep} and f, due to fluctuations in f_{rep}. For example, a 100 microns change in the laser cavity caused by mechanical vibration or thermal expansion can induce a 2.6 kHz drift of the laser repetition rate. Thus, if an independent frequency synthesizer were used to generate the bias, the reference frequency would drift by that much, which could lead to artifacts over a long scan. The DDS circuit synchronizes the signal f to the laser pulses and minimizes the drift between f and f_{rep}.

The DDS output is amplified and sent to the sample, where we use a resonant LC circuit which is driven by a 2 W RF power amplifier to enhance the voltage across the electrodes, as shown in Fig 2.5. The inductor is the secondary coil of an air-core transformer with $L = 1200$ nH. The capacitor is a sealed glass variable capacitor: for electro-reflectance, the LC resonance frequency is 44.5 MHz (close to ½ f_{rep} of the 89 MHz Ti:sapphire laser) and the capacitance is set to be $C = 7$ pF; for THz generation the LC resonance frequency is 89 MHz (close to f_{rep}), and $C = 2$ pF; and for coherent control the LC resonance frequency is 76 MHz (f_{rep} of the 76 MHz pump laser), and $C = 3$ pF. The sample contributes a few picofarad of additional capacitance. The secondary consists of 22 turns of 20 gauge magnet wire wound on a plastic toroid. The primary is a ¾ turn of the same wire. Another ¾ turn of wire is connected to an oscilloscope and the voltage across it, V_{mon}, is used as a monitor for tuning the resonance of the circuit. In order to minimize signal reflection, which prevents part of the RF signal from being transferred to the LC resonance circuit, the impedance of the transformer is tuned to match the 50 Ω output impedance of the RF amplifier by adjusting the position of the wires along the toroid. This position affects the reactance (imaginary part of the impedance) of the LC resonance by changing the parasitic capacitance between the wires.

2.3 Frequency mixing lock-in detection

In laser spectroscopy experiments, one often periodically modulates some parameter of the experiment and uses phase-sensitive detection to increase sensitivity and reduce background noise. For example, this can be done by using a mechanical chopper in the laser beam or by modulating the bias across the sample, and using a lock-in amplifier to measure the signal at the modulation frequency. In our system, we modulate the bias voltage across the sample sinusoidally at the frequency f, which is near the laser repetition rate f_{rep}. One could in principle use a lock-in amplifier capable of detecting in the RF frequency range, but they are not as sensitive and resistant to pickup noise as digital lock-in amplifiers in the audio frequency range. Thus we use a heterodyne technique to shift the effective modulation frequency to the audio frequency range, where photodetector circuits and lock-in amplifiers have the best performance. A diagram of the frequency-mixing lock-in detection scheme is shown in Figure 2.6.

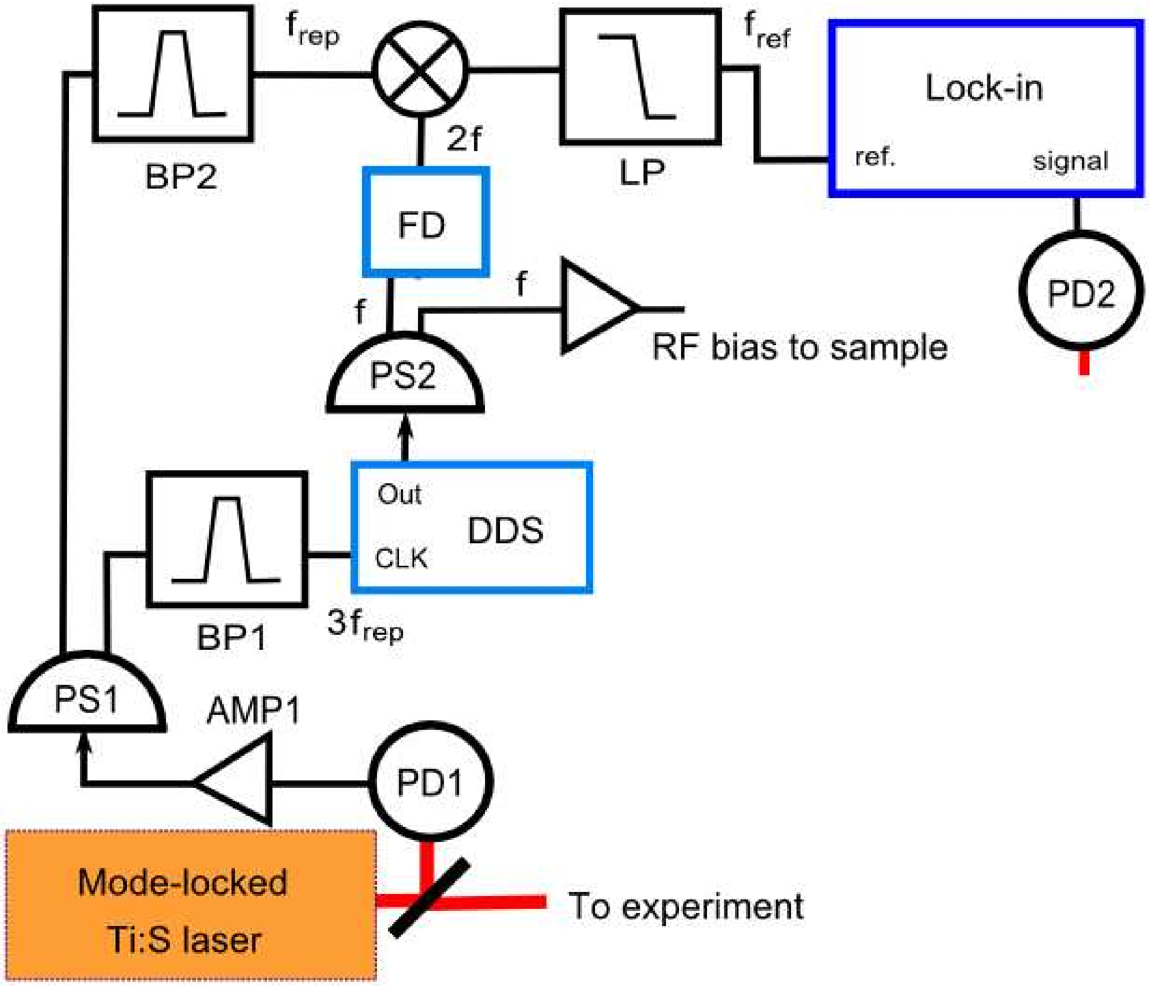

Figure 2.6: Frequency-mixing lock-in detection scheme. BP: band pass filter, AMP: RF amplifier, PS: power splitter, LP: low pass filter, FD: frequency doubler (only for electro-reflectance case), PD: photodetector.

The output of the high speed photodetector used to provide the clock for the DDS is split by a RF power splitter and then filtered. As discussed previously, part of the output, which selects $3f_{\mathrm{rep}}$, is used as the clock frequency of the DDS. The other part is filtered to select the fundamental harmonic of f_{rep}; this is mixed with part of the DDS output, which in some cases was doubled, to generate a reference frequency, $f_{\mathrm{ref}} = 2f - f_{\mathrm{rep}} \approx 1$ kHz (for electro-reflectance), or $f_{\mathrm{ref}} = f - f_{\mathrm{rep}} \approx 1$ kHz (for THz generation). It is proven below that the signal from a lock-in amplifier referenced to $2f - f_{\mathrm{rep}}$ (or $f - f_{\mathrm{rep}}$) is the same amplitude as that from a RF lock-in amplifier referenced to $2f$ (or f). With the advantages of not requiring mechanical chopping and a continuous, wide range of electronically selectable reference frequencies, this detection scheme combined with the RF bias technique could be useful in ultrafast experiments where detecting a signal modulated by a uniform electric field is required. On the other hand, if one only needs a constant field, the RF bias frequency can be set to be equal to the laser repetition rate. This is used in our field induced coherent control experiment which will be discussed in Chapter 5. Note that one must carefully adjust the phase between the laser pulse train and the bias waveform in order to achieve the optimum effective DC field strength. A diagram of the pulse train and bias field for this configuration is shown in Fig 2.7.

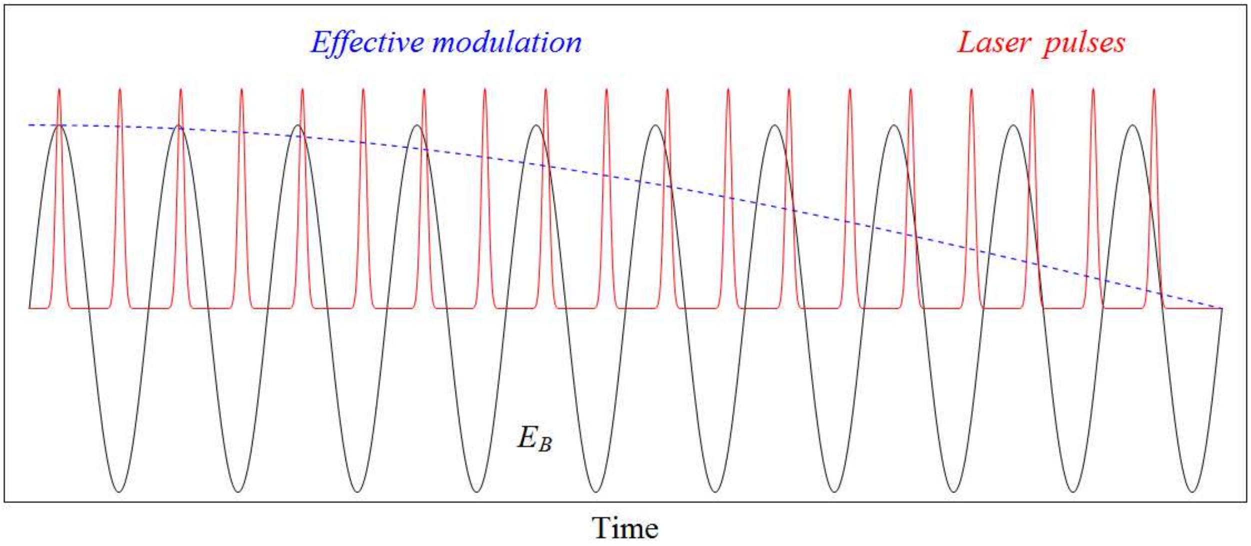

Figure 2.7: Bias field with frequency f synchronized with the laser pulses. Red: laser pulses. Black: RF bias. Blue: effective modulation of the bias.

For the case of electro-reflectance based on the Franz-Keldysh effect, at a given photon energy $\hbar\omega$ the differential reflectivity of the sample $\Delta R(E_{\mathrm{B}}, \hbar\omega) =$

$R(E_B, \hbar\omega) - R(0, \hbar\omega)$ is highly nonlinear in the electric field E_B from the bias (details will be given in the next chapter), but neglecting sign-dependent Franz-Keldysh effects that can occur in a noncentrosymmetric crystal under certain conditions [40], ΔR is even in the electric field, totally independent of its sign. Thus, a Taylor expansion of ΔR can be written as

$$\Delta R(E_B, \hbar\omega) = R_2(\hbar\omega)E_B{}^2 + R_4(\hbar\omega)E_B{}^4 + R_6(\hbar\omega)E_B{}^6 + \ldots.. \tag{2.5}$$

The modulated electric field is of the form $E_B(t) = E_0 \sin(2\pi f t)$. This expansion leads, for the first term in Eq. (2.5), to

$$\Delta R(E_B, \hbar\omega) \propto R_2(\hbar\omega)E_0^2 \sin^2(2\pi f t) = \frac{R_2 E_0^2}{2} - \frac{R_2 E_0^2}{2}\cos(2\pi \cdot 2 f t). \tag{2.6}$$

Thus the RF bias results in a DC change in the reflectivity and a modulated reflectivity signal at frequency $2f$. Higher order terms in Eq. (2.5) result in harmonics of $2f$.

The intensity of the laser beam on the photodetector I_{PD} is proportional to $R[E_B(t), \hbar\omega] \cdot I(t)$, where $I(t)$ is the intensity of the incident laser light. For a mode-locked laser with a repetition rate of f_{rep}, $I(t)$ can be written as

$$I(t) = \sum_{n=-\infty}^{\infty} I_0 \cdot \exp[\frac{-(t - \frac{n}{f_{rep}})^2}{\tau^2}] \tag{2.7}$$

Where τ is a laser pulse width parameter. Thus the light intensity on the photodetector is

$$I_{PD} \propto \Delta R[E_B(t), \hbar\omega] \cdot I(t)$$
$$= (R_2(\hbar\omega)E_B^2 + R_4(\hbar\omega)E_B^4 + R_6(\hbar\omega)E_B^6 + \ldots) \cdot \left\{ \sum_{n=-\infty}^{\infty} I_0 \cdot \exp[\frac{-(t - \frac{n}{f_{rep}})^2}{\tau^2}] \right\} \tag{2.8}$$

Taking a Fourier transform to the frequency domain and only considering the fundamental harmonic at 2*f* for the sake of simplicity, the Fourier transform of *I*(t) is a comb with lines centered at n·f_{rep}.

$$I_{PD}(\omega) \propto \int \left[\sum_{m=0}^{\infty} \tilde{I}_0 \exp\left(\frac{-(mf_{rep})^2}{v^2} \right) \delta(\omega' - 2\pi m f_{rep}) \right]$$
$$\times [\delta(\omega - \omega') - 0.5\delta(\omega - \omega' - 4\pi f) - 0.5\delta(\omega - \omega' + 4\pi f)] \cdot \exp(-i\omega t)dt$$
$$= \exp(-i\omega t) \cdot \{ \sum_{m=0}^{\infty} \tilde{I}_0 \exp\left(\frac{-(mf_{rep})^2}{v^2} \right) \delta(\omega - 2\pi m f_{rep}) - 0.5 \sum_{m=0}^{\infty} \tilde{I}_0 \exp(\frac{-(mf_{rep})^2}{v^2}) \delta(\omega + 4\pi f - 2\pi m f_{rep})$$
$$- 0.5 \cdot \sum_{m=0}^{\infty} \tilde{I}_0 \exp\left(\frac{-(mf_{rep})^2}{v^2} \right) \delta(\omega - 4\pi f - 2\pi m f_{rep}) \} \tag{2.9}$$

Here v is the laser spectral width. By the convolution theorem, the Fourier transform of I_{PD}(t) has a peak at 2*f* – f_{rep}. Thus if we choose *f* to be close to ½f_{rep}, for 2*f* slightly different from f_{rep}, the pulse train and bias waveform slip with respect to one another, leading to a reflectance signal at the difference frequency. Harmonics arising from terms $R_m(E_{\text{B}})^m$ in Eq. (2.4) lead to peaks at $m \cdot (2f - f_{\text{rep}})$. In principle, one could construct the constant-field spectrum using these harmonics, but in the experiments described in this thesis only the fundamental harmonic is used. The frequency 2*f* – f_{rep} is set in the audio frequency range as a reference for the lock-in amplifier.

For THz generation using an RF bias, the signal is approximately proportional to the bias field, because the THz field is detected through electro-optic sampling, as described in Chapter 4. We again use the heterodyne technique to shift the effective modulation, this time choosing f to be close to f_{rep}. In this case, for a given time delay between the pump and electro-optical sampling pulses, the THz field strength is

$$E_{THz}(t) \propto E_B(t) \cdot I(t) \tag{2.10}$$

where $E_{\mathrm{B}}(t)$ is the modulated electric field, and $I(t)$ is the intensity of the pump laser pulse train. Because of the difference between the laser repetition rate and the bias modulation frequency, the THz field is modulated in the time domain

$$E_{THz} \propto E_0 \sin(2\pi ft)\left\{\sum_{n=-\infty}^{\infty} I_0 \exp\left[\frac{-\left(t-\frac{n}{f_{rep}}\right)^2}{\tau^2}\right]\right\} \tag{2.11}$$

As before, take the Fourier transform to the frequency domain and use the convolution theorem:

$$E_{THz}(\omega) \propto \sum_{m=0}^{\infty} \tilde{I}_0 \exp\left(\frac{-(mf_{rep})^2}{v^2}\right)\delta(\omega - 2\pi m f_{rep})] * [\delta(\omega - 2\pi f) - \delta(\omega + 2\pi f)] \tag{2.12}$$

$$= \sum_{m=0}^{\infty} \tilde{I}_0 \exp\left(\frac{-(mf_{rep})^2}{v^2}\right)\delta[\omega - 2\pi(mf_{rep} + f)] - \sum_{m=0}^{\infty} \tilde{I}_0 \exp\left(\frac{-(mf_{rep})^2}{v^2}\right)\delta[\omega + 2\pi(f - mf_{rep})]$$

When we use the fundamental harmonic ($m = 1$), the second term on the right hand side of Eq. (2.12) is

$$\delta[\omega + 2\pi \cdot (f - m \cdot f_{rep})] = \delta[\omega + 2\pi \cdot (f - f_{rep})] \tag{2.13}$$

This shows that $E_{\mathrm{THz}}(\omega)$ has a peak at $f - f_{\mathrm{rep}}$. In this case we set f to be close to f_{rep}, and the reference frequency for lock-in detection is $f_{\mathrm{ref}} = f - f_{\mathrm{rep}}$.

For the field-induced coherent control experiment, the RF bias technique is used without requiring this heterodyne scheme for detecting the signal. Details of that experiment will be described in Chapter 5.

2.4 Summary

In this chapter, our experimental techniques for achieving a relatively uniform field in a SI-GaAs sample with a transverse electrode geometry were introduced. The uniformity of the field was proven by spatially resolved electroreflectance, as will be described in the next chapter. We utilize an insulating layer in order to minimize the trap-enhanced electric field by preventing carrier-injection from metal electrodes. Combined with a fast oscillating bias in the radio frequency range, which helps us minimize photo-injected carrier screening, we can achieve an effectively uniform field distribution in the transverse geometry. We also developed a heterodyne detection technique which can guarantee a good signal-to-noise ratio and a widely adjustable reference frequency without the requirement of a mechanical chopper.

This RF bias and frequency-mixing technique was applied to experiments such as electro-reflectance, THz generation, and field induced coherent control. Each of these experiments is discussed in the following chapters.

CHAPTER 3

Electroreflectance and electroabsorption based on Franz-Keldysh effect

In this chapter, we mainly focus on electroreflectance (ER) and electroabsorption (EA) spectroscopy based on the Franz-Keldysh effect. First we start with a brief introduction to bulk gallium arsenide (GaAs) and the theory of the Franz-Keldysh effect. Then results are discussed from a typical electroreflectance setup that uses a low frequency bias that is modulated in the kHz range and a pair of electrodes in direct contact with the semi-insulating GaAs (SI-GaAs) sample. One of the goals of the ER/EA experiments was to get very nice and clean experimental data with more observable Franz-Keldysh oscillations that could be compared to a sophisticated theory being developed in collaboration with John Sipe of the University of Toronto. However, it turned out to be much harder than we thought. We calculated the electric field distribution between electrodes based on a parabolic band approximation model, and found a strong trap-enhanced electric field near the anode edge as discussed in the previous chapter. The field nonuniformity washes out the Franz-Keldysh oscillations, which is the reason why we developed the RF technique, because it overcomes the trap-enhanced fields. We then present experimental results with RF bias ER, which uses a rapidly oscillating bias that is synchronized to the laser pulses. The bias generated by our RF technique is applied to SI-GaAs with electrodes electrically isolated from the sample surface, as described in Chapter 2. The measured electric field distribution proves that a uniform electric field can be achieved successfully by using our RF technique. More detailed studies of the bias voltage, optical power and polarization dependence of

ER signal are also described. ER under high optical power is also discussed. In the last part, electroabsorption results from a 1 μm thick GaAs epilayer are also discussed in detail.

3.1 Introduction

Gallium arsenide (GaAs), one of the most commonly used semiconductor materials in today's manufacture of electro-optic devices and microwave frequency circuits, is a direct bandgap III/V compound semiconductor with zinc-blende structure. In GaAs, near the Γ point of the Brillouin zone where $k = 0$, there is one conduction band and three valence band, all of them have parabolic dispersions. The conduction band is an electron band which has a positive curvature with respect to k, and the three valence bands are hole states which have a negative curvature. Two of the valence bands, the heavy hole (hh) and light hole (lh) bands, are degenerate at $k = 0$. The heavy hole band has a smaller curvature compares with the light hole band. The third valence band is split off to lower energy by the spin-orbit coupling, and is known as the split-off band. Bandgap energy E_g is defined as the energy difference between the minimum of the conduction band and the maximum of the valence band, at room temperature $E_g = 1.42$ eV.

In case of linear absorption where the incident photon energy $\hbar\omega$ is close to the bandgap energy of GaAs, the absorption coefficient α is directly proportional to the joint electron-hole density of states [6]:

$$\text{for } \hbar\omega < E_g\,,\ g(\hbar\omega) = 0\,, \tag{3.1}$$

$$\text{for } \hbar\omega \geq E_g\,,\ g(\hbar\omega) = \frac{1}{2\pi^2}\left(\frac{2\mu}{\hbar^2}\right)^{3/2}\left(\hbar\omega - E_g\right)^{1/2}. \tag{3.2}$$

μ is the reduced electron-hole mass. From Eq. (3.1) and Eq.(3.2), the linear absorption coefficient α as a function of incident photon energy $\hbar\omega$ is:

$$\text{for } \hbar\omega < E_g , \alpha(\hbar\omega) = 0 , \tag{3.3}$$

$$\text{for} \hbar\omega \geq E_g , \ \alpha(\hbar\omega) \propto \left(\hbar\omega - E_g\right)^{1/2} . \tag{3.4}$$

As a result, there is no absorption if $\hbar\omega < E_g$ (only consider linear absorption case), and if $\hbar\omega \geq E_g$, the absorption increases as a function of $\left(\hbar\omega - E_g\right)^{1/2}$.

3.1.1 Airy function theory for Franz-Keldysh effect

The Franz-Keldysh effect is the field-induced modulation of the optical properties in a semiconductor in the presence of a static electric field [1,2,46,47]. The coherent acceleration of photoexcited carriers driven by the electric field gives rise to so-called Franz-Keldysh oscillations in the reflection or absorption spectrum for light with photon energy above the bandgap of the semiconductor. The field assisted absorption through a tunneling produces an exponential tail in the reflectivity or absorption spectrum for light with photon energy below bandgap. In practice, electroreflectance (ER) and electroabsorption (EA) based on the Franz-Keldysh effect are used to study band structure critical points because the ER and EA signals are always enhanced at bandgap critical points of semiconductor materials [48]. The Franz-Keldysh oscillations can also give useful information about effective masses in new materials and heterostructures [49].

The Franz-Keldysh effect was first predicted independently by Walter Franz and Leonid Keldysh in 1958 [1,2]. Callaway and Tharmalingam made early contributions as well [50,51]. The theory was developed much more extensively and practically by David Aspnes starting in 1966, when he extended the theory to critical points of various dimension and symmetry [46]. In another work, he extended the theory to both real and imaginary parts of the dielectric function and showed how to include broadening phenomenologically by adding an imaginary argument to the Airy functions [47]. Later Aspnes and Rowe took the low-field limit and showed that under certain conditions, the response is proportional to the third-derivative of the optical constants [48]. This development put ER on solid theoretical footing as a technique for finding semiconductor critical points.

Here we only consider the simple case of a direct transition in the vicinity of a normal (M_0, which means the valence band curves downward and the conduction band curves upward) absorption edge in a direct bandgap semiconductor. This case describes all of our experimental results in the following sections. When a constant electric field, E_B, is applied to a semiconductor, the experimentally measureable change in absorption coefficient is

$$\Delta\alpha(E_B) = \alpha(E_B) - \lim_{E_B \to 0} \alpha(E_B)\,. \tag{3.5}$$

Under the parabolic band approximation with positive effective mass at the normal M_0 edge, neglecting the Coulomb interaction between electrons and holes, the absorption coefficient under a constant electric field is [46]

$$\alpha(E_B) = \left(N^2 / \pi\right) R \theta^{1/2} \left\{ Ai'^2(\eta) - \eta Ai^2(\eta) \right\}, \tag{3.6}$$

where $\eta = (E_g - \hbar\omega)/\hbar\theta$, R is a constant, and θ is the electro-optic frequency

$$\theta = \left[e^2 E_B^2 / 2\hbar\mu \right]^{1/3}, \tag{3.7}$$

here $\mu = m_c m_v/(m_c + m_v)$ is the reduced mass between the conduction band and valence bands, which have effective masses m_c and m_v [47]. *Ai* is the Airy function, which solves [46]

$$\frac{d^2F(x)}{dx^2} = xF(x)\,. \tag{3.8}$$

There are actually two solutions for $F(x)$, $Ai(x)$ and $Bi(x)$, which are the solutions regular and irregular at infinity, respectively. The integral representations of these functions are

$$Ai(x) = \frac{1}{N}\int_0^\infty \cos(\tfrac{1}{3}s^3 + xs)ds\,, \tag{3.9}$$

$$Bi(x) = \frac{1}{N}\int_0^\infty \left[\exp(-\tfrac{1}{3}s^3 + xs) - \sin(\tfrac{1}{3}s^3 + xs)\right]ds\,. \tag{3.10}$$

N is the normalization constant of the Airy function and usually taken as π.

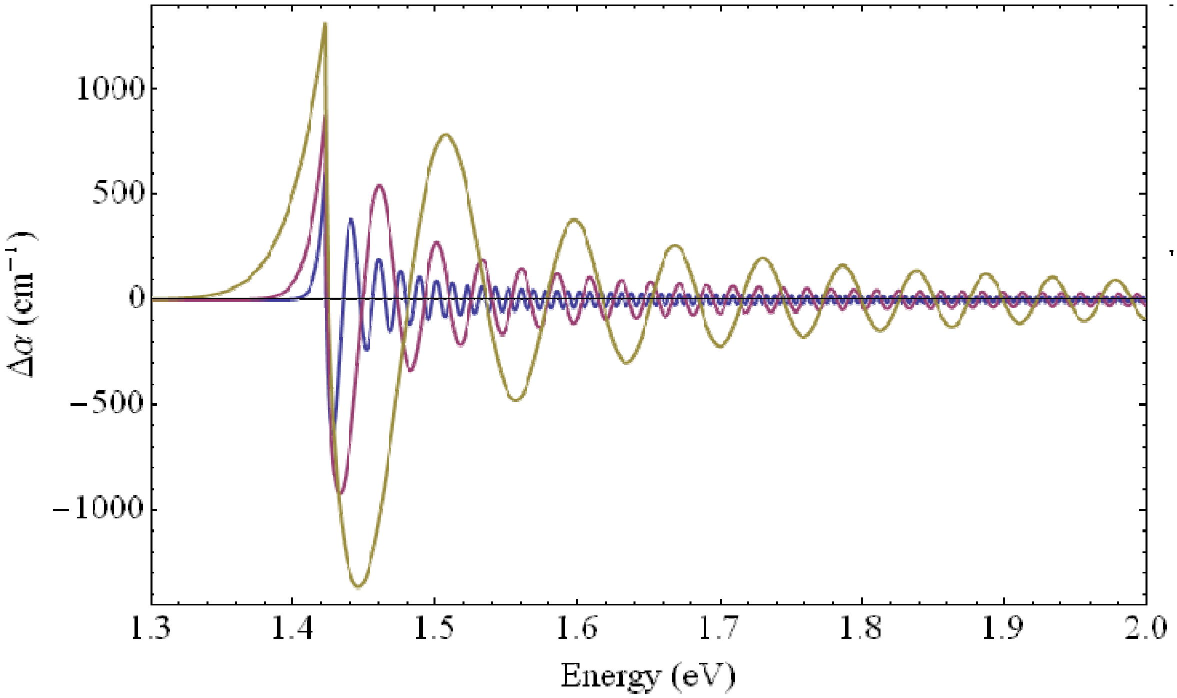

Figure 3.1. Change in absorption coefficient due to the electric field in bulk GaAs predicted by the Airy function theory. Yellow: E_B = 10 kV/cm. Red: E_B = 5 kV/cm. Blue: E_B = 2 kV/cm.

From Eq. (3.5), the experimentally measurable change in absorption coefficient can be obtained using the asymptotic forms of Ai(x) [46] for $x \to \infty$,

$$\Delta\alpha(E_B) = R\theta^{1/2}\left\{\left(N^2/\pi\right)\left[Ai'^2(\eta) - \eta Ai^2(\eta)\right] - \sqrt{-\eta}H(-\eta)\right\}. \quad (3.11)$$

where $H(x)$ is the unit step function, equal to one for positive x, and zero for negative x. The expression for Δα in Eq. (3.11) is based on the approximation that the index of refraction n is constant as the photon energy is tuned across the M_0 edge, which is a good approximation for the fundamental edge in GaAs. For higher absorption thresholds the variation of n with field must be taken into account. The change in absorption coefficient as predicted by Eq. (3.11) is plotted as a function of photon energy in Figure 3.1.

In a semiconductor, absorption is related to the dielectric constant through the Kramers-Kronig relations, thus the dielectric constant is also affected by the DC field. In case of electroreflectance, the normalized change in reflectivity under a constant electric field is [49]

$$\Delta R / R = a(\varepsilon_1, \varepsilon_2)\delta\varepsilon_1 + b(\varepsilon_1, \varepsilon_2)\delta\varepsilon_2 , \qquad (3.12)$$

where ε_1 and ε_2 are the real and imaginary parts of the complex dielectric constant $\varepsilon = \varepsilon_1 + i\varepsilon_2$, and a and b are the Seraphin coefficients, related to the unperturbed dielectric function. Analogous to the absorption coefficient, the complex dielectric function under a constant electric field is

$$\varepsilon(E - E_g, E_B) = \varepsilon(E - E_g, 0) + \Delta\varepsilon(E - E_g, E_B) \qquad (3.13)$$

where $\Delta\varepsilon$ is the change of ε due to the electric field.

In the experiments, we modulate the DC field and measure the change in reflectivity spectrum of a laser beam. It will be useful to compare the data to a simple theory. Near the fundamental bandgap of a bulk semiconductor, $b \approx 0$, and assuming electromodulation from flatband, where the field-induced change in dielectric function is equal to the dielectric change due to the perturbation in the field modulation experiment, we have

$$\Delta R / R \cong a \,\mathrm{Re}[\Delta\varepsilon(E - E_g, E_B)]. \qquad (3.14)$$

Near the fundamental bandgap of a III-V semiconductor, the change of the dielectric constant is [49]

$$\Delta\varepsilon(E-E_g,E_B)=\sum_i \alpha_i G\left(\frac{E_g-E}{\hbar\theta_i}\right), \tag{3.15}$$

where i = hh, lh, for heavy-hole and light-hole contributions, θ is the electro-optic frequency, and

$$\alpha_i=\frac{2e^2\hbar^2\left|e\cdot P_{c,v}\right|^2}{m^2E^2}\left(\frac{2\mu_i}{\hbar^2}\right)^{3/2}(\hbar\theta_i)^{1/2}, \tag{3.16}$$

with μ the reduced mass, and $P_{c,v}$ the momentum matrix element between conduction and (heavy hole or light hole) valence band. The 'electro-optic' function $G(\xi)$ has an Airy function form [52]

$$G(\xi)=\pi[Ai'(\xi)Bi'(\xi)-\xi Ai(\xi)Bi(\xi)]+\sqrt{\xi}H(\xi)+i\{\pi[Ai'^2(\xi)-\xi Ai^2(\xi)]-\sqrt{-\xi}H(-\xi)\}, \tag{3.17}$$

where Ai and Bi are given by Eq. (3.9) and Eq. (3.10). The effect of broadening can be included by replacing $E-E_g$ with $E-E_g+i\Gamma$ in Eq. (3.6) and Eq. (3.14), where Γ is a broadening parameter. The change in reflectivity as predicted by Eq. (3.14) is plotted as a function of photon energy in Figure 3.2.

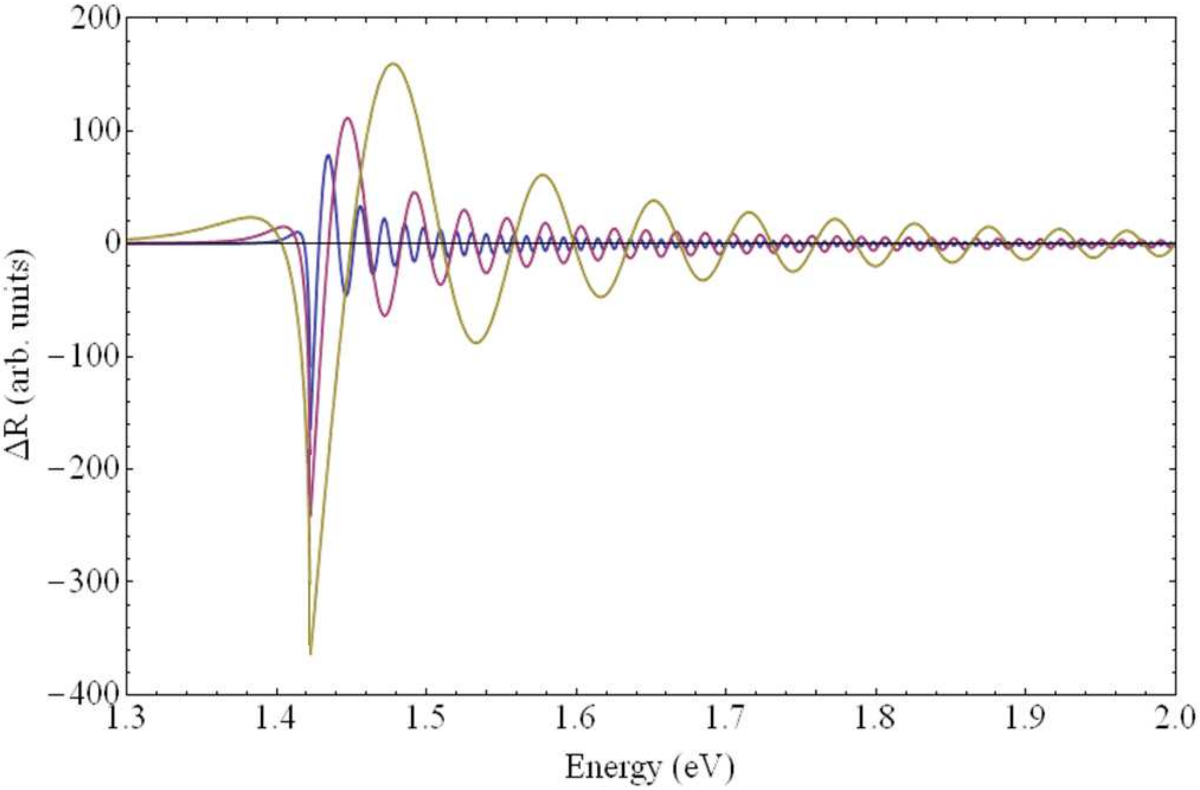

Figure 3.2. Electric field induced change in reflectivity in bulk GaAs predicted by the Airy function theory. Yellow: E_B = 10 kV/cm. Red: E_B = 5 kV/cm. Blue: E_B = 2 kV/cm.

3.2 DC bias electroreflectance experiment and results

Electroreflectance (ER) based on the Franz-Keldysh effect is a widely used characterization technique for semiconductor materials. A modulated electric field produces a resonant differential reflectance spectrum at band structure critical points [48]. In our experiment we start with a transverse electrode sample structure and DC bias. The metal electrodes are in direct contact with the semi-insulating GaAs sample, and from the experimental results we observe a highly nonuniform electric field distribution in the gap between electrodes due to strong trap-enhanced electric field effects.

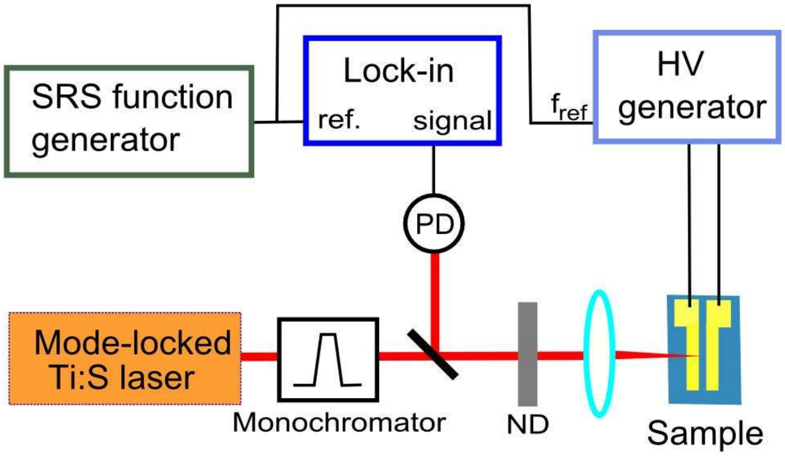

Figure 3.3. Diagram of the DC bias ER experimental apparatus. The electrodes are in direct contact with sample. ND: neutral density filter

The experimental apparatus for DC bias ER is shown in Figure 3.3. For a light source we use a mode-locked Ti:sapphire laser with a spectrum centered at 820 nm, with full width, half maximum 40 nm and repetition rate $f_{\mathrm{rep}} \approx 89$ MHz. The pulse energy is 5.5 nJ with about 70 fs duration (we use a laser as our light source for all of our ER and EA experiments because it is required in experiments using the radio-frequency bias). The laser output is passed through a Spectral Products Model CM 110 monochromator, with a 600 line/mm grating blazed at 500 nm and a resolution of 1.5 nm. After the monochromator, the spectrally resolved light is sent through a neutral density filter and then focused on the sample using a lens with a focal length of 75 mm. The average power at the sample is approximately 45 nW. The FWHM beam waist at the focus on the sample is measured to be 26 μm using the knife edge formed by the Au-GaAs interface (there is a large difference in reflectivity between GaAs and Au). Back reflected light from the sample is captured by a beam splitter and measured with a custom high gain photodetector. The sample is a (100)-oriented SI-GaAs wafer with two Au electrodes patterned directly on the GaAs surface, separated by a 100 μm gap. The sample position is controlled with respect to the focusing lens using a stepper motor. A square-wave voltage, which is generated by a high-voltage square wave generator, is applied across the gap between electrodes so as to produce a periodic modulating field. We modulate the bias between 0 V and 410 V at 1 kHz. The modulation frequency is produced by a Stanford Research System DS-345 function generator. The ER signal is measured by a lock-in amplifier at this modulation frequency.

By moving the sample position with respect to the laser focal spot with a motorized translation stage, we measure the ER signal distribution in the gap between electrodes. A map of the ER spectrum versus spot position is shown in Figure 3.4, where the x axis corresponds to incident photon energy, and the y axis corresponds to focal spot position. Here the polarization of the laser light is parallel to the applied electric field. The edges of two Au electrodes, located around 15 μm and 115 μm with respect to the y axis, are indicated by the red lines. The field induced variation of reflected light intensity, ΔR, is normalized by the total reflected intensity R, which is directly proportional to the average output of the photodetector. From the ER signal distribution we find that the ER signal is strongly enhanced near the positively charged electrode edge, which is around 115 μm in Figure 3.4. As the electrodes are in direct contact with the SI-GaAs sample, free-carrier injection from electrode will lead to increased free-electron occupancy of the EL-2 defect near the anode edge, giving rise to the trap-enhanced electric field (TEF) in this region. The ER signal enhancement near the anode edge is mainly related to the strong TEF [9].

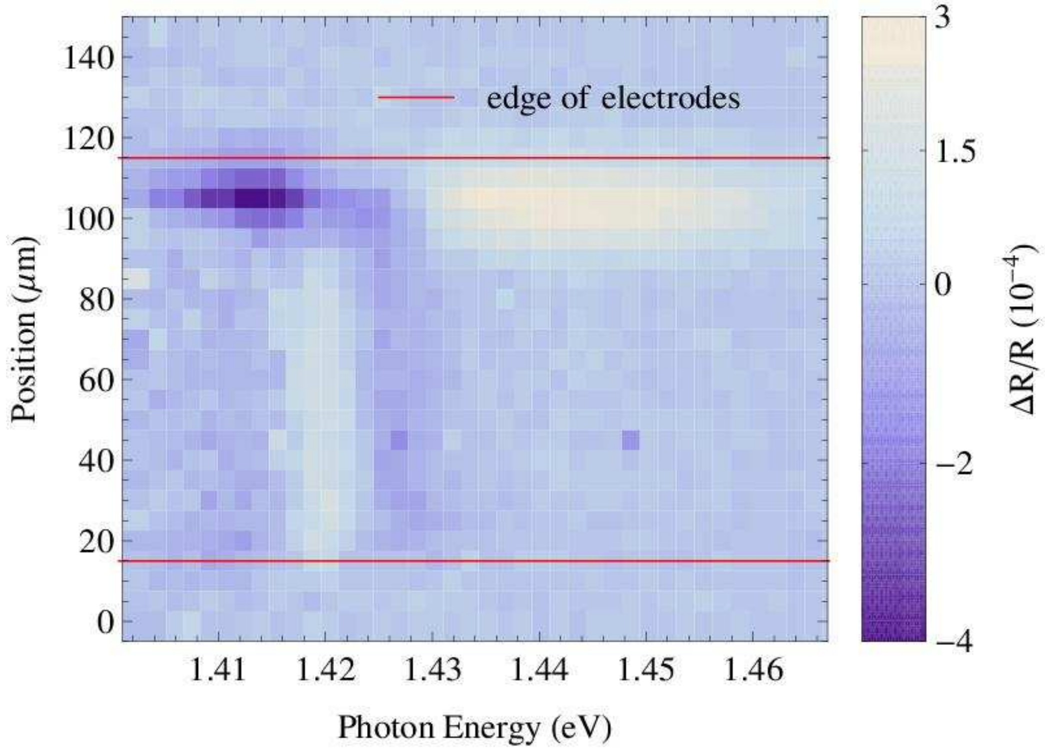

Figure 3.4. Two-dimensional plot of the ER spectrum with DC bias vs. laser spot position. Lines show the approximate position of the electrode edges.

We estimate the electric field distribution in our sample by using the experimental data combined with the Airy function theory. In GaAs at the photon energies used here, the ER line shape is given to a good approximation by the electro-optic function $G(x)$ [47]. For a uniform electric field within the laser spot, the theoretical reflectivity as a function of laser energy $\hbar\omega$ predicted in Eq. (3.14) can be written in a simplified form:

$$\Delta R(\hbar\omega, E_B) \propto \frac{1}{\theta(E_B)} G[\frac{\hbar\omega - E_g + i\Gamma}{\hbar\theta(E_B)}]. \quad (3.18)$$

Here Γ is the broadening parameter, E_B is the bias field, and E_g is the band gap energy (for GaAs at room temperature, $E_g = 1.42$ eV). The electro-optic frequency θ is defined in Eq. (3.7).

Using $\mu = 0.036\ m_e$ (only light holes contribute for optical polarization parallel to bias field [53]), one can derive from Eq. (3.18) a relation between the electric field strength and the energy of the first dip above the band gap in the ER spectrum. We choose the position of the first dip above gap because it is not strongly affected by either field inhomogeneity or broadening. The electro-optic energy is related to the difference between the energy of the dip E_{dip} and the band gap energy E_g by: $E_{dip} = E_g + \alpha \bullet \theta(E_B)$, where α is a real number which can be found analytically from Eq. (3.18) (here we got $\alpha = 1052$). Once α is found, the actual electric field strength can be calculated through Eq. (3.7).

We estimated the actual electric field distribution inside this direct contact sample with DC bias from the ER data. The estimated electric field versus position between electrodes is shown in Figure 3.5. The field strength near the positively biased electrode edge is almost 100 times stronger than other part of the gap, which is comparable to other results on the trap-enhanced field effect [9]. The highly inhomogeneous TEF also affects the shape of the Franz-Keldysh oscillations strongly by making the oscillations above bandgap diminish quickly with increasing photon energy. The field nonuniformity within the laser spot acts like a huge broadening parameter.

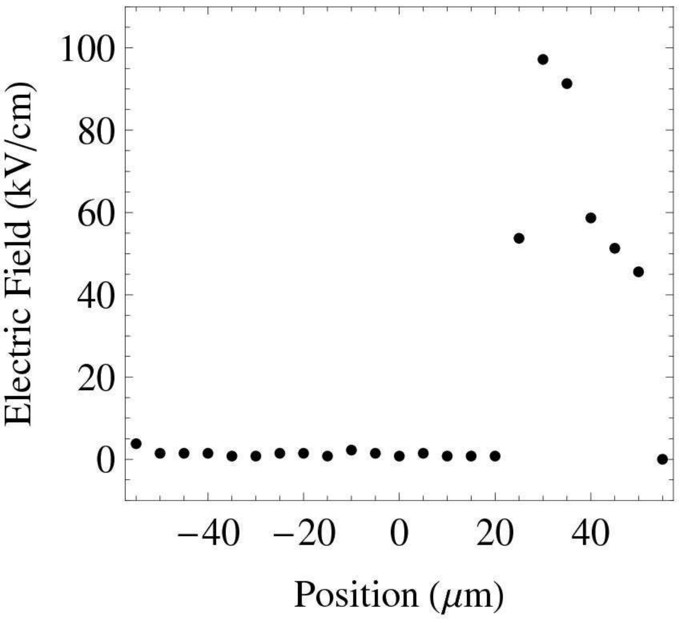

Figure 3.5. Extracted electric field vs. the position of the laser spot for DC bias ER.

3.3 Radio-frequency bias electroreflectance

In this section, we present our ER experiments using a transverse electrode sample structure with RF bias and heterodyne detection technique as discussed in Chapter 2; we discuss the main results of our electroreflectance experiments with RF technique, and compare the results with the DC biased direct contact electrode sample.

A diagram of the experimental apparatus is shown in Figure 3.6. The optical part of the setup is identical to that of the DC bias experiment in section 3.2. An RF bias of frequency $f = \frac{1}{2} f_{\text{rep}} + 1$ kHz $\approx$ 44.5 MHz is applied across the electrodes on the sample. The bias voltage is around 400 V (measured by the monitor of the LC circuit, as shown in Figure 2.5). The lock-in amplifier measures at $f_{\text{ref}} = 2f - f_{\text{rep}}$.

We studied a semi-insulating (100)-oriented GaAs wafer. The sample includes a 100 nm SiO_2 layer between Au electrodes and GaAs as an insulating layer. The detailed sample geometry was described in Chapter 2. Position of the sample with respect to the laser focal spot is controlled using a motorized translation stage.

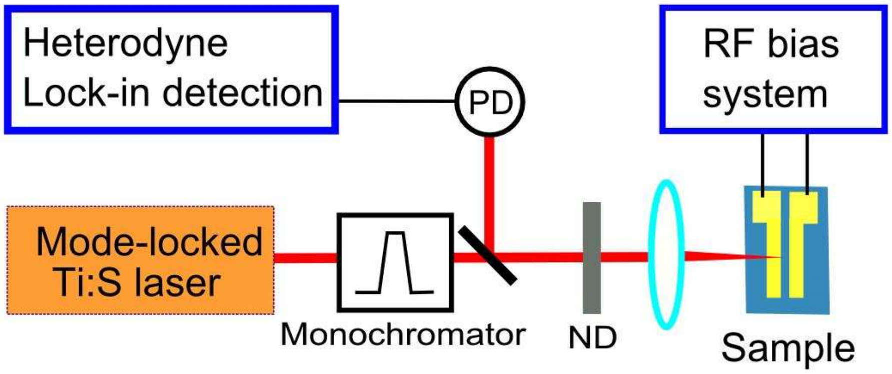

Figure 3.6 Diagram of the RF bias ER experimental apparatus. The sample is in the transverse ER configuration with insulated electrodes. ND: neutral density filter

The main purpose of our RF technique is to achieve a more uniform electric field distribution in a transverse electrode geometry. By scanning the sample under the laser spot with the stepper motor stage and recording the ER spectrum as a function of spot position, we can map the electric field between two Au electrodes. A plot of the ER signal versus position is shown in Figure 3.7. The polarization of the laser light is also parallel to the applied electric field.

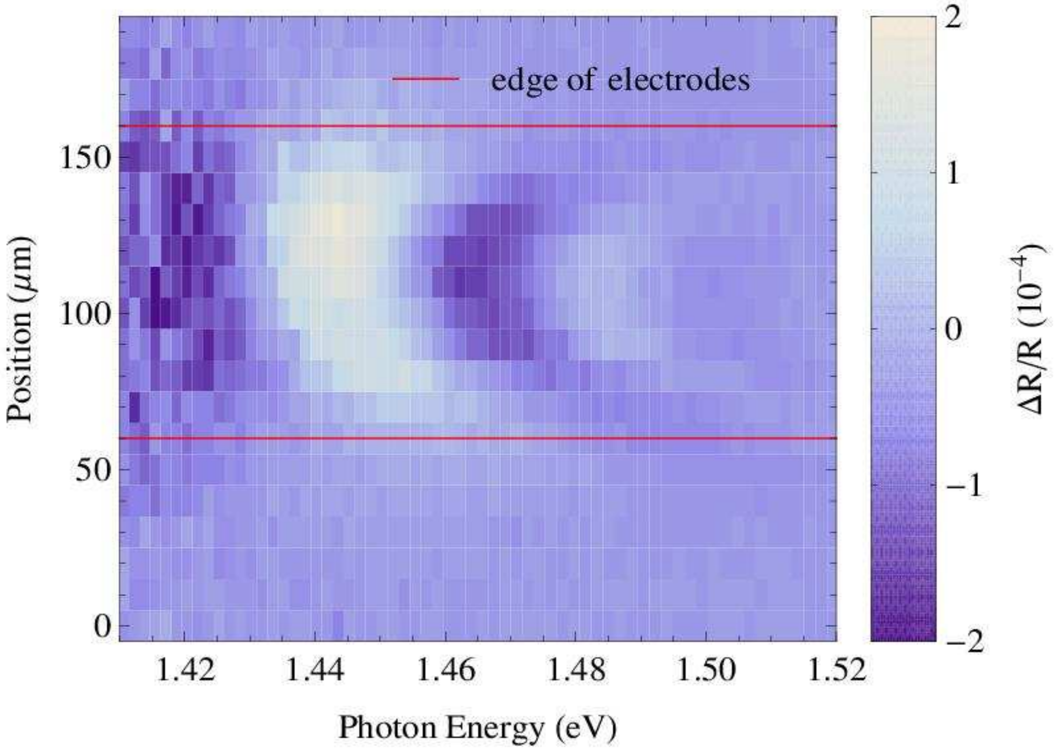

Figure 3.7. Two-dimensional plot of the ER spectrum with RF bias vs. laser spot position. Lines show the approximate position of the electrode edges.

The edges of the two Au electrodes are located around 60 μm and 160 μm with respect to *y* axis, as indicated by the red lines in Figure. 3.7. The field induced variation of reflected light intensity ΔR is normalized by the total amount of reflected intensity R, which as in the DC bias ER experiment, is recorded directly from the output of the photodetector by an Agilent digital multimeter. We can see the ER signal ΔR/R is now distributed fairly uniformly across the gap, and from this data we can estimate the actual electric field in the sample between electrodes using the simplified Airy function approximation based on parabolic-band assumption, as introduced previously.

The estimated electric field from our RF ER data is shown in Figure 3.8. We find, as expected, that the field is weakest (but most uniform) in the center of the two electrodes. The field near the electrode edges is higher than in the center due to geometric effects. The field distribution in Figure 3.8 is far more uniform compared with the one shown in Figure 3.5 – the difference between the electrode edge and the center of the gap is only around a factor of 2 in Figure 3.8, whereas in Figure 3.5 the difference is close to a factor of 100. This is proof of the uniform electric field achievable by using the RF technique.

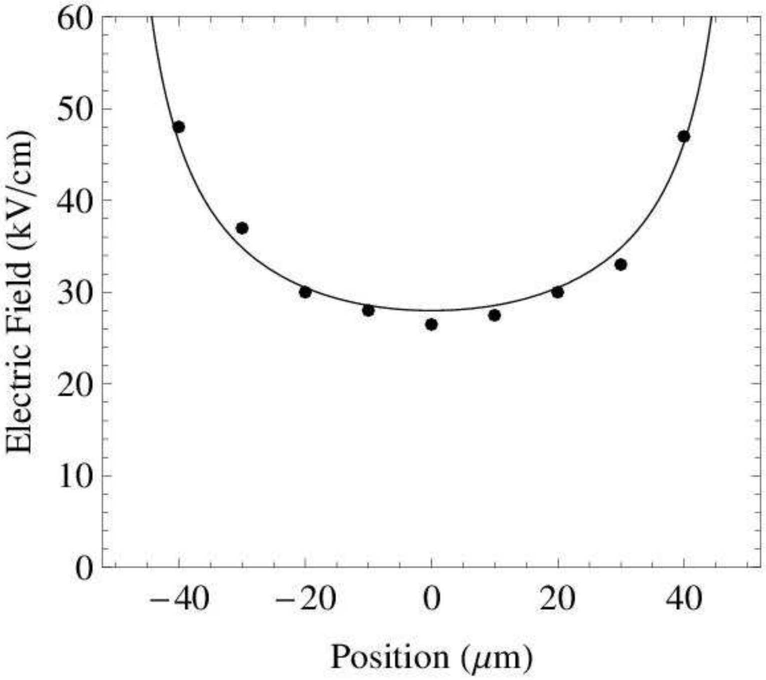

Figure 3.8. Extracted electric field vs. the position of the laser spot. The line is a fit to the analytical theory of Ref. [39].

The calculated electric field distribution from our data was fit to an analytical theory from the appendix of Ref. [39]. This theory, which assumes an idealized two-dimensional potential distribution with simple boundary conditions for a typical transverse electrode geometry, can describe the bias field distribution in sample structures such as the one studied here quite accurately, at least in the absence of trap-enhanced fields. The field on the surface of the gap between two electrodes is:

$$E = \frac{\pi V}{4dK(1-m)}[1 - m \cdot \cosh^2(\frac{\pi V}{2d})]^{-1/2} . \tag{3.19}$$

Where K is the complete elliptic integral of the second kind, d is the sample thickness, V is the bias voltage, and $m = \cosh^{-2}(\frac{\pi s}{4d})$ (where s is the distance between electrodes). The theoretical result for our sample (of 300 μm thickness, neglecting the thin insulating layer) is shown as a solid line in Figure 3.8. In the center of the gap, the ER spectrum is consistent with a peak electric field of 26.5 kV/cm. The best fit of the field distribution yields a peak bias of 430 V. With electrodes in direct contact with the sample and a similar bias of 410 V, the electric field extracted from the ER spectrum with the laser spot in the center of the gap is only 5.5 kV/cm.

A direct comparison of single ER traces using both DC and RF bias is shown in Figure 3.9. The dashed line shows an ER trace using direct contact sample with a DC bias of 410 V modulated a 1 kHz, with the laser spot focused midway between the electrodes. The solid line shows an ER trace using a sample with electrodes insulated from the surface and RF bias, also focused at the same position. Both traces are taken with optical field parallel to the bias field.

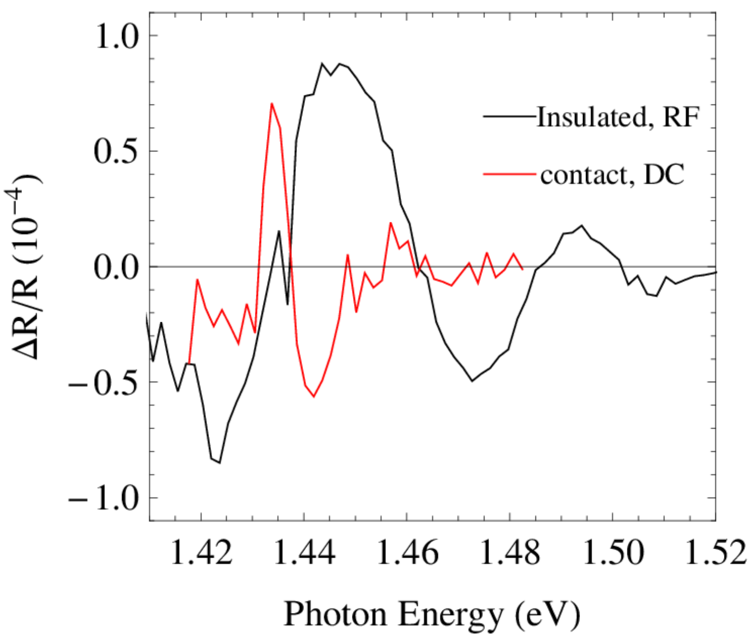

Figure 3.9. ER spectra for GaAs with the probe beam centered between the electrodes, for the optical field parallel to the bias field. The dashed line is an ER spectrum using a sample with electrodes on the surface of the sample and a DC bias, and the solid line is an ER spectrum using a sample with electrodes insulated from the surface of the sample and an RF bias.

The spacing between Franz-Keldysh oscillations is related to the electric field. From Figure 3.9 we can see that even if a bias with same amplitude is applied, for the sample with direct contact electrodes the effective electric field in the center of the gap is much smaller compared with the insulated electrode sample, which has a more uniform field distribution. This is an important advantage of the RF bias technique.

3.4 Bias, polarization, and optical power dependence the RF bias electroreflectance

More results from the RF bias electroreflectance, including the ER signal dependence on the applied bias, the optical polarization of incident light, and the optical power, will be discussed in this section.

3.4.1 Bias dependence

We also studied the dependence of ER signal on applied RF bias. The magnitude of the RF bias can be controlled by adjusting the output amplitude of the DDS (direct digital synthesizer). In this way, one can change the bias amplitude itself without inducing any phase shift between the RF bias and the Ti:sapphire laser pulse train (if one uses RF attenuators to adjust the amplitude, a phase shift can be induced). The change of the ER signal with increasing electric field is shown in Figure 3.10.

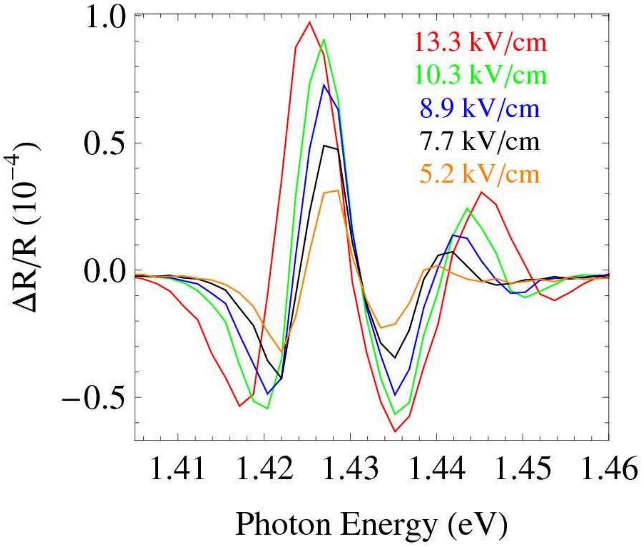

Figure 3.10. The evolution of the ER spectrum of GaAs with increasing bias field.

In Figure 3.10, we can see the entire oscillation period changes with increasing electric field in the manner that is predicted by the parabolic band theory: the oscillation peaks and dips above band gap shift toward higher energy. Physically, this is due to the fact that photo-carriers are accelerated more quickly by stronger electric fields, thus gaining higher energy.

By finding the best fit of the ER spectrum between the theory prediction and the experimental data, one can also measure the broadening energy Γ, which is related to the decay processes of free carriers such as collisions, trap recombination, phonon emission, etc [39]. Figure 3.11 shows a 'best fit' to the ER spectrum at a field of 13.3 kV/cm. The 'best fit' occurs for $\Gamma = 4.5$ meV. We attribute the poor fit at low energies to the fact that the semiconductor is transparent at those energies. This results in experimental artifacts due to the reflection of light from the back surface of the sample, which has been seen in previous experiments [82].

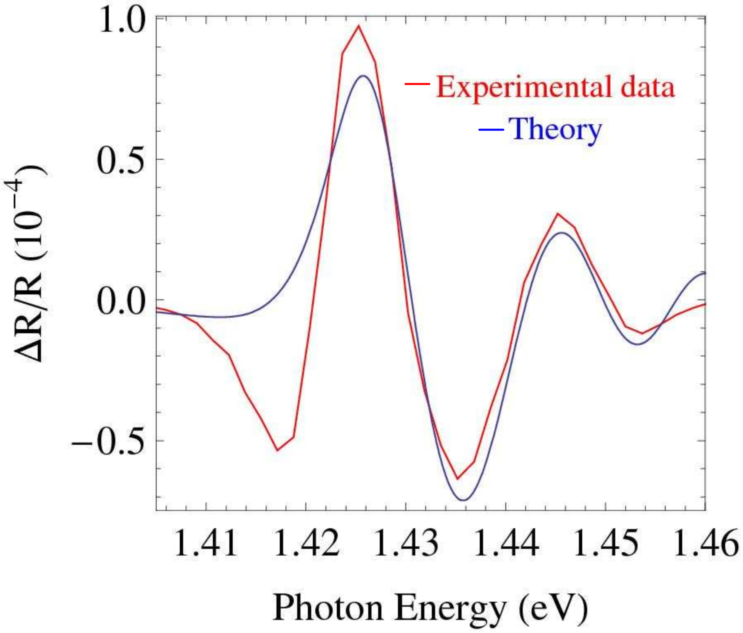

Figure 3.11. Fit of theoretical curve to experimental ER data near the fundamental band edge of GaAs.

3.4.2 Optical polarization dependence

The polarization dependence of electro-absorption (EA) spectra has been studied both theoretically and experimentally in the past as a way of studying the symmetry of band structure critical points [41,53]. The origin of the polarization dependence of the Franz-Keldysh absorption spectrum near the band gap in GaAs is related to how the heavy hole (hh) – conduction band (CB) and light hole (lh) – conduction band transitions contribute differently to the bulk absorption.

Consider incident light with variable polarization on bulk GaAs in the presence of a DC field. Here transverse electric (TE) is defined as the electric field of the incident light pointing perpendicular to the field vector of the applied electric field, and transverse magnetic (TM) refers to when the electric field of the incident light is parallel to the field vector of the applied electric field. Then the bulk electroabsorption of GaAs can be decomposed into its hh-CB and lh-CB contributions, writing for TE and TM electroabsorption, respectively [53],

$$\alpha_{TE}(\omega, E_B) = P^2 \alpha_{hh}(\omega, E_B) + \frac{1}{3} P^2 \alpha_{lh}(\omega, E_B) \tag{3.20}$$

$$\alpha_{TM}(\omega, E_B) = \frac{4}{3} P^2 \alpha_{lh}(\omega, E_B) \tag{3.21}$$

Where P is the momentum matrix element, and $\alpha_{lh}(\omega)$ and $\alpha_{hh}(\omega)$ differ from each other by the combined density of states in the perpendicular direction with respect to the field and the square of the envelope function overlaps along the field direction. As shown in Eq. (3.20) and Eq. (3.21), the TM polarized light only interacts with the lh band, whereas the absorption of the TE polarized light is affected by both hh and lh bands. Due to the fact that the lh-CB combined density of states is larger than the hh-CB combined density of states, and the decay of the below band gap tunneling tail for hh is faster than lh, $\alpha_{lh}(\omega)$ is larger than $\alpha_{hh}(\omega)$, and the ratio between them grows with increasing photon energy. As a result, the absorption of TM polarized light which consists of only lh-CB contributions, is stronger than the absorption of TE polarized light, which consists of mainly hh-CB contributions. This explains the polarization dependence of the below gap exponential tail of ER, which was studied previously. The above gap dependence is what we are more interested in, and it is simply related to the fact that the effective masses are different.

Ruff et al. studied the EA spectrum of a low temperature grown GaAs (LT-GaAs) epi-layer, they show that with photon energy above the band gap, the Franz-Keldysh oscillations for TM polarized light show longer oscillation periods compared with TE polarized light, and below band gap, the TM absorption is stronger than TE

[41]. The results are in good agreement with theory calculations using both k•p model and 2D diagonal approximation.

Although the best available theories calculate only the EA spectrum, the ER is related through the Kramers-Kronig relations [47], and thus the same polarization dependence can be expected, with a somewhat different line shape near the band edge. Taking advantage of our transverse M-S-M sample geometry, we can study the polarization dependence of the ER signal at the fundamental band gap of GaAs. A half-wave plate in front of our SI-GaAs sample rotates the polarization of the incoming laser beam with respect to the direction of the applied electric field in the sample. The polarization dependent ER signal plotted with both linear and log scales is shown in Figure 3.12.

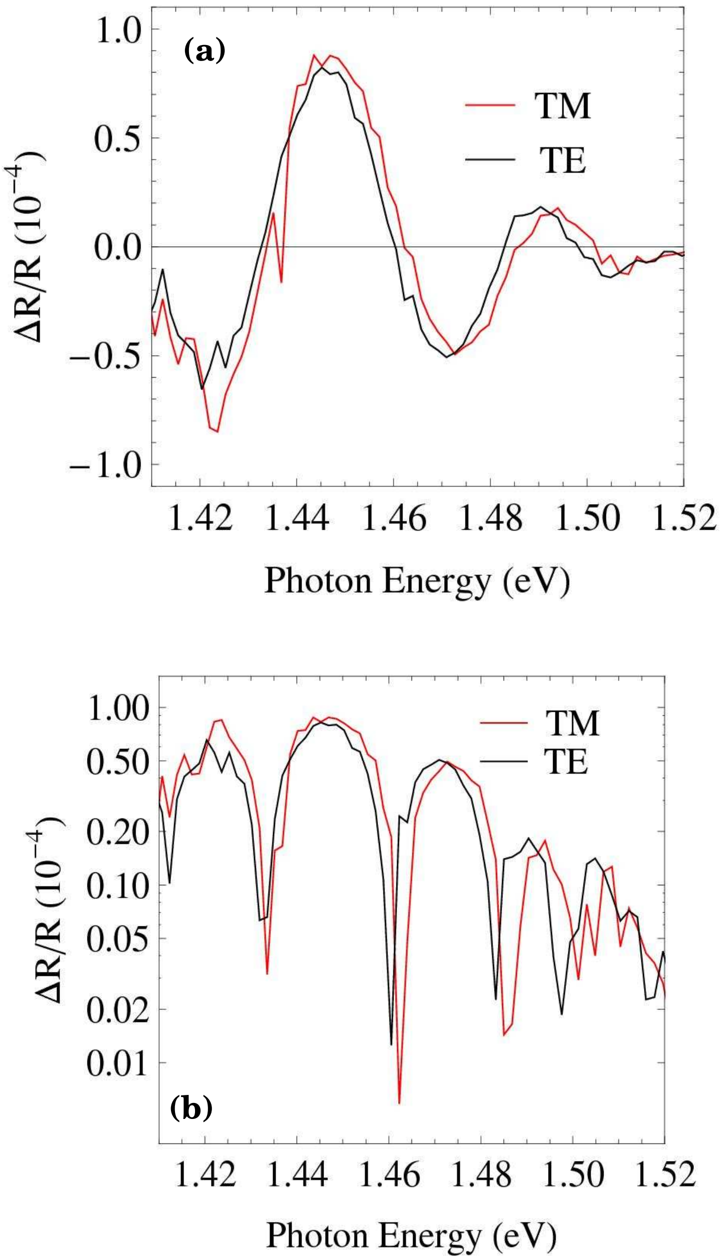

Figure 3.12. Polarization dependence. (a) ER spectrum in linear scale for GaAs with beam centered between electrodes, for the optical field perpendicular (TE, black) and parallel (TM, red) to the RF bias field. (b) Absolute value of ER spectrum in logarithmic scale, to highlight the positions of the Franz-Keldysh oscillations.

Figure 3.12 (a) shows the ER spectrum of SI-GaAs in linear scale for two different polarization configurations with the laser spot midway between the electrodes. And the absolute value of the field induced reflection change in logarithmic scale is shown in Figure 3.12 (b). The strong dips in the spectrum are due to the zero crossings of the reflectivity spectrum. In both linear and logarithmic scales, a clear difference in the differential reflectivity between TE (black) and TM (red) polarized light is evident. Our ER results match previous EA results and theoretical calculations in that, for energies above the band gap, the oscillation period is longer for TM incident polarization than for TE, as expected because of the difference between the effective masses of the light and heavy holes.

3.4.3 Optical power dependence

We also studied the optical power dependence of the ER signal with RF bias. A continuously adjustable neutral density filter in front of the SI-GaAs sample is used to control the incoming beam power precisely. In order to study the influence of photocarrier generation on the electric field distribution inside the sample, we also performed spatial scans by scanning the sample under the laser spot and measuring the ER spectrum with a variety of optical powers. The two-dimensional plots of the ER spectrum versus laser spot position are shown in Figure 3.13, with average optical power at the sample from 50 nW up to 15 μW. The two red lines in each figure indicate the edges of the two electrodes.

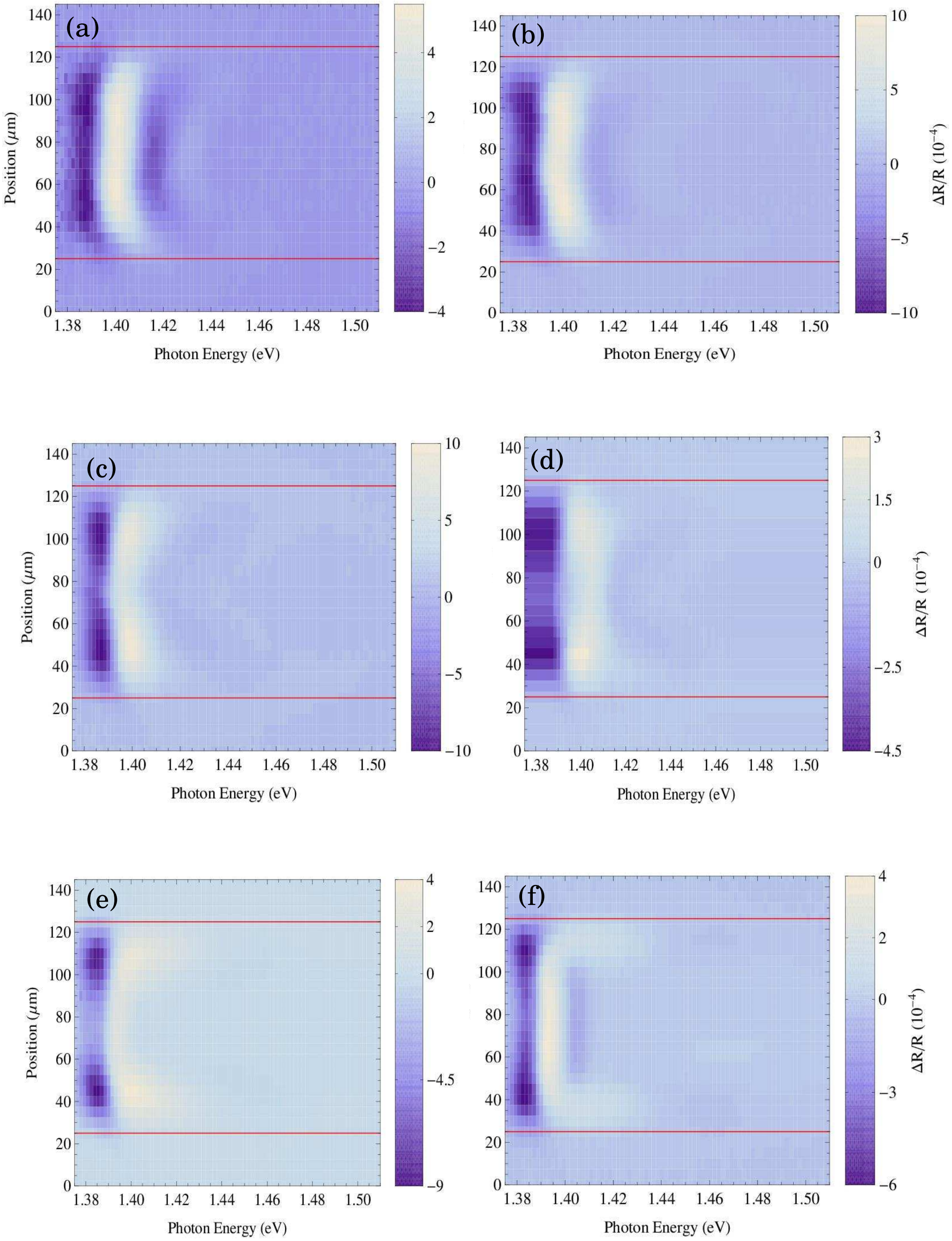

Figure 3.13 Two dimensional plots of the ER spectrum vs. laser spot position. (a) 50 nW optical power; (b) 1 μW; (c) 3 μW; (d) 5 μW; (e) 10 μW; (f) 15 μW.

From Figure 3.13, with increasing optical power the rate of photocarrier generation clearly affects the ER signal distribution in the gap between electrodes. Under relatively low optical power (less than 5 μW), the normalized ER signal $\Delta R/R$ distributes uniformly cross the gap. When the optical power reaches 5 μW, the $\Delta R/R$ signal starts decreasing, and remains roughly constant under higher optical power. The calculated electric fields versus the position of laser spot under different optical power corresponding to spatial scans in Figure 3.13 are shown in Figure 3.14.

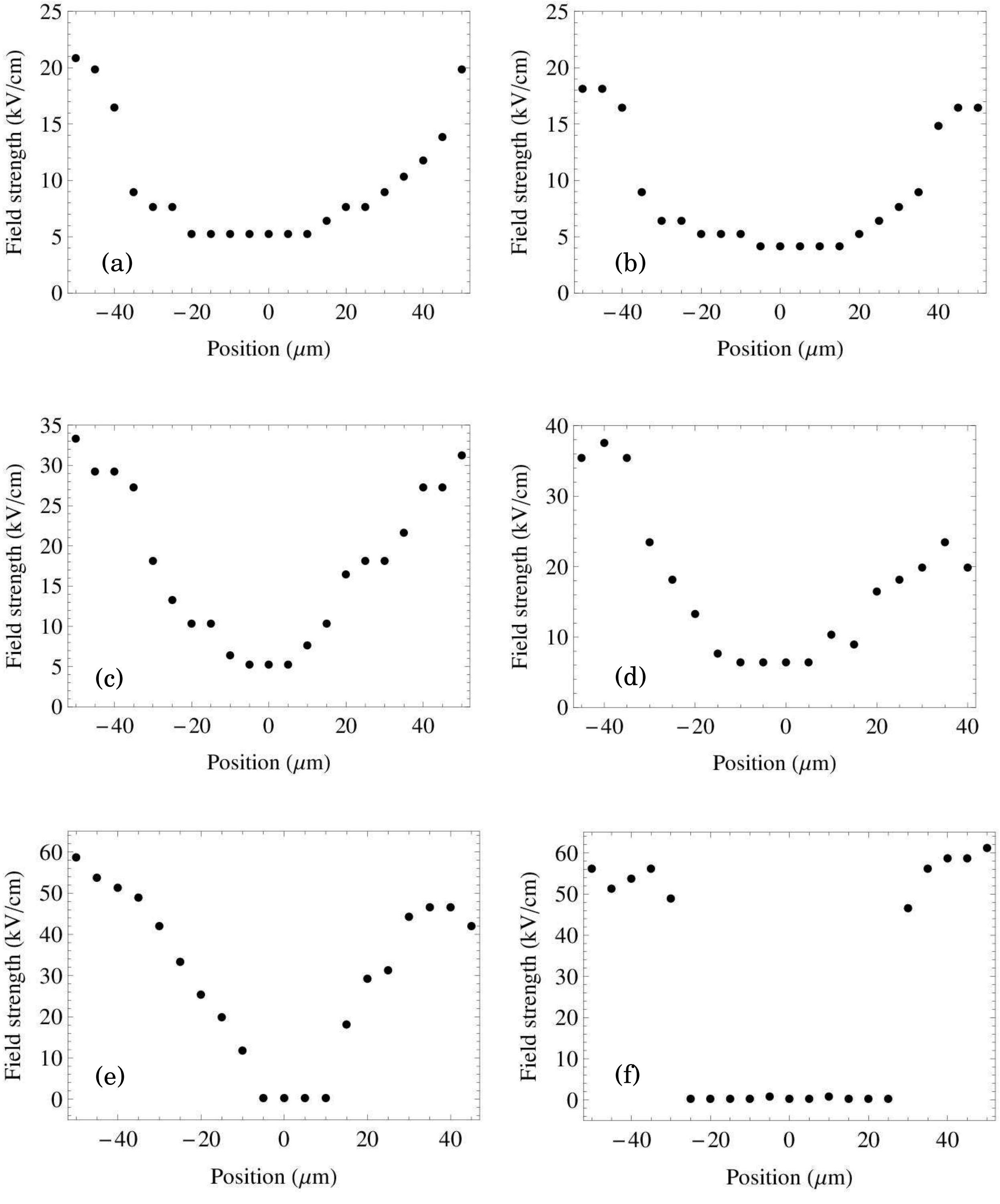

Figure 3.14. Extracted electric field vs. laser spot position from the data in Fig. 3.13. (a) 50 nW optical power; (b) 1 μW; (c) 3 μW; (d) 5 μW; (e) 10 μW; (f) 15 μW.

In Figure 3.14, the electric field distribution under different optical powers is estimated using the mapping method that was discussed in section 3.2. The electric field near the edge of each electrode increases constantly with increasing optical power. Interestingly, the electric field around the center of the gap between electrodes remains constant with average optical power below 10 μW, and with higher optical power (above 10 μW) the field in the center drops to almost zero. The optical power dependence of the electric field distribution can be explained partially by the 'optical biasing effect' which is induced by optical injection of free carriers [9]. As described in Chapter 2, our sample has a SiO_2 insulating layer between As electrodes and SI-GaAs surface, this SiO_2 layer prevents carrier injection from electrodes. But under strong illumination, large amount of optical injected free carriers can also be captured by traps in SI-GaAs, and thus have a strong effect on the potential distribution. Other effects, like high field dynamics of free carriers, can also be involved. More theoretical work, e.g., calculation of Franz-Keldysh effect that take into account Coulomb interactions between electrons and holes under strong optical illumination, would be needed to fully understand the optical power dependence of the ER signal.

3.5 Electroabsorption experiment and results

Although the sample preparation can be a bit more complicated, experiments based on the electric field induced change in absorption spectrum can provide a better signal-to-noise ratio than electroreflectance. Also, the experiment discussed in Chapter 5, about the field-induced population control, had to be done in transmission in a thin sample. So we also performed electroabsorption (EA) experiments. The experimental apparatus for EA is very similar to the ER setup. We use the same Ti:sapphire laser as the light source. To provide spectral resolution and achieve a tight focus at the sample, we used a 4*f* pulse shaper with a movable slit at the focal plane to spectrally resolve the incident light. The home-made pulse shaper is used as a monochromator in this experiment. The spectral resolution of the pulse shaper is around 0.3 nm. We focus the spectrally resolved laser beam after the pulse shaper onto a thin GaAs sample, and simply collect the transmitted light, then focus it again onto a silicon photodiode for detection. Figure 3.15 is a diagram of the experimental apparatus.

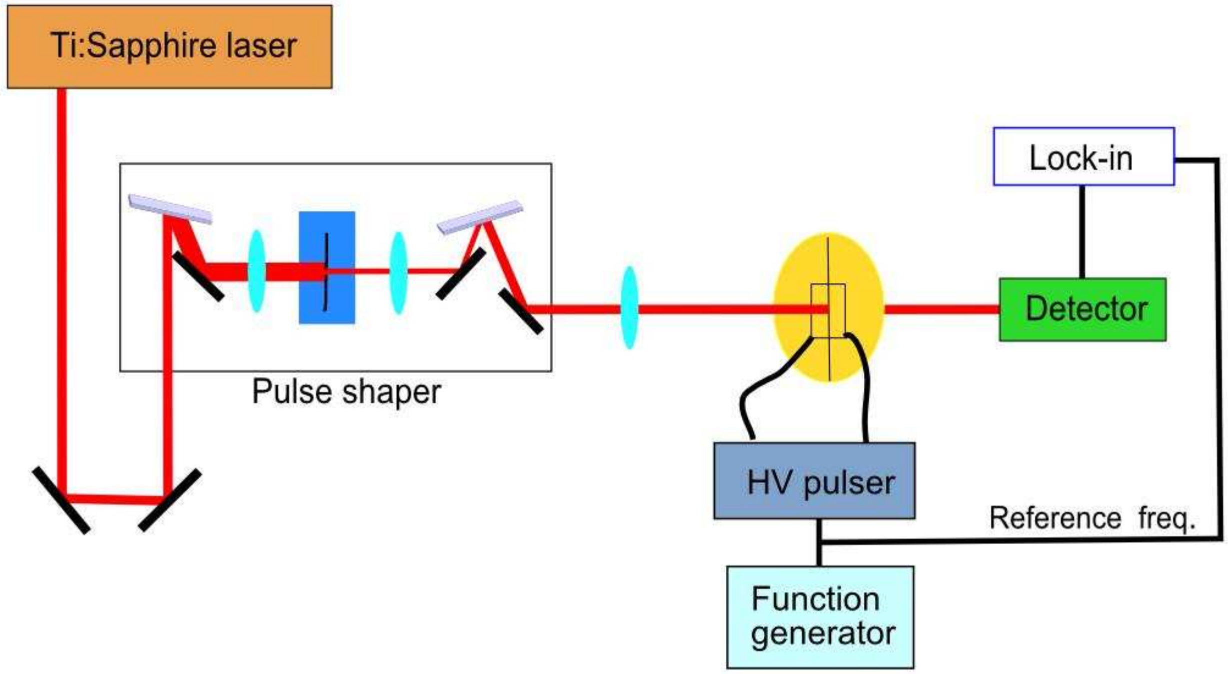

Figure 3.15 Transverse electroabsorption (EA) setup. The EA signal is measured as a function of incident photon energy.

The sample we studied is an undoped GaAs epilayer of thickness 1 μm, grown by molecular beam epitaxy with an AlAs etch stop. The GaAs sample is attached to a sapphire disk first using transparent wax, and the substrate is then removed by mechanical thinning and chemical etching. More details about the thin sample can be found in Appendix C. After thinning and etching, Ti:Au electrodes of roughly 200 nm thickness are evaporated on the GaAs surface, separated by 120 μm. The gap between electrodes is made by a shadow mask using a thin magnet wire. A DC bias generated by the high-voltage square wave generator is applied to the sample. The function generator produces a modulation frequency which is set to be a reference signal for the high-voltage pulser and the lock-in amplifier. The sample position with respect to the laser focal spot is also controlled by a stepper motor stage. In Figure 3.16, representative EA experimental spectra for two orthogonal optical polarizations of incident beam are plotted. For energies above the band gap, the EA oscillation period is slightly longer for TM polarized light than for TE. The results are consist with previous studies [41,53].

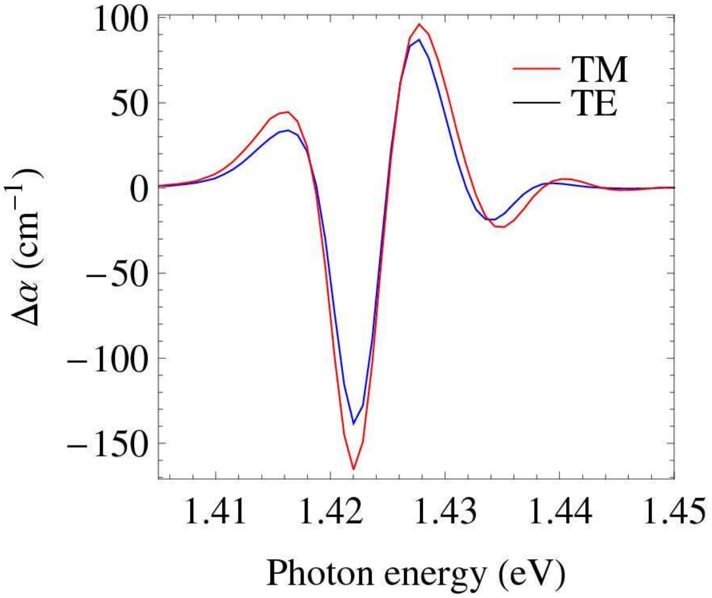

Figure 3.16. Representative electroabsorption spectra for TM (transverse magnetic) and TE (transverse electric) polarization.

Multiple EA traces taken under different bias field strength are shown in Figure 3.17. The incident light is TM polarized. Just as in the ER case, the main dips at the bandgap critical point are fixed, and the oscillation peaks above bandgap shift toward higher energy with increasing electric field. As discussed in Section 3.1, in the parabolic band approximation, with electric fields sufficiently large that Coulomb effects can be neglected, the EA lineshape takes the form of the electro-optic function $F(x)=[Ai^{'}(x)]^2 - xAi^2(x) - \sqrt{-x}H(-\mathrm{Re}[x])$. For a uniform electric field within the laser spot, the theoretical differential absorption as a function of laser energy $\hbar\omega$ predicted in Eq. (3.11) can be written in a simplified form:

$$\Delta\alpha(\hbar\omega, E_B) \propto \frac{1}{\theta(E_B)} F\left(\frac{\hbar\omega - E_g + i\Gamma}{\hbar\theta(E_B)}\right). \qquad (3.22)$$

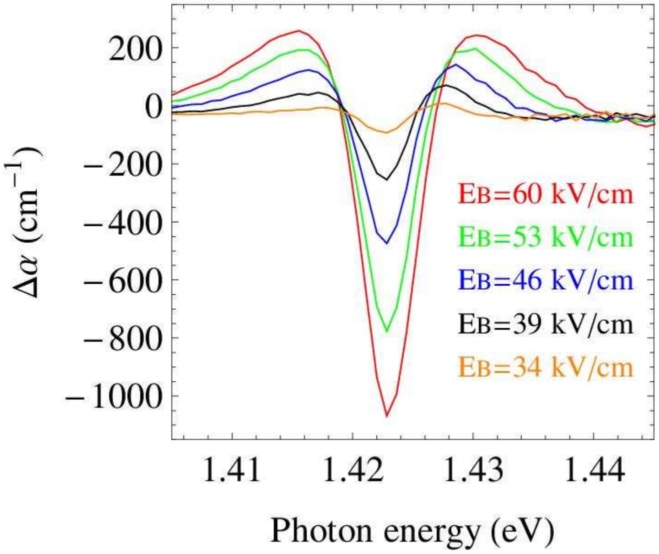

Figure 3.17. Evolution of the fundamental EA spectrum of GaAs with increasing electric field.

A spatial scan is shown in Figure 3.18 (a) with an average optical power of 30 nW. The EA signal is measured as a function of incident photon energy and the focal spot position on the sample. Here we modulate the bias between 0 V and 75 V at 50 Hz, the modulated EA signal is measured by the lock-in amplifier, and the DC signal on the photodiode is also recorded by a digital multimeter. We divide the modulated signal by the DC signal to give ΔT/T. Then the modulated absorption $\Delta\alpha = -\log(\Delta T / T + 1) / L$, where L is the thickness of the sample. Since here we have a thin GaAs layer with Au electrodes in direct contact, in Figure 3.18 (a), most of the EA signal is concentrated near the positively biased electrode edge (around 150 μm), due to the trap-enhanced electric field effect [9].

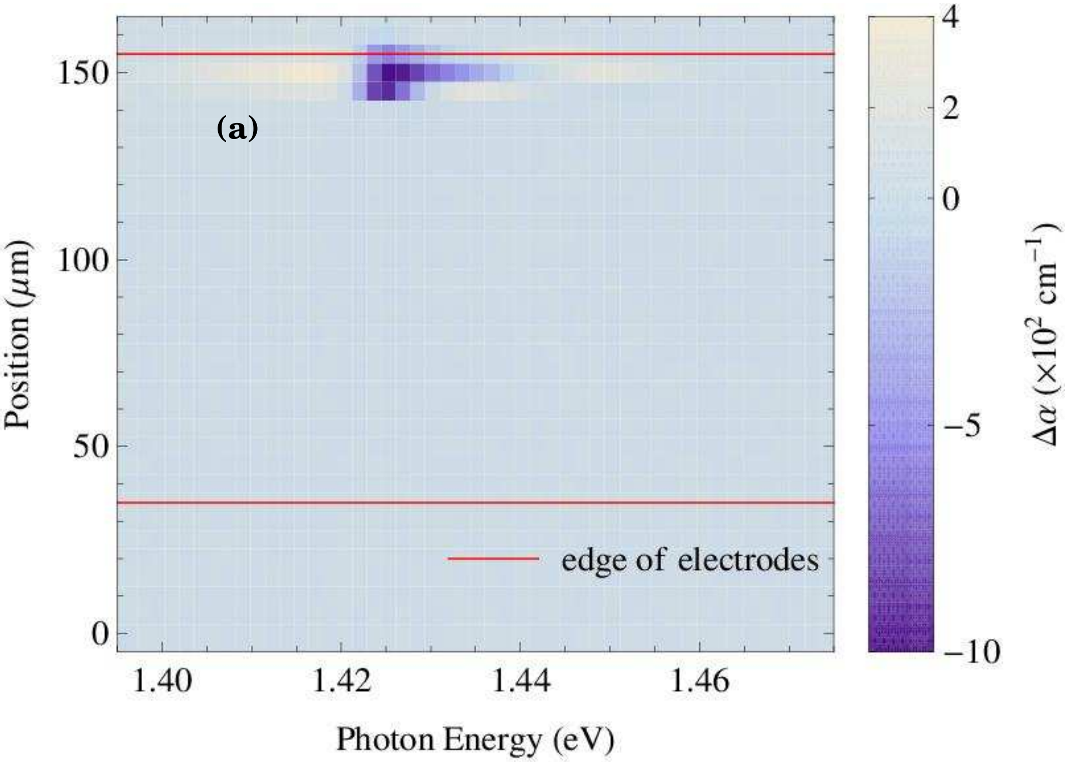

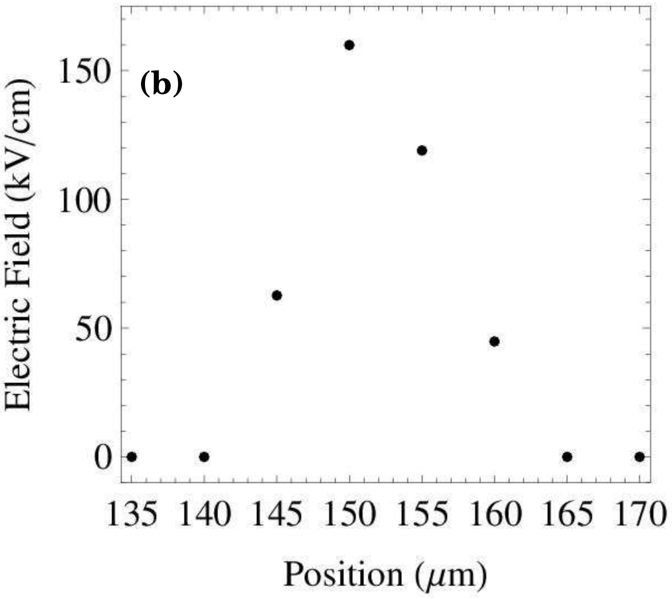

Figure 3.18. Spatial map of the EA signal and electric field in a GaAs sample with a 120 μm gap between electrodes. (a) EA spectra as a function of spot position at 75 V bias. (b) Electric field versus position near anode edge, found by analysis of the EA lineshape.

As with ER, by fitting our EA data to the theoretical EA lineshape based on the parabolic band approximation, the electric field distribution between electrodes was estimated. Similar to the ER case, rather than fit the entire lineshape, which is distorted by the nonuniformity of the field, we instead find the position of the first peak above the band gap. This first peak above gap is not strongly affected by either field inhomogeneity or broadening. The electric field strength is related to the difference between the peak position E_{peak} and the band gap energy by $E_B = [1052(E_{peak} - E_g)]^{3/2}$. Using the above relation we calculated the field distribution using the EA spectrum. The extracted electric field near the positively biased electrode edge as a function of position is shown in Figure 3.18 (b). The result, with strong trap-enhanced fields near anode edge, is very similar to the ER experiment as expected.

Due to field inhomogeneity and broadening, we find that the Franz-Keldysh oscillations above the bandgap were mostly washed out in our room temperature EA and ER experiments. Hoping to see more oscillations we also studied EA in a sample at low temperature. A cryostat which has AR coated windows on both sides was used to cool the GaAs sample with liquid helium. EA traces under different temperatures are shown in Figure 3.19, with incident beam power around 20 nW, and a 75 V bias modulated at 50 Hz. With temperature decreasing, crystal lattice spacing shrinks. Thus the bandgap energy of GaAs increases and the EA traces show up at higher energy. A sharp exciton (caused by the attraction between the photoexcited electron and hole) feature appears when the temperature is around 100 K, and this makes it harder to understand the current data since the simple theory does not account for the electron-hole interaction. This indicates that a stronger electric field is possibly required to separate the Franz-Keldysh oscillations from the excitonic effect [83].

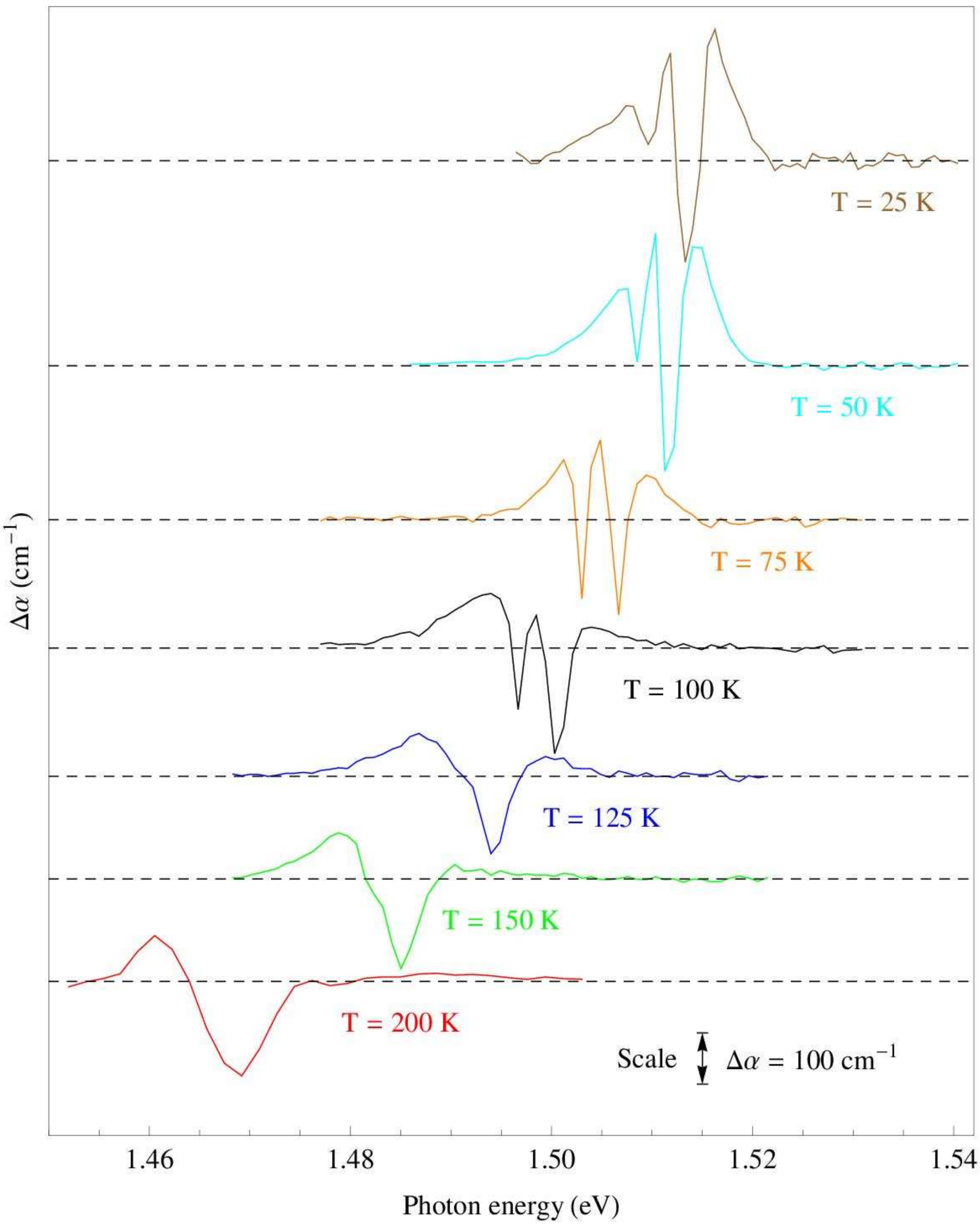

Figure 3.19. The shifting of the EA spectrum near the fundamental bandgap of GaAs with decreasing temperature.

We also performed two dimensional spatial scans under low temperature by moving the cryostat with the sample inside and recording the EA spectrum as a function of laser focal spot position. The plots of EA signal versus position at three different temperatures are shown in Figure 3.20. The red lines indicate the edge of electrodes on GaAs surface. The positive biased electrode edges are around 20 μm,

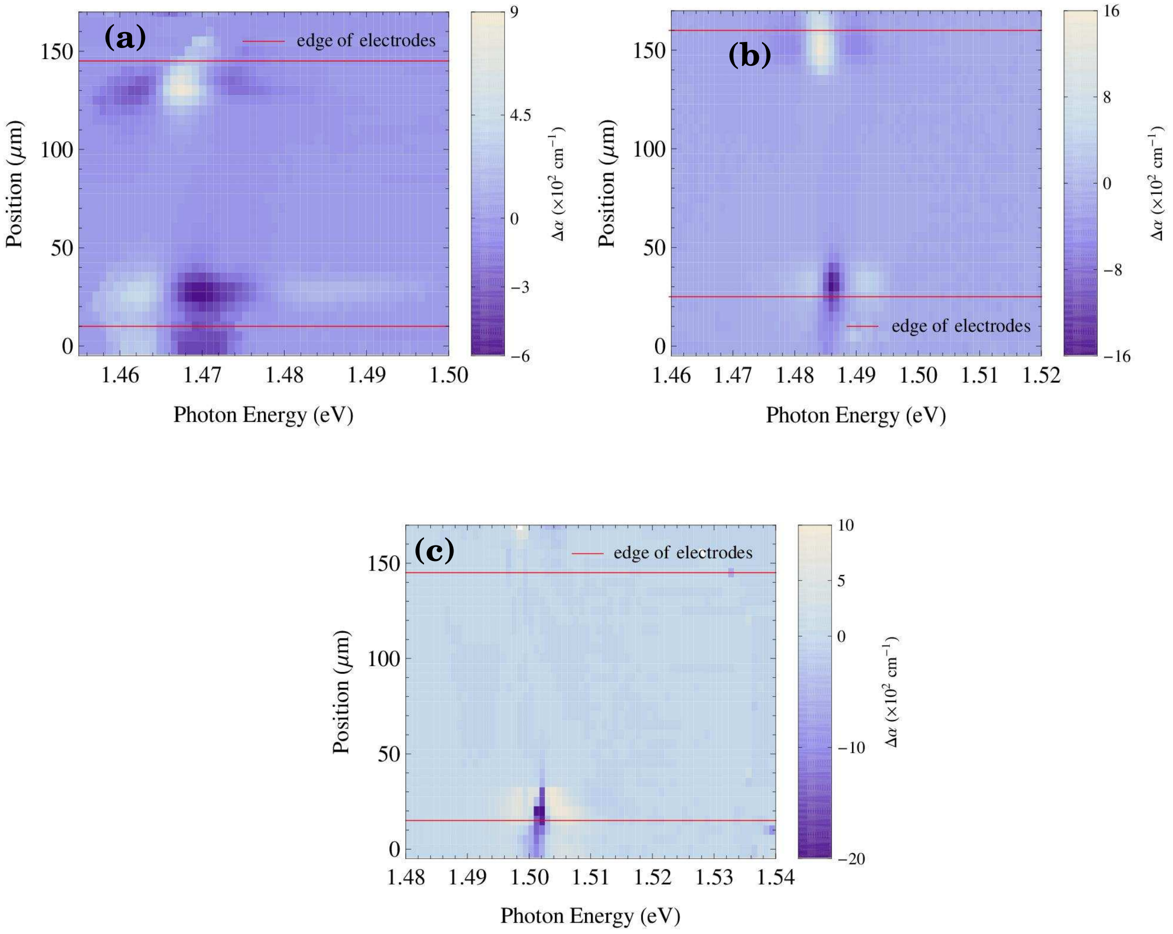

Figure 3.20 Two dimensional plot of EA spectrum vs. laser spot position, under low temperature. (a) 200 K (b) 150 K; (c) 100 K

with EA signal concentrated near these regions, probably due to the electric field inhomogeneity caused by the trap-enhanced field effect. However, at 200 K and 150 K, EA signal also shows up near the cathode edge which can not be only explained by the trap-enhanced field, but disappears at 100 K. We do not have a good explanation for the low temperature EA signal distribution at this point, and we haven't seen more oscillations as expected. Furthermore, the ice on the window of the cryostat and other issues like the thermal expansion of the wax layer make our EA signal not perfectly repeatable. The EA experiment under low temperature still needs further technical improvement. Ideally, the RF bias technique could be adapted to a low temperature experiment so that a uniform field could be achieved. This might require somehow mounting an LC circuit on the sample holder inside the cryostat.

3.6 Summary

In this chapter, our experimental results of transverse electroreflectance and electroabsorption were discussed. By using a radio frequency bias combined with a sample whose Au electrodes are insulated from the GaAs surface, we successfully minimized the trap-enhanced field effect and achieved a uniform electric field distribution, as measured by ER under relatively low optical power. We compared our ER results using the RF technique side by side with the conventional transverse ER using DC bias, and also presented further studies such as bias dependence, optical power and polarization dependence. Furthermore, we showed our DC bias EA result from a 1 μm thick GaAs epilayer. The EA results are similar to the ER, but with a better signal-to-noise ratio. The low temperature EA data is not fully understood at this point. Further study and improvement of the experimental apparatus is required.

CHAPTER 4

Terahertz generation with RF technique

An important ultrafast optical application of biased M-S-M structures is the generation of broadband THz pulses. The application of the RF bias technique to this problem is the subject of this chapter.

We start with a brief introduction about photoconductive terahertz (THz) generation, and the electro-optic sampling detection system we use to measure THz emission. Then the key limiting factor of photoconductive THz generation efficiency, ultrafast screening of the applied electric field, is discussed. Finally we show experimental results using the RF bias technique, and compare our data with DC bias results. As discussed in previous chapters, the RF bias technique and sample with insulated electrodes allow application of a strong, effectively constant field without carrier injection from the electrodes, and thus the trap-enhanced electric field does not form. The resulting uniform electric field distribution allows excitation with a large laser spot, lowering the photo-injected carrier density for a given pulse energy and increasing the pulse energy at which ultrafast screening of the field during the laser pulse occurs. Furthermore, the insulated electrodes sample shows less susceptibility to damage. Our RF technique shows the potential for further improvement if a more powerful RF power amplifier is available. For comparison, previous results of THz generation using low temperature grown GaAs (LT-GaAs) are discussed.

4.1 Terahertz generation from photoconductive antenna

Ultrafast broadband terahertz radiation, which refers to electromagnetic waves at frequencies between 0.3 and 10 THz, has been exploited for a variety of applications including imaging, sensing, and spectroscopy [42]. One of the most widely used sources for THz radiation [54] is a biased photoconductive switch: a semiconductor, such as GaAs, with metal electrodes on the surface, which is excited by ultrafast optical pulses from a mode-locked laser. Although higher peak THz fields can be achieved using amplified laser systems that operate at kilohertz repetition rates, for spectroscopy applications sources employing oscillators with repetition rates near 100 MHz are attractive for their better noise performance, relative simplicity and lower cost. The transverse electrode sample geometry which we used to study electroreflectance can also work as a photoconductive dipole antenna for THz generation.

The GaAs based photoconductive THz emitter relies on the absorption of ultrashort pump pulses with a photon energy above the bandgap in order to generate electron-hole pairs. In undoped GaAs, the creation of photocarriers by ultrashort optical pulses gives rise to a sudden, many orders of magnitude, change in the electrical resistance. Because the GaAs is biased with a static electric field, the change in its resistance will lead to a current that has a strong time dependence, radiating electromagnetic waves in the THz frequency range. A diagram of a typical THz photoconductive switch (sometimes called an antenna) with a DC bias applied to its electrodes is shown in Figure 4.1. It is comprised of a GaAs substrate with metal electrodes deposited on the surface. A laser beam is focused to a spot within the gap between the electrodes to create free carriers in the GaAs substrate. A DC bias is applied to the electrodes to create a constant electric field in the gap.

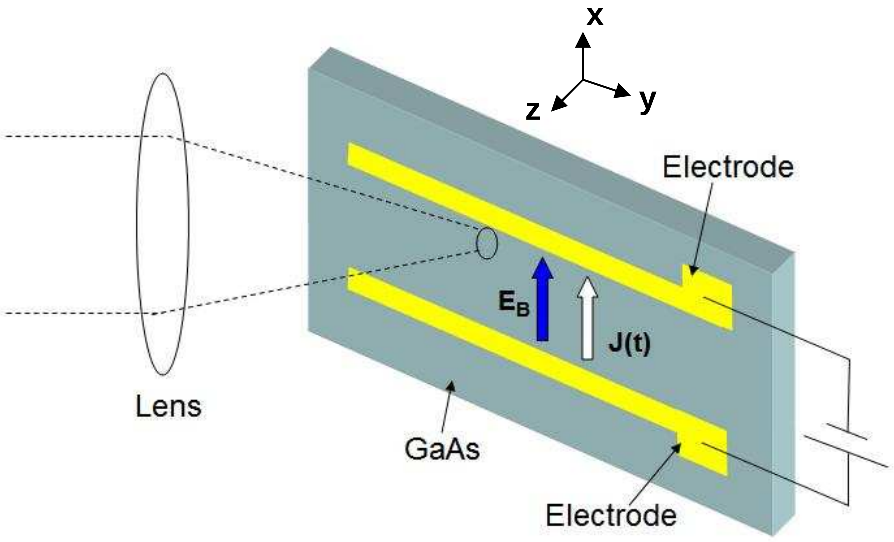

Figure 4.1: Schematic of a GaAs based photoconductive switch for THz generation. E_B is the applied static electric field, j(t) is the time dependent current density.

The laser beam creates a time-dependent photocarrier population in the GaAs substrate. Neglecting the background carrier density, the rate of change of the carrier density n is

$$\frac{dn(t)}{dt} = -\frac{n(t)}{\tau_c} + G(t,z)\,, \tag{4.1}$$

where τ_c is the carrier lifetime, z is the propagation distance of the laser pulses, and $G(t,z)$ is the optically injected carrier generation rate, at the surface of the GaAs substrate, it is [54]

$$G(t, z=0) = G(t) = \alpha \cdot \frac{I(t)}{\hbar\omega}\,, \tag{4.2}$$

here α is the absorption coefficient of GaAs and ħω is the incident photon energy. Assuming a Gaussian pulse with pulse duration τ_p, the laser intensity is

$$I(t) = I_0 \exp\left(\frac{-\ln 2 \cdot t^2}{\tau_p^2}\right). \tag{4.3}$$

Here assume α is constant, and one absorbed photon generates one electron-hole pair. Since the carrier lifetime τ_c (~10 ns in SI-GaAs, a few 100's of fs for LT-GaAs) is much longer than the pulse duration, the approximate solution of Eq. (4.1) is

$$n(t) = e^{-\frac{t}{\tau_c}} \int_{-\infty}^{t} G(t) \cdot e^{\frac{t}{\tau_c}} dt = \int_0^t G(t) dt - N_0 \cdot e^{-\frac{t}{\tau_c}}. \tag{4.4}$$

The first term refers to the change in carrier density within the laser pulse duration, and the second term refers to the carrier density change after the laser pulse. N_0 is the bulk carrier density without illumination.

Before excitation there are almost no free carriers present, so even with a strong applied bias field E_B, the current is essentially zero. After excitation, the pulse generates electron-hole pairs and the conductivity σ of the GaAs is increased dramatically,

$$\sigma(t) = n(t) \cdot e \cdot \mu , \tag{4.5}$$

where by definition $\mu = V_d / E_B$ (V_d: drift velocity) is the usual mobility of free carriers. The time dependent current density is

$$j(t) = \sigma(t) \cdot E(t) = \sigma(t) \cdot [E_B + E_{THz}(t)]. \tag{4.6}$$

This current is driven by the total field $E(t)$ in the semiconductor [54], which consists of the applied electric field E_B plus the generated THz field $E_{THz}(t)$.

Only nonmagnetic material is considered here, thus $B = \mu \bullet H$ everywhere. According to Maxwell's equations,

$$\nabla \times \vec{E}(t) = -\mu \frac{\partial \vec{H}(t)}{\partial t}, \tag{4.7}$$

$$\nabla \cdot \vec{H}(t) = j(t) + \frac{\partial}{\partial t}[\varepsilon_r \varepsilon_0 \vec{E}(t)]. \tag{4.8}$$

Inside the semiconductor, assume $D = \varepsilon_r \varepsilon_0 E$ by neglecting dispersion and nonlinear effects. From Eq. (4.7) and Eq. (4.8), one can derive [54]

$$E(t) = -\frac{\mu \cdot c}{1+\sqrt{\varepsilon_r}} \cdot j(t), \tag{4.9}$$

$$B(t) = -\frac{\mu}{1+\sqrt{\varepsilon_r}} \cdot j(t), \tag{4.10}$$

where c is the speed of light in vacuum. To obtain the THz field transient, use Eq. (4.9) in Eq. (4.6),

$$j(t) = \sigma(t) \cdot [E_B - \frac{\mu \cdot c}{1+\sqrt{\varepsilon_r}} \cdot j(t)], \tag{4.11}$$

and solving for $j(t)$ gives

$$j(t) = \frac{\sigma(t) \cdot (1+\sqrt{\varepsilon_r})}{1+\sqrt{\varepsilon_r} + \sigma(t) \cdot \mu \cdot c} \cdot E_B. \tag{4.12}$$

Inserting the expression for $j(t)$ into Eq. (4.9) gives

$$E(t) = E_B + E_{THz}(t) = -\frac{\mu \cdot c \cdot \sigma(t)}{1+\sqrt{\varepsilon_r} + \mu \cdot c \cdot \sigma(t)} \cdot E_B \,. \qquad (4.13)$$

The THz near field is roughly Gaussian. Taking into account the carrier lifetime and mobility, the THz far field is a single cycle pulse of a few hundred femtoseconds duration.

Summarizing the processes described above, THz generation from a semiconductor based photoconductive antenna with external bias can be thought of as occurring in a few steps. First of all, an optical pulse creates carriers in a semiconductor with static bias field. The photoinjected electrons and holes are accelerated in the DC field, moving in opposite directions and creating a current transient. The time dependent current leads to a transient THz electric field which is roughly the time derivative of the current. In the case of strong illumination, photocarriers of very high density can be created, and carrier separation by the bias field can build up an opposing field to screen the applied DC field. It will be shown later that this screening process limits the strength of the THz field that can be achieved using this technique. These processes all happen within less than a picosecond. On the much longer time scale of approximately 10 ns between the laser pulses, the photocarriers can either recombine or travel to the electrodes, and the THz emitter system goes back to its initial state, ready to repeat these processes again.

4.2 Electro-optic sampling detection system

In time domain THz spectroscopy, the amplitude and phase of a THz pulse are measured as a function of time after it transmits through a sample. This allows the full characterization of the THz response of the sample [54]. This technique works because one can easily measure the THz electric field. Two types of time-gated THz pulse detection schemes have been widely used. One is based on a semiconductor photoconductive antenna, and the detection mechanism, which based on the fact that a current transient can be detected when photo-injected carriers in a photoconductive antenna is driven by the THz field, is very similar to the mechanism used to generate THz pulses discussed in previous section. The other one is based on the electro-optic effect, in which an electric field applied to a nonlinear crystal leads to a change in its refractive index. We use the second scheme, which is usually called electro-optic (EO) sampling, in our experiments for detecting free space THz radiation.

Figure 4.2 shows a schematic diagram of an EO sampling system. Here a linearly polarized beam from the same Ti:sapphire laser that is the light source for generating THz radiation is used as a probe beam for EO sampling. The THz radiation generated from the photoconductive antenna and the probe beam are carefully aligned to propagate in the same direction through the nonlinear crystal (a 1 mm thick (110) oriented ZnTe crystal is used in the experiments). The THz field can induce birefringence in the ZnTe crystal, which induces a small ellipticity in the probe polarization that is proportional to the THz field. Following the ZnTe crystal there is a $\lambda/4$ waveplate and a Wollaston prism. Two orthogonally polarized components of the probe beam after the Wollaston prism are focused separately onto two photodiodes of a balanced photodetector. The time delay between the THz pulse and the optical probe pulse is controlled by a retroreflector mounted on a translation stage driven by a stepper motor in the probe beam path (not shown in the figure).

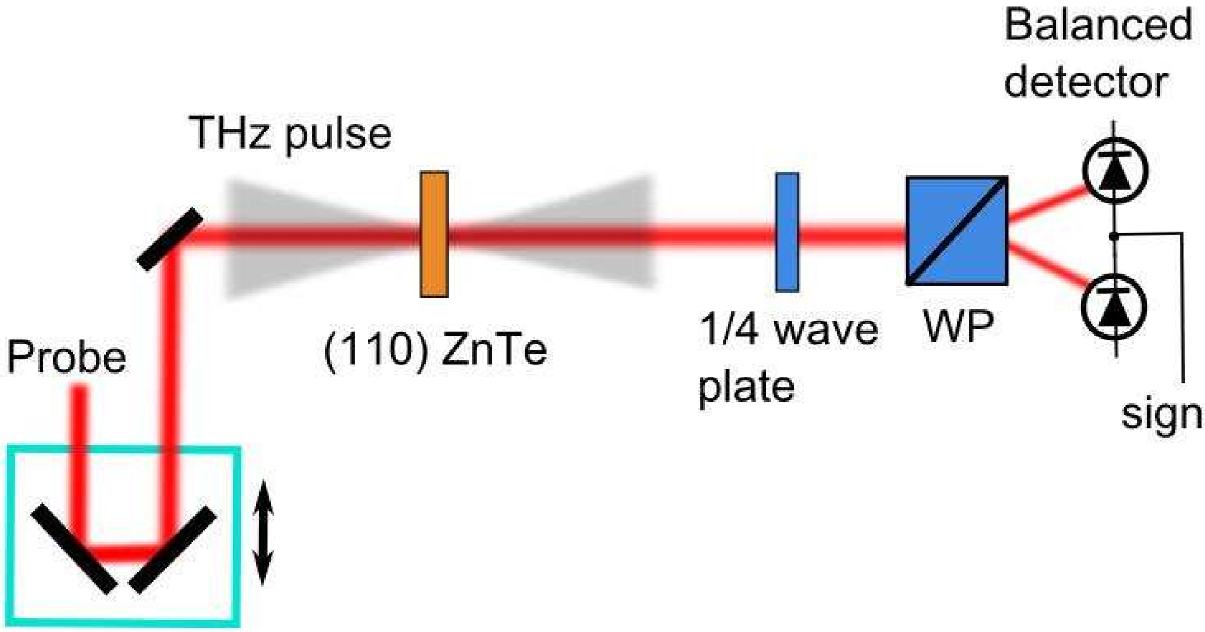

Figure 4.2: Schematic of a typical electro-optic (EO) sampling system for detection of ultrashort THz pulses.

When the THz field and the probe pulse do not temporally overlap in the ZnTe crystal, as shown in Figure 4.3 (a), there is no field induced birefringence, and the probe beam polarization remains unchanged. After the $\lambda/4$ waveplate, the probe beam will be circularly polarized, and two equal polarization components of the probe will be separated by the Wollaston prism, and thus the output of the balanced detector is zero [55]. The amount of ellipticity is linear in the THz field, and thus so is the voltage on the balanced detector. By scanning the delay between the THz pulse and probe pulse, the THz electric field can be mapped out as a function of time.

As shown schematically in Figure 4.3 (b) and (c), by changing the time delay, the positive or negative part of the THz field overlaps the probe pulse in –y direction in the ZnTe crystal, the THz electric field can induce birefringence in the crystal based on the second order nonlinear effect, and this leads to a polarization rotation of the probe pulse. The field induced change in refractive index of ZnTe is $\Delta n = r_{41}\, n^3 E_{\mathrm{THz}}$, where n is the linear refractive index and r_{41} is a component of the electro-optic tensor. The phase shift of the probe pulse is [56]

$$\Delta\varphi_{THz}(\omega) = \frac{\omega}{c} n^3 r_{41} E_{THz}(\omega) L\,, \tag{4.15}$$

where L is the thickness of the ZnTe crystal. With a phase change $\Delta\phi_{THz}(\omega)$ in the probe polarization, after the λ/4 waveplate, the field component of the probe pulse in y direction has a $\pi/2$ phase shift, which makes the probe polarization slightly elliptical. After the Wollaston prism, the two orthogonally polarized components have slightly different intensities which can be detected. The intensity difference on the balanced photodetector is [57]

$$S = I_1 - I_2 = \varepsilon_0 c \operatorname{Re}\int_0^{\infty} \left|a_0(\omega)\right|^2 \Delta\phi_{THz}(\omega) d\omega\,, \tag{4.16}$$

where c is the speed of light, ε_0 is the dielectric constant, and $a_0(\omega)$ is the amplitude of the probe optical field, $a_0(\omega) = A_{probe}(\omega)\exp[ik(\omega)L]$. We see that the output signal from the balanced detector is proportional to the actual THz electric field and the length of the crystal. In practice, dispersion in the crystal results in some distortion in the measured THz pulse shape, particularly for thick crystals or extremely short THz pulses. A complete description of EO sampling in the frequency domain is given in Reference [57].

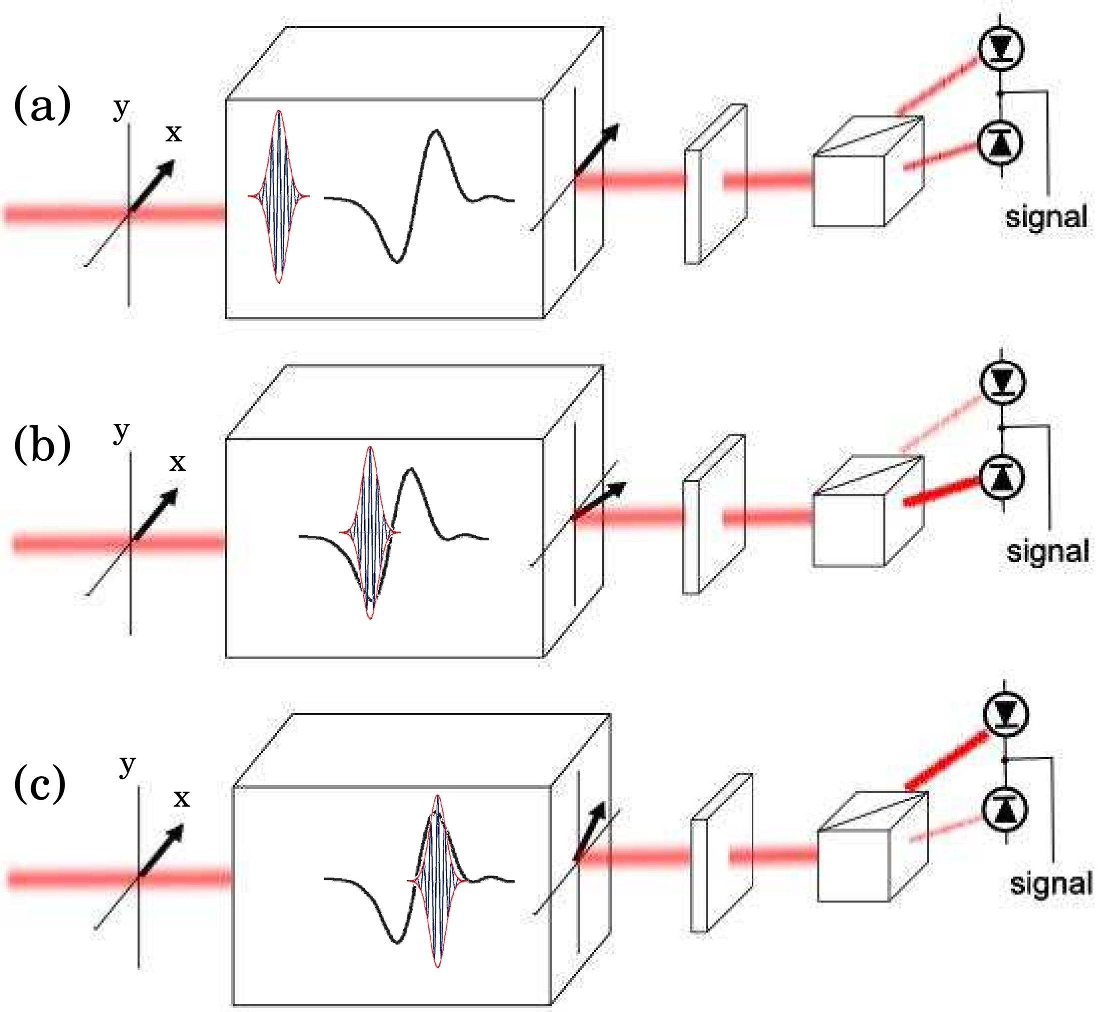

Figure 4.3: EO sampling with three relative delays between the THz pulse and the probe pulse, showing how the signal on the balanced detector changes depending on the sign of the THz field overlapping with the probe pulse.

4.3 Carrier screening and THz power saturation

Generation of THz radiation from a biased photoconductive antenna is useful because of its good noise performance and relative simplicity at low cost.

However, the optical-to-THz conversion efficiency is very small (typically ~0.002%) [58]. A number of different emitter designs and biasing techniques have been explored to improve the conversion efficiency of the photoconductive THz antenna. These include so-called “semilarge” emitters using widely spaced electrodes, high voltage bias, and high optical power [59]; emitters using lower bias, tight focusing, and strong trap enhanced fields [9,58]; and emitters with interdigitated, closely spaced electrodes, with half of the gaps blocked [60]. Because they do not require high voltage or special electrode structures, emitters based on trap-enhanced fields are attractively simple. The key limitation is ultrafast screening of the applied field by photoinjected carriers [23,43,58]. This screening depends strongly on the laser excitation spot size, becoming less important for a larger spot.

As discussed previously, in a biased photoconductive antenna the acceleration of photocarriers induced by the bias electric field gives rise to the THz emission. At the same time, the carriers moving in the bias field can partially screen out the bias [23]. The screening of the bias field can be classified into two main categories: direct Coulomb screening from the separation of the photocarriers, and radiation screening from the generated THz radiation itself [61,62]. Both of the two screening effects are related to the spatial dynamics of the carriers, such as their velocity and acceleration in the applied electric field. Consider a point charge moving with velocity v and acceleration a in a bias field, the electric field it generates is [63]:

$$E = \frac{q}{4\pi\varepsilon}\left(\frac{1}{\left|1-\hat{R}\cdot v/c\right|^{3}} \left\{ \frac{(1-v^{2}/c^{2})(\hat{R}-v/c)}{R^{2}} + \frac{\hat{R}\times[(\hat{R}-v/c)\times a]}{c^{2}R} \right\} \right)_{t_r} , \qquad (4.17)$$

where R is the position vector directed from charge q to the point of observation, c is the speed of light and ε is the permittivity of the medium. The position vector, velocity and acceleration are evaluated at the retarded time $t_r = t - R/c$. When the drift velocity of the photocarriers is much less than the speed of light, the electric field in Eq. (4.16) can be split into two parts: the contribution of the radiation field (E_r) and Coulomb field (E_c) [63,64]

$$E \cong E_c + E_r = \frac{q}{4\pi\varepsilon}\left(\frac{\hat{R}}{R^2}\right)_{t_r} + \frac{q}{4\pi\varepsilon c^2}\left(\frac{\hat{R}\times(\hat{R}\times a)}{R}\right)_{t_r} \tag{4.18}$$

Both the Coulomb field, which is induced by charge separation, and the radiation field, which is from the acceleration of charges, are in the opposite direction to the applied bias field, and thus contribute to the reduction of the effective carrier-driving electric field in a photoconductive antenna. When the screening field approaches the external bias field within the time scale of the optical pulse, the THz emission is suppressed. In a typical experiment, when the excitation spot size is fixed, with increasing optical power, the increase in carrier density leads to a rapid decrease in the distance between carriers, and an increase in the number of carriers that contribute to the Coulomb screening, thus the Coulomb screening field increases with increasing optical power. Further more, under higher carrier density, the radiation screening also gets stronger due to the carrier numbers which contributes to the radiation screening also increase. As a result, the THz radiation saturates quickly under high optical excitation power. For a fixed optical power/carrier density, the Coulomb screening is dominant when the excitation spot size is no larger than 100 μm FWHM (this value probably depends somewhat on the THz wavelength), and when the spot size is larger than 100 μm, radiation screening dominates [23]. On the other hand, under a given optical power, one can decrease the carrier density by using a large excitation spot. A bigger spot leads to an increasing distance between carriers and a decreasing number of carriers that contribute to the Coulomb and radiation screening field [23,43,58].

Due to their strong dependence on carrier density, both Coulomb and radiation screening field decrease with increasing excitation spot size. As a result, one can think about improving the optical power-to-THz conversion efficiency by minimizing the screening field with larger excitation spot. However, simply increasing the excitation spot size is not the best option, since the electric field in a typical M-S-M structure THz emitter is strongly enhanced only within a few microns near the anode edge due to the trap-enhanced field (TEF) [9]. If a large spot size means only a small portion of the excitation spot can overlap with the narrow TEF region, the THz generation efficiency will be strongly compromised. Thus in previous studies, an elliptical focusing technique was adopted to obtain effective THz generation using a maximally broadened excitation aperture in the TEF region [23,58].

4.4 RF bias THz generation

Instead of using an elliptical laser spot [23,58] or a complicated electrode structure that lowers the effective active area of the device [60], here we use the RF biasing technique, which results in a uniform electric field across the sample. Unlike the trap-enhanced field device, using a large laser excitation spot with an RF bias does not lower the average field within the laser spot. The large spot increases the saturation threshold of optical excitation, and there are a number of other advantages as well.

4.4.1 Experimental layout

We use a simple electrode structure that is insulated from the sample, as described in Chapter 2, and rapidly oscillate the bias at a frequency near the laser repetition rate to prevent the screening of the field by space charge during the time between pulses. Although an oscillating bias has been used at lower repetition rates corresponding to amplified laser systems [65], as far as we know it had not been previously scaled up to the repetition rates of Ti:sapphire or fiber oscillators.

Figure 4.4 shows a schematic of the THz generation and detection apparatus. The light source is the same mode-locked Ti:sapphire laser we used in our ER and EA experiments, with a spectrum centered at 830 nm, a FWHM of 50 nm, and a repetition rate f_{rep} = 89 MHz. The pulse energy is 5.5 nJ with about 70 fs duration. The laser beam is divided by a beam splitter, one output of which is used to pump the photoconductive emitter. The other output is used as the probe pulse in an EO sampling system using a 1-mm-thick ZnTe (110) crystal. The emitter is a bulk semi-insulating (100)-oriented GaAs wafer, with a 100-nm-thick layer of silicon oxide on the surface as an insulating layer, and Au electrodes separated by 100 μm on top of the insulating layer. More details about the sample structure were discussed in Chapter 2. The THz radiation from the photoconductive antenna passes through the back of the sample with a silicon hemisphere lens attached for better output coupling and THz collection efficiency, and is collected and focused into the EO sampling system by a pair of parabolic reflectors. The probe beam is directed into the ZnTe crystal using a mirror mounted on a long post. This blocks a small portion of the THz beam.

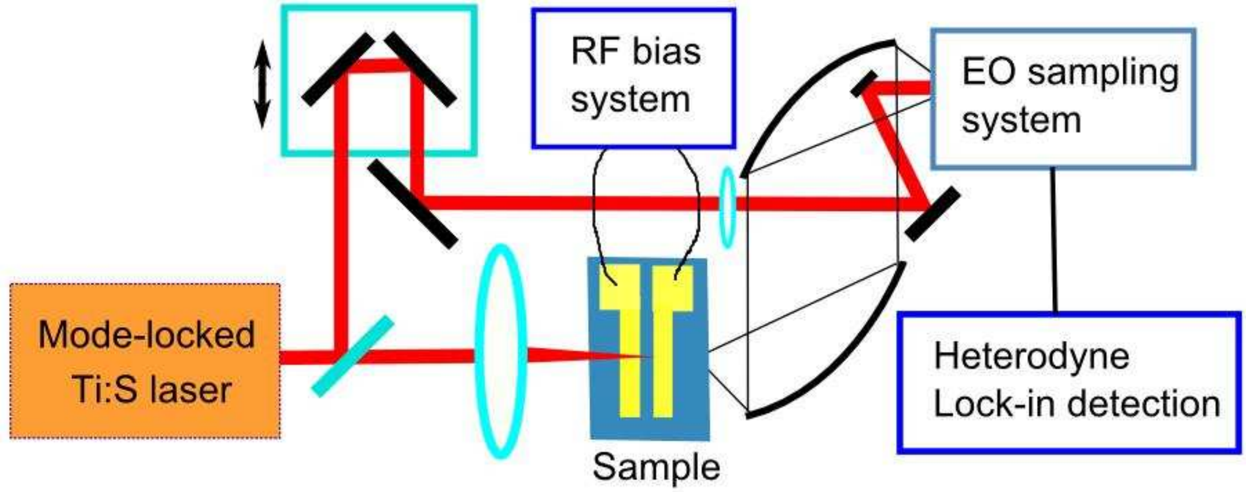

Figure 4.4: Radio-frequency biased THz generation apparatus, showing both the emitter and the EO sampling system.

A radio-frequency bias is applied across the electrodes with a frequency f near the laser repetition rate. The THz signal is modulated at the difference between the RF bias frequency and the laser repetition rate, and that difference can be set to any frequency. We use a modulation frequency in the kHz frequency range, where the lock-in amplifier has the best performance. More information about the RF bias and heterodyne detection system can be found in Chapter 2 and Appendix A.

4.4.2 Optical power dependence and bias dependence

As demonstrated in the previous chapter, because the electrodes are insulated from the GaAs sample, current injection and the resulting trap-enhanced fields do not form [24]. Although the bias field strength we have been able to generate (~10 kV/cm at 89 MHz and ~30 kV/cm at 45 MHz as measured by electroreflectance [24]) using the RF bias technique is not as strong as the localized trap-enhanced fields seen in samples with DC bias (~200 kV/cm) [9], the area over which the electric field extends is considerably larger, essentially the entire region between the electrodes. One can therefore use a much larger laser spot size, resulting in a higher saturation threshold for the THz power emitted as a function of optical pump power. The electroreflectance data presented in [24] were acquired using very low optical powers in the nanowatt range, whereas to generate significant THz power, much larger optical powers in the milliwatt range must be used. Given the strong dependence of screening on the photoexcited carrier density, it is not obvious that the uniform field observed in electroreflectance will exist at high optical powers; however, our results confirm this fact. A typical THz trace, measured by EO sampling, obtained using the RF technique and the THz power spectrum, found by taking the discrete Fourier transform of the time domain data, are shown in Figure 4.5. The oscillations after the main THz pulse are caused by water absorption lines in the air as well as absorption and dispersion in the ZnTe crystal.

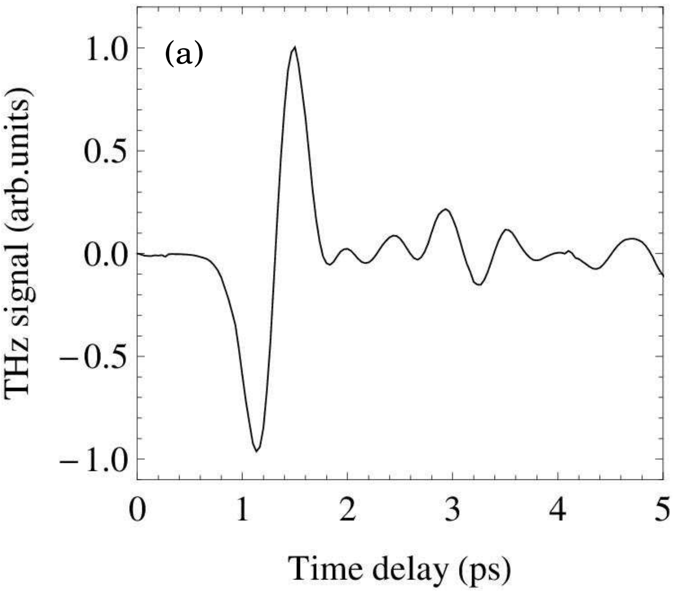

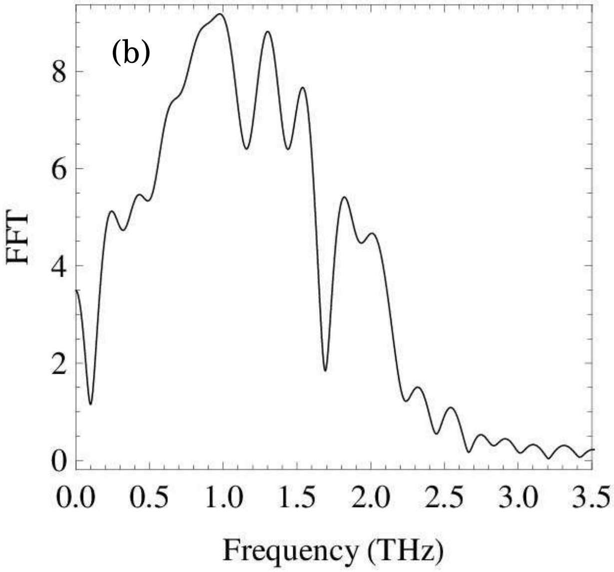

Figure 4.5: THz radiation signal measured using a photoconductive emitter with a radio frequency (RF) bias. (a) Typical THz trace. (b) THz spectrum.

The peak electric field can be found using Eq. (4.14) from the EO sampling signal. We find a peak THz field of 20 V/cm for an input power of 160 mW. Using an estimated spot size of 50 μm for the THz beam focused at the ZnTe crystal, our THz power is around 100 μW and the optical power-to-THz efficiency is close to 0.1%, this result is comparable with other techniques [58]. The maximum THz signal was found for a laser spot size of ~80 μm FWHM. We measured the dependence of the THz field on the optical power; the results are shown in Figure 4.6. For a large spot (~80 μm), shown as filled circles in Figure 4.6, we find a steadily increasing THz field, whereas for a small spot (~8 μm), shown as empty circles in Fig 4.6, we find saturation behavior. This behavior is consistent with theories of ultrafast screening [23,43,58], because screening is much stronger for a small excitation spot. The peak fluence at which saturation begins is consistent with previous studies [58].

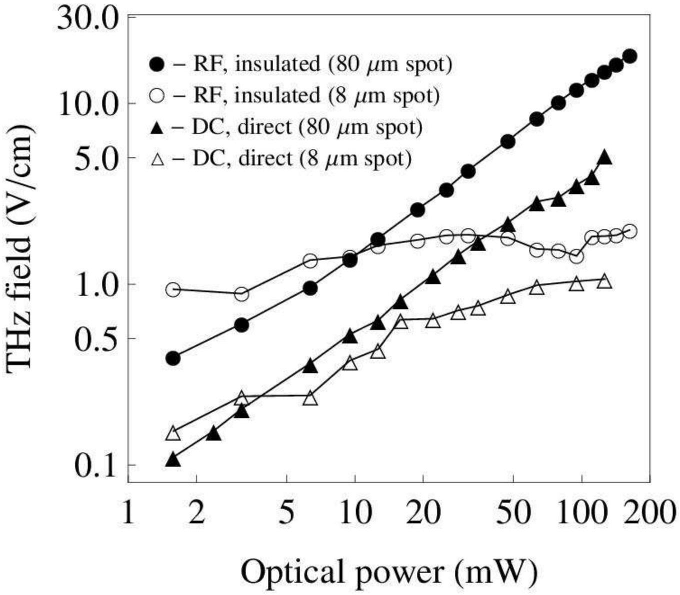

Figure 4.6: Dependence of peak THz field on optical power for various excitation geometries. Filled circles: large spot, RF technique; empty circles: small spot, RF technique; filled triangles: large spot, DC technique; empty triangles: small spot, DC technique.

The narrower emission pattern (and thus, better collection efficiency by the THz optics) for a larger excitation spot size may also explain part of the difference in the signal size between the dc and RF bias techniques. This is an important advantage, because in a typical spectroscopy apparatus, the THz is collected by similar optics and sent through a sample. It is much easier to collimate a THz source with a narrower emission pattern. We found that V_{mon}, which is the monitor for tuning the LC resonant circuit (as shown in Figure 2.5), was lower when the laser was on the sample than when there was no illumination, a sign that the presence of free carriers spoils the Q of the LC resonant circuit.

The bias dependence of the THz field strength generated by the RF technique, shown in Figure 4.7, shows a roughly linear dependence over the accessible range of RF powers, as the basic theory presented in Section 4.1 predicts.

This shows the potential for improved performance if the bias field can be increased, for instance by using a more powerful RF amplifier.

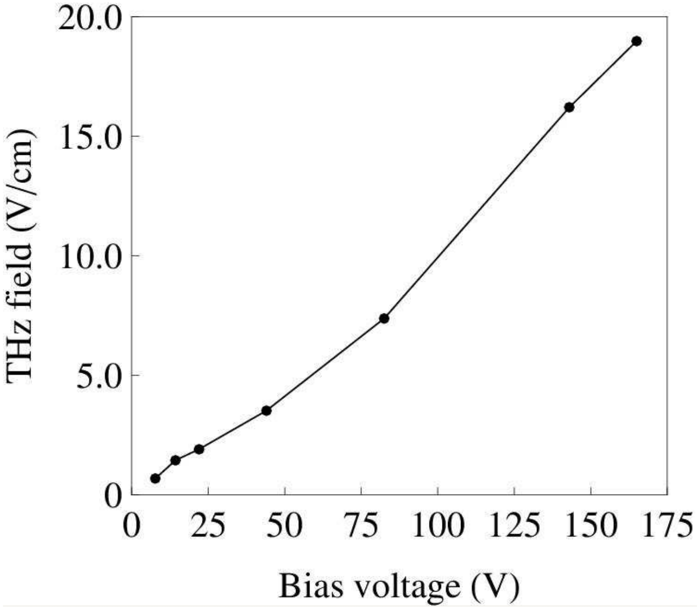

Figure 4.7: Dependence of the peak THz field on the bias voltage using the RF technique.

.

To investigate the role of carrier injection in these structures, we compared emitters with insulated electrodes to emitters with an identical electrode pattern, but no insulating layer. With an RF bias, the direct contact samples show a similar power and bias dependence but are susceptible to failure at the highest optical power and largest bias. Examination under a microscope revealed damage where the laser was focused, the migration of the gold across the gap has shorted out the electrodes. With a constant bias of 40 V, we find a smaller THz field, which can be partially explained by the fact that the THz was emitted only from the region of the sample near the electrodes. The samples with a dc bias also showed susceptibility to failure. The insulated samples showed no signs of damage after long term operation at the highest optical and RF power, which is an important advantage over typical photoconductive emitter designs.

4.4.3 Spatial dependence of the THz field

To investigate the field distribution in the presence of strong optical excitation, we also examined the dependence of the signal on the position of the laser spot (of width 8 μm) on the emitter. By scanning the sample under the laser spot with a stepper motor, the peak THz field as a function of the spot position between the two Au electrodes was measured. Results are shown in Figure 4.8. We compared the insulated, RF-biased emitter with an emitter with direct contacts with a constant bias of 40 V. The RF bias produces a more uniform field distribution, as measured by the THz emission (which is proportional to the bias field). The emitters with direct contacts showed the trap-enhanced field effect, with THz emission peaked near the anode [9]. We found, interestingly, that for RF bias, the emission was peaked near the electrodes at low optical power, but very uniform across the sample at high optical power. Neither of these results is consistent with the distribution measured by electroreflectance at very low optical power [24], which, as discussed in the previous chapter, was consistent with a calculation for a perfect dielectric with this electrode geometry [39]. The high-field dynamics of carriers and the effect of the electrodes on the screening are probably involved; more theoretical work is needed.

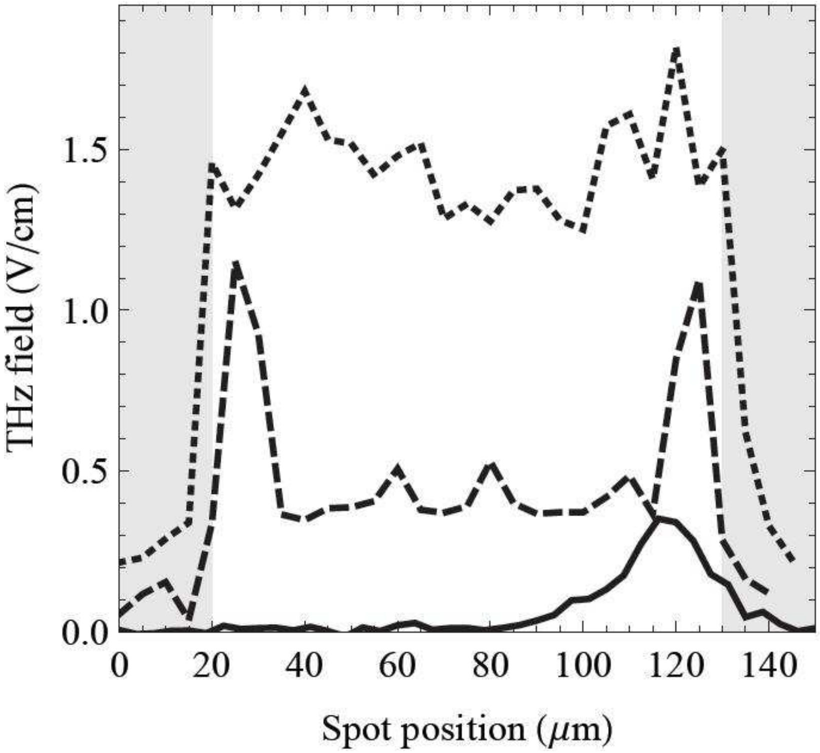

Figure 4.8: Dependence of the THz peak field on the position of the laser spot for a focus of 8 μm; the shaded region corresponds to the gold electrodes. Short dash, RF-insulated high optical power (150 mW); long dash, RF-insulated low optical power (15 mW); solid line, dc direct low optical power (15 mW).

4.5 THz generation and electroreflectance in LT-GaAs

Evidence from electroreflectance (ER) and THz emission has been given for the trap-enhanced field in a DC biased sample in the previous chapter and this one. But one may wonder, how well does the field measured by ER correlate with the spatial dependence of the THz emission? We decided to measure ER and the THz radiation from the same sample simultaneously to answer this question. For this experiment, low temperature-grown (LT) GaAs was used because it makes a more reliable THz emitter. The unique properties of low-temperature-grown GaAs (LT-GaAs), such as subpicosecond carrier lifetime, large resistance and high carrier mobility, make it one of the most widely used materials in photoconductive THz emitters [64,66].

Light from the Ti:sapphire laser, the same one we used in our ER and THz generation experiments using SI-GaAs, is focused onto the LT-GaAs sample by a microscope objective. The focal spot size was measured to be approximately 5 μm FWHM. The back-reflected light from the sample is collected by a beamsplitter, narrowed by a monochromator to about 1 nm bandwidth (with a variable wavelength), and then focused on a photodiode which measures ΔR at the modulation frequency of the bias field. Note that, unlike in the ER measurements described in the previous chapter, here we excite with a broadband pulse and monochromatize after reflection from the sample. The theory predicts an identical ER spectrum; one normally narrows the spectrum first so that the optical power at the sample is minimized, but here a broadband pulse is required to create THz radiation. On the back side of the sample, the emitted THz radiation is collimated and focused by the off-axis parabolic mirrors into an electro-optic (EO) sampling system. The sample is mounted on a stepper motor in order to examine the laser spot position dependence of the ER signal and the peak THz field. A schematic plot of the experimental setup is shown in Figure 4.9.

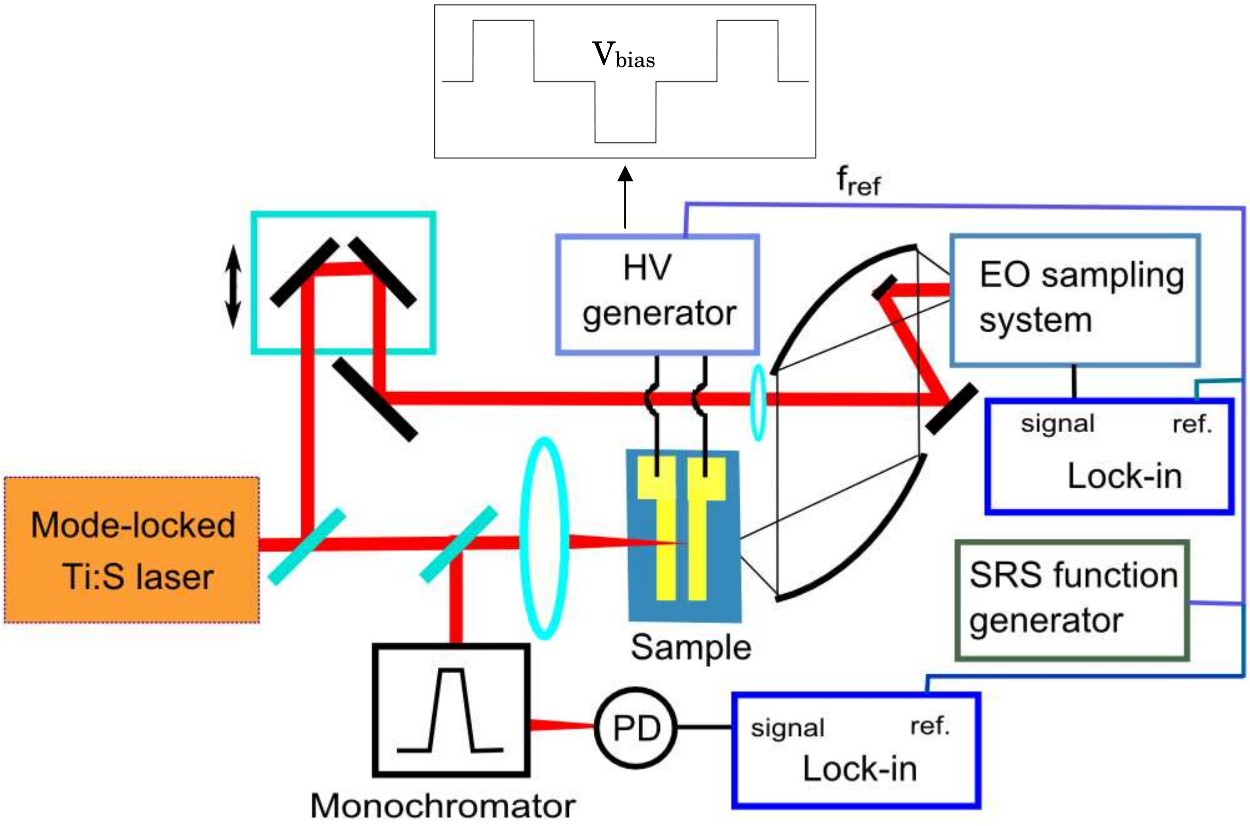

Figure 4.9: Experimental apparatus for simultaneous ER and THz measurement in LT-GaAs.

The LT-GaAs sample was grown by Dr. Richard Mirin at NIST. It consists of a 1.8 μm layer of GaAs grown at 400 ^{o}C on a semi-insulating GaAs substrate with no buffer layer. Gold electrodes with 180 μm spacing are evaporated on the LT-GaAs surface directly. The gap between two electrodes is made by a very thin wire which acts as a shadow mask. A bipolar square waveform bias changing from 0 V to a positive value, then back to 0 V, then a negative value, is applied to the sample with a repetition frequency of 1 kHz. The amplitude of the positive and negative square wave can be adjusted anywhere between 0 V and 500 V. This special waveform is supposed to give a more uniform electric field, according to reference [7]. The EO sampling signal was detected by a lock-in amplifier referenced to 1 kHz, while the field induced change in reflectance ΔR was measured using a second lock-in amplifier referenced to the second harmonic of 1 kHz.

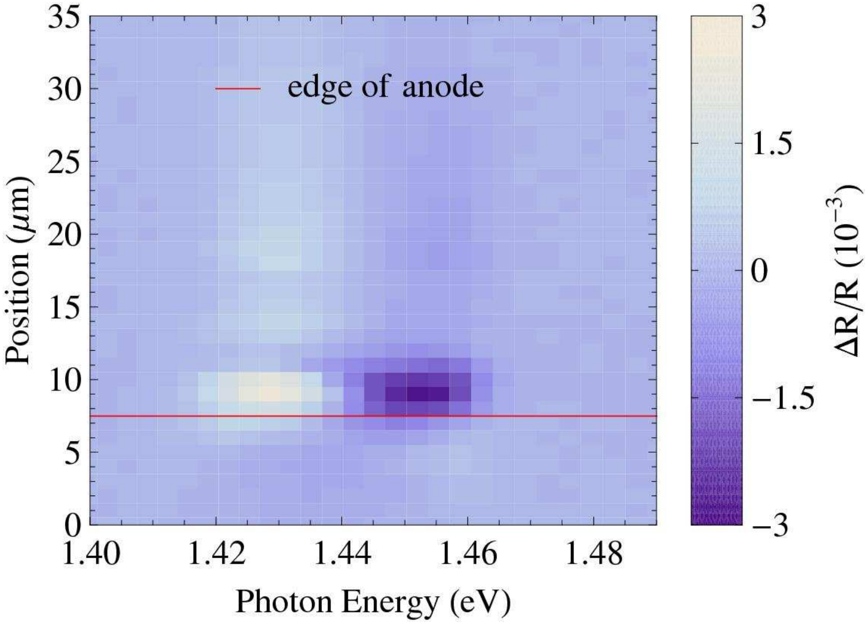

Figure 4.10: Two-dimensional plot of the ER spectrum of LT-GaAs sample with 250 V DC bias vs. laser spot position. The average excitation power is 15 mW. The red line shows the approximate position of the anode edge.

By modulating the bias field, a change in reflectance spectrum is detected that on first glance looks similar to the Franz-Keldysh oscillation. By moving the sample under the focal spot, in Figure 4.10, spatial map of the ER signal shows strong enhancement near the anode edge due to the trap-enhanced electric field, as expected for this sample structure with electrodes in direct contact to GaAs. However, in order to get strong THz emission, a high optical power of 15 mW is applied onto the sample. Under this strong illumination the field modulated reflectance signal, which shows a very strong and unusual dependence on both optical power and bias field, is not consistent with the Franz-Keldysh lineshape in reflectance, as discussed in the previous chapter. Figure 4.11 (a) and (b) show the ER signal under 150 V and 200 V bias. The red curves in both (a) and (b) are the ER signal with 15 mW incident optical power.

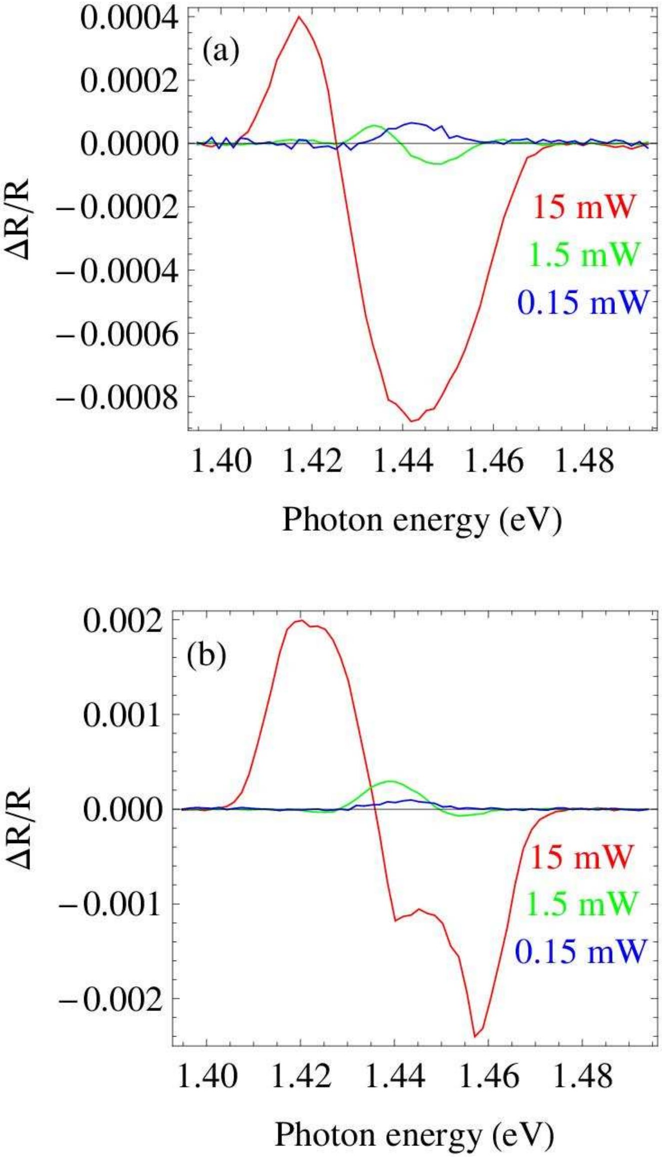

Figure 4.11: Electroreflectance signal from LT-GaAs. (a) Under 150 V bias. (b) Under 200 V bias.

The green curves correspond to 1.5 mW and the blue curves correspond to 0.15 mW incident optical power. All the ER signals are normalized by the voltage from the photodiode to provide ΔR/R. Whereas at low excitation, the Franz-Keldysh lineshape was observed in ER in the experiments described in the previous chapter, the data in Fig. 4.11 is clearly inconsistent with the Franz-Keldysh theory. The unexpected signal might be related to the field modulation of the photoinjected carrier density, which is much higher in the case of strong illumination. Also, with a high photocarrier concentration, a strong carrier screening effect must also be involved, and this makes the results more difficult to understand.

By adjusting the time delay of the probe pulse, the THz electric field generated from the LT-GaAs photoconductive antenna can be mapped out by the EO sampling system. In Figure 4.12 the THz electric field is plotted as a function of probe time delay. The bias applied across the gap between electrodes is 225 V.

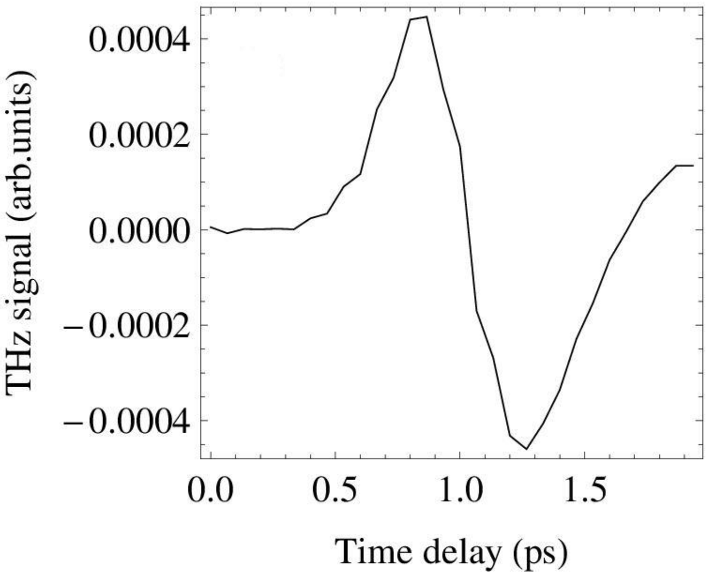

Figure 4.12: THz electric field measured using a LT-GaAs emitter under DC bias.

The spatial dependence of the THz peak field on the excitation spot position is also studied by moving the laser spot cross the gap between electrodes. As we expected, the THz field is also strongly enhanced near the edge of the anode due to the trap-enhanced electric field. The peak THz field can be found at the same position where we find the largest ER signal. The spatial dependence of the peak THz field and the peak absolute value of the ER signal is shown in Figure 4.13. Illuminating near the edge of the anode gives rise to a THz radiation about 30 to 50 times stronger than illuminating the center of the gap between electrodes.

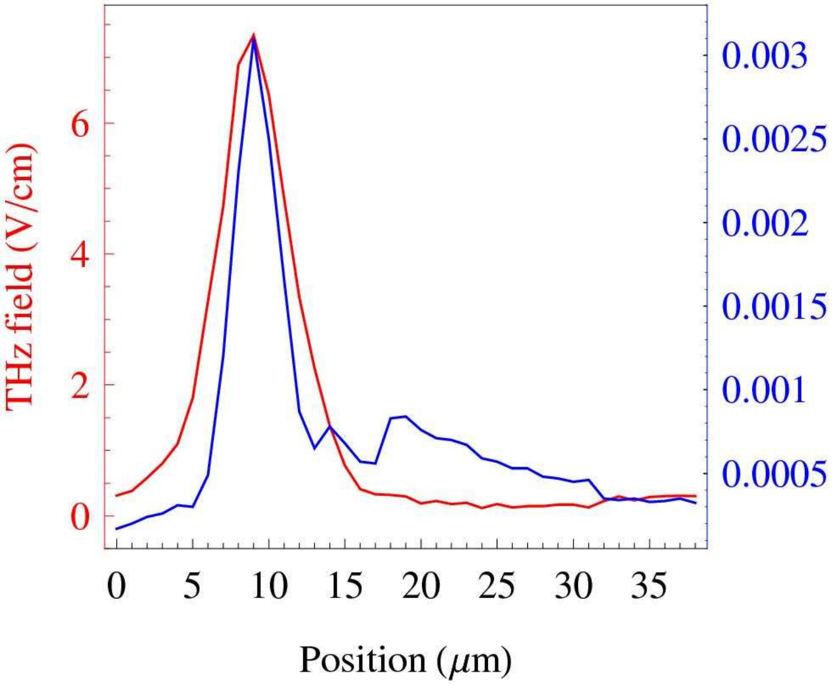

Figure 4.13: THz electric field (red) and ER signal (blue) versus laser spot position.

Under a maximum bias of 250 V, a peak THz field of 7.34 V/cm is measured. The field strength we found is a reasonable value compared with previous results [58], considering that the focus is tight on the sample and we did not use a silicon hemisphere lens to capture the highly divergent THz radiation. In Figure 4.14, the measured THz field is plotted as a function of the amplitude of the applied bias. The THz field shows a roughly linear dependence on the bias. However, for the THz emitter with electrodes in direct contact to the LT-GaAs, increasing the bias beyond 300 V will result in sparking from one electrode to the other, causing irreversible damage.

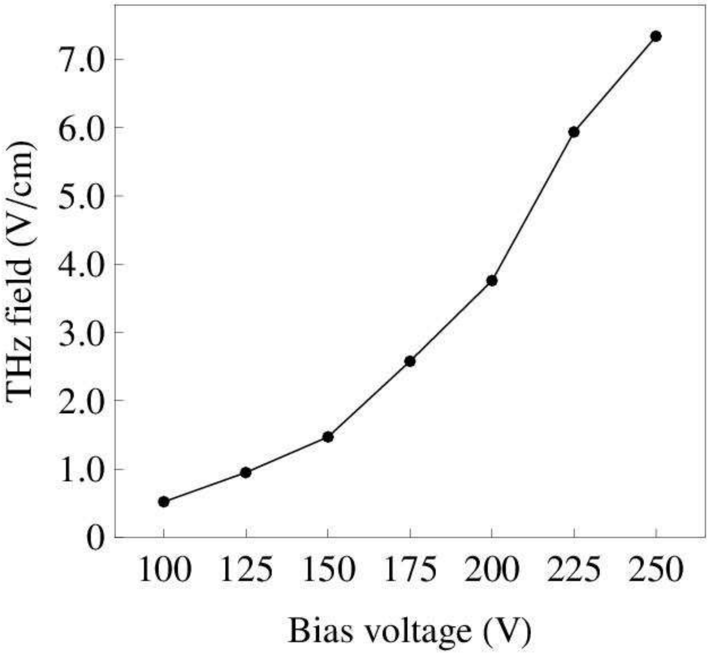

Figure 4.14: THz field as a function of the applied DC bias for an LT-GaAs based emitter.

4.6 Summary

In summary, we have developed a new technique for generating THz radiation effectively through a photoconductive THz emitter. The emitter with its gold electrodes insulated from the GaAs surface is biased using a rapidly oscillating bias near the laser repetition rate. Its chief advantage over photoconductive switches utilizing trap-enhanced fields is in spreading the electric field over a wider area. This provides improvement of the optical power saturation because of the larger excitation area. Our technique also does not require a specially patterned sample, like interdigitated structures; though using electrodes patterned on the surface with a thin insulating layer between is optimal. The RF signal is amplified by a passive LC circuit to produce the high voltage; it does not require active high voltage electronics, which often produce electrical pickup. One can also modulate the bias field at the repetition rate, leading to an effectively constant train of THz pulses—we have tested that scheme using a mechanical chopper to modulate the pump beam (we set the phase of the bias waveform to optimize the THz emission).

This technique can be an attractive alternative for generation of THz radiation using unamplified mode-locked laser. Currently we are limited to bias fields of roughly 30 kV/cm at radio frequencies, but the field can be increased further by optimizing the *LC* resonant circuit or using a more powerful RF amplifier. Other improvement like using an antireflection coating as the insulating layer to minimize the reflection loss can also help increasing the optical power-to THz conversion efficiency.

We also studied the electroreflectance and THz generation simultaneously from a DC-biased LT-GaAs sample with Au electrodes patterned directly on top. The existence of an enhanced electric field near the positively biased electrode is observed from the spatial dependence of both THz radiation and the ER signal. The ER signal is not consistent with the lineshape expected for the Franz-Keldysh effect when an optical power is used that is sufficient to generate significant THz radiation. A peak THz electric field of 7.34 V/cm from this LT-GaAs emitter is detected near the edge of anode, where we also find the strongest ER signal.

CHAPTER 5

Quantum interference and electric field induced coherent control

In this chapter, experiments on quantum interference control (QUIC) via one- and two- photon absorption pathways and coherent control of the carrier population injection rate in a semiconductor are discussed in detail.

First we start with a brief introduction about quantum interference injection of ballistic current and carrier population control in GaAs, and then follow with a description of a theory that predicts that an electric field enables coherent control of the carrier population. Then, in the experimental part, two measurements of the field induced coherent control will be discussed. An all-optical measurement and results are presented first. The results include the bias and optical polarization dependence of the carrier population in a GaAs epilayer. Then an electrical measurement scheme, in which we detect the change in the photocurrent read out by the same electrodes used to apply the bias to the sample, is discussed. The last part describes our measurement of ballistic current injection (without an applied field) via QUIC in erbium doped GaAs.

5.1 Quantum interference control of ballistic current in a semiconductor

When a semiconductor is illuminated with coherent optical beams at frequency ω (leads to two-photon absorption if $\hbar\omega$ is less than the band gap) and 2ω (leads to one-photon absorption), quantum interference between different absorption pathways that connect the same initial and final states can cause effects that depend on the relative phase between the frequency components, enabling control over the end state of the absorption process. This is analogous to the interference of two beams in a Young's double slit experiment. This quantum interference in semiconductors leads to the injection of a ballistic charge current [25,26,27] or pure spin current [31], where the current direction is controlled by the polarization of the light and the relative phase between the light components at frequency ω and 2 ω. By measuring the current injected in a semiconductor device, it has been shown that the phase evolution of the pulse train from a mode-locked laser can be measured [32,33]. The signal can be used to lock the laser's carrier-envelope offset frequency [34,35], an important function for optical frequency metrology using mode-locked lasers.

For one-color excitation in an unbiased semiconductor, either one-photon absorption of the 2 ω field or two-photon absorption of the ω field can generate a net carrier density, but neither can generate a net charge current without taking advantage of some material asymmetry. On the other hand, for excitation with the two frequencies simultaneously, the two types of quantum mechanical pathways that connect the valence band and conduction band are both present, and quantum interference between these two pathways leads to phase-dependent charge distributions that are asymmetric in k-space. Since the momentum is proportional to k, an asymmetric charge distribution is equivalent to a net current. As a result, the ballistic charge current which comes from the asymmetric distribution can be controlled coherently.

Let us examine quantum interference in absorption in a little more detail. When both ω and 2 ω fields excite a semiconductor and satisfy $\hbar\omega < E_g < \hbar 2\omega$, the total carrier injection rate can be written as the sum of three terms [36]:

$$\dot{n} = \dot{n}_{2\omega} + \dot{n}_{\omega} + \dot{n}_I , \tag{5.1}$$

where the first two terms correspond to the population injection rates for one- and two-photon absorption acting alone, respectively. The last term is the quantum interference part of the population injection rate. Each of these total carrier injection rates is a sum over the Brillouin zone of the rate for a particular wavevector *k*, for the interference term:

$$\dot{n}_I = \sum_{\vec{k}} \dot{n}_I(k) \propto \sum_{c,v,\vec{k}} a_{cv}^{2\omega}(\vec{k})^* a_{cv}^{\omega}(\vec{k}) + c.c = 0 . \tag{5.2}$$

Here $a_{cv}^{2\omega}$ and a_{cv}^{ω} are the one-photon and two-photon transition amplitudes. It can be shown that, for a simplified model of the bands in an isotropic semiconductor, $a_{cv}^{2\omega}$ is independent of *k* and a_{cv}^{ω} is proportional to $|\mathrm{k}|$. One has

$$a_{cv}^{2\omega}(\vec{k})^* a_{cv}^{\omega}(\vec{k}) \propto k|E_{2\omega}||E_{\omega}|^2 e^{i(2\phi_\omega - \phi_{2\omega})} , \tag{5.3}$$

which is antisymmetric in *k*-space. As a result,

$$\dot{n}_I(k) \propto k|E_{2\omega}||E_{\omega}|^2 e^{i(2\phi_\omega - \phi_{2\omega})} + c.c. \tag{5.4}$$

is antisymmetric in *k*-space [26,28]. Therefore, QUIC allows for the optical injection of a total carrier population $\dot{n}_I(k)$ that is distributed asymmetrically in *k*-space, as shown in Figure 5.1. The asymmetry results from constructive interference in one direction (determined by the optical polarization) in *k*-space, and destructive interference in the opposite direction. This leads to more carrier injection in one direction than the other, i.e., more in +*k* than in –*k* here in Figure 5.1.

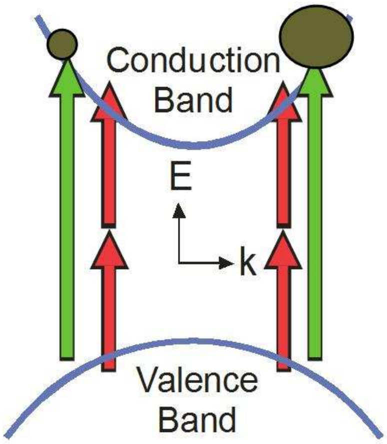

Figure 5.1. Schematic of asymmetric carrier distribution in *k*-space under two-color excitation.

Charge current in the semiconductor can be defined as a weighted average of the carrier population as a function of *k*. While the interference term sums to zero for the carrier injection rate, the asymmetric distribution of carriers in *k*-space results in a ballistic current:

$$\dot{J} \propto \sum_{c,v,\vec{k}} q\vec{v}(\vec{k}) \cdot \left| a_{cv}^{2\omega}(\vec{k}) + a_{cv}^{\omega}(\vec{k}) \right|^2 , \tag{5.5}$$

where $\vec{v}(\vec{k})$ is the velocity of carriers in *k*-space. The net one- and two-photon charge currents are zero, thus the total charge current is proportional to the interference term only:

$$\dot{\vec{J}} \propto \sum_{c,v,\vec{k}} q\vec{v}(\vec{k}) \cdot a_{cv}^{2\omega}(\vec{k})^{*} a_{cv}^{\omega}(\vec{k}) + c.c.. \tag{5.6}$$

Using symmetry arguments for an isotropic material and a parabolic band model, an equation for the ballistic charge current injection rate has been derived [67]:

$$\dot{J} = -iD\frac{q}{\hbar}[B_1\vec{E}_{\omega}(\vec{E}_{\omega} \cdot \vec{E}_{2\omega}^{*}) + B_2\vec{E}_{2\omega}^{*}(\vec{E}_{\omega} \cdot \vec{E}_{\omega}^{*})] + c.c., \tag{5.7}$$

where $\vec{E}_{\omega}$ and $\vec{E}_{2\omega}$ are the electric fields of ω and 2ω beam. The constant D is defined as

$$D = \frac{\sqrt{2}}{60\pi}\frac{q^3 E_P}{\sqrt{m}}\frac{(2\hbar\omega - E_g)^{3/2}}{\hbar^4\omega^4}, \tag{5.8}$$

where E_P is the Kane energy, E_g is the bandgap energy, q is the electron charge, and m is the electron mass. The coefficients B_1 and B_2 depend on material parameters (i.e., E_p and E_g) and the effective mass of the various band involved,

$$B_1 = 3.2 - 0.3\varepsilon, \tag{5.9}$$

$$B_2 = 0.036 + 0.19\varepsilon, \tag{5.10}$$

where the energy dependence term

$$\varepsilon = \frac{2\hbar\omega - E_g}{\hbar\omega}. \tag{5.11}$$

In case of QUIC when $\hbar\omega < E_g < \hbar 2\omega$, ε lies in the range $0 < \varepsilon < 1$. For bulk GaAs at room temperature with $\hbar\omega = 0.8$ eV and $E_g = 1.42$ eV, $\varepsilon = 0.225$ and $B_1 = 3.13$, $B_2 = 0.079$ can be found. Assuming two pulses with frequency ω and 2ω propagating in the z-direction with parallel linear polarizations along x-direction, the electric fields of incident beams are

$$\vec{E}_{\omega} = \left|E_{\omega}\right| \cdot e^{i\phi_{\omega}} \hat{x} \tag{5.12}$$

and

$$\vec{E}_{2\omega} = \left|E_{2\omega}\right| \cdot e^{i\phi_{2\omega}} \hat{x} \, . \tag{5.13}$$

Puting Eq. (5.12) and Eq. (5.13) into Eq. (5.7), the ballistic charge current is

$$\dot{J} = 2DB_1 \frac{q}{\hbar} \left|E_{\omega}\right|^2 \left|E_{2\omega}\right| \sin(2\phi_{\omega} - \phi_{2\omega}) \hat{x} \, . \tag{5.14}$$

As a result, for parallel linear polarizations of the incident beams, a charge current will be injected along the direction of the incident polarizations. By adjusting the relative phase of the ω and 2ω beams, the magnitude and sign of the current can be controlled. This effect has been observed previously both electrically [27] and by measuring the emitted THz radiation [84]. In the last section of this chapter, our measurement of current injection in Er-doped GaAs will be described.

5.2 QUIC population control in noncentrosymmetric medium

In the previous section, ballistic current generation through quantum interference in an unbiased semiconductor was discussed. In a (100)-oriented zincblende semiconductor (such as GaAs, the subject of all the experiments in this thesis) with two-color excitation, the photo-injected carrier-distribution in *k*-space is modulated and controlled by QUIC, but without changing the overall carrier density. For other crystal orientations, such as (111)- and (110)-oriented GaAs , the overall carrier density can also be controlled coherently by QUIC. This process may be observed when the optical fields are aligned along certain crystal axes.

In a medium that lacks inversion symmetry in *k*-space, e.g. (111)-oriented GaAs, Eq. (5.2), the approximations for the transition amplitudes made earlier break down. Roughly, the amplitude for one photon absorption has a slight linear dependence on k, and thus the sum over *k* of $\dot{n}_I(k)$, is not zero. The interference component of the total carrier population is [68]:

$$\dot{n}_I = \sum_{k} \dot{n}_I(k) = \sum_{jkl} \eta_I^{jkl} E_{\omega}^{j*} E_{\omega}^{k*} E_{2\omega}^{l} + c.c. \tag{5.15}$$

where the tensor η_I is related to the imaginary part of the second order susceptibility $\chi^{(2)}$ [36]. For the general case of ω and 2ω beam both linearly polarized, using $\vec{E}_\omega = |E_\omega| \cdot e^{i\phi_\omega}$ and likewise for the 2ω component, Eq. (5.15) reduces to:

$$\dot{n}_I = \eta_I^{jkl}(\omega) E_{2\omega}^{j} E_{\omega}^{k} E_{\omega}^{l} \cdot \exp(i\phi_{2\omega} - 2i\phi_{\omega}) + c.c.. \tag{5.16}$$

From Eq. (5.16), the interference part of the total carrier population $\dot{n}_I$ depends on the parameter $\phi_{2\omega} - 2\phi_\omega$ involving the relative phases of the two fields. In a crystal with center of inversion symmetry, in the absence of an external field, $\eta_I^{jkl}(\omega)=0$. If there is no center of inversion symmetry, then in general $\eta_I^{jkl}(\omega)\neq 0$ for $\hbar 2\omega$ above the bandgap, and coherent control of population is possible even in the absence of an external field [36]. We refer to this as the $\chi^{(2)}$-enabled population control process because it is enabled by the second-order nonlinear susceptibility. It has been experimentally observed in a (111)-oriented GaAs sample using optical [36] and electrical [69] detection.

5.3 Electric field induced population control

The $\chi^{(2)}$ nonlinearity in general is only nonzero for certain optical polarizations, but when a DC electric field is applied, one can get an effective $\chi^{(2)}$ that enables coherent control of carrier injection without aligning the optical fields along certain crystal directions. Just as in the case of electric-field induced second harmonic generation [70], when a DC electric field is applied to a GaAs sample, it can combine with the always present third-order susceptibility $\chi^{(3)}$ to produce an effective $\chi^{(2)}$. This effect enables control of the carrier population through quantum interference between one- and two-photon absorption, even in a crystal with a center of inversion symmetry [71].

By extending a theoretical framework for the one-photon Franz-Keldysh effect to multi-photon processes, Wahlstrand and Sipe calculated QUIC in the presence of a static electric field. In Eq. (5.18), the tensor $\eta_I^{jkl}(\omega)$, which describes the efficiency of the field-induced population control process as a function of ω, can be found analytically by assuming the valence band to conduction band velocity matrix element V_{cv} is k-independent and assuming parabolic bands separated by a direct bandgap $\hbar\omega_g$ [71]:

$$\eta_I^{zzz}(\omega) = \frac{e^3 E_{dc}^2}{2\hbar^3 \omega^4 \Omega} \left|V_{cv}^z\right|^2 \left(\frac{Ai^2\left(-\frac{2\omega-\omega_g}{\Omega}\right)}{2\Omega} + \frac{-\frac{2\omega-\omega_g}{\Omega} Ai^2\left(-\frac{2\omega-\omega_g}{\Omega}\right) - \left[Ai'\left(-\frac{2\omega-\omega_g}{\Omega}\right)\right]^2}{\omega} \right). \tag{5.17}$$

In Eq. (5.17), E_{dc} is the applied DC electric field, $\Omega = \left(e^2 E_{dc}^2 / 2\mu\hbar\right)^{1/3}$ is the electro-optic frequency, μ is the reduced mass, and $Ai(x)$ is the Airy function.

The spectrum of the field-induced population injection tensor shows Franz-Keldysh oscillations for $2\omega > \omega_g$. The oscillations are expected to be strongly damped at room temperature, just like the case of the one-photon Franz-Keldysh effect [47]. Eq. (5.17) can thus be simplified by using the asymptotic form of the Airy function, which gives the spectrum in terms of $\sin^2(x)$ and $\cos^2(x)$, and replacing them with the average value of 0.5,

$$\eta_I^{zzz}(\omega) = \frac{\sqrt{2} e^4 \mu^{1/2}}{2\pi\hbar^{9/2}\omega^4} \left|V_{cv}^z\right|^2 \left(\frac{1}{4\sqrt{2\omega-\omega_g}} - \frac{\sqrt{2\omega-\omega_g}}{\omega} \right) E_{dc}, \tag{5.18}$$

for $2\omega > \omega_g$. The tensor $\eta_I(\omega)$ is a real number and the population injection rate through quantum interference is thus directly proportional to $\cos(\phi_{2\omega} - 2\phi_\omega)$, where $\phi_{2\omega} - 2\phi_\omega$ is the relative phase between ω and 2ω beams. In this limit of strong damping, using expressions for the one- and two-photon absorption under the parabolic band approximation, the fractional change in carrier injection rate caused by quantum interference can be found as

$$\frac{\dot{n}_I}{\dot{n}} = \frac{6e^2 E_{dc} E_\omega^2 E_{2\omega} \omega(4\omega_g - 7\omega)}{16e^2 E_\omega^4 (2\omega-\omega_g)^2 + 3E_{2\omega}^2 \mu\hbar\omega^4 (2\omega-\omega_g)}, \tag{5.19}$$

for $2\omega > \omega_g$. As a result, in the large-broadening limit, the QUIC induced carrier injection rate is linear in the applied electric field E_{dc}.

5.4 Experimental layout – all optical measurement

In order to observe field-induced population control experimentally, we performed an all-optical measurement on (100)-oriented GaAs samples at room temperature. A diagram of the experimental apparatus is shown in Figure 5.2. The technique is similar to what was used by Fraser *et al.* to observe conventional population control in (111) GaAs [36]. The most important difference is the addition of a bias across the sample. A two-color pump pulse injects carriers through one- and two-photon absorption and quantum interference. Because the absorption coefficient of the GaAs is affected by the photoexcited carrier density, the transmission of a probe pulse is also sensitive to the density [72]. We look for a change in transmission that depends on the phase parameter $\phi_{21} = \phi_{2\omega} - 2\phi_{\omega}$. The light source for the pump beam is an optical parametric oscillator (OPO) using cesium titanyl arsenate (CTA), with a signal wavelength tuning range from 1400 nm to 1650 nm, and typical output power of 200 mW. The OPO is synchronously pumped by a mode-locked Ti:sapphire laser with 1.3 W output power at a repetition rate of f_{rep} = 76 MHz. The signal output of the OPO, centered at 1580 nm, is doubled using a barium borate (BBO) crystal, and the two harmonics are split by a prism into two paths, the relative delay of which can be adjusted using mirrors mounted on piezoelectric transducers. The harmonics are recombined using the same prism. We use the residual pump light, centered at 827 nm, as a probe beam. The pulse widths of the OPO fundamental, second harmonic, and probe pulses are approximately 160 fs, 220 fs, and 120 fs, respectively.

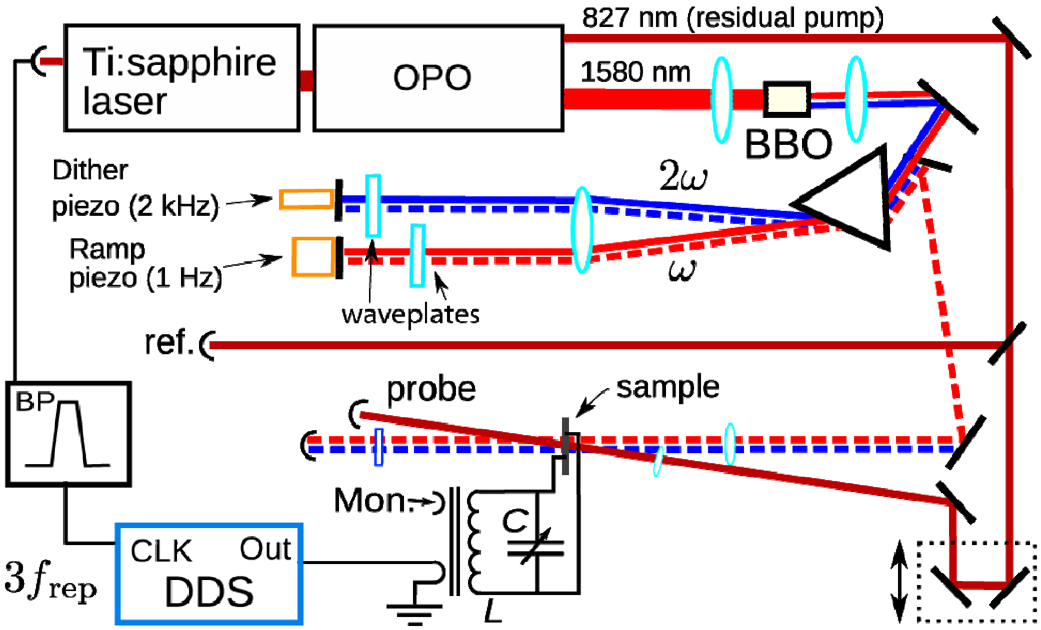

Figure 5.2. Schematic of the experimental apparatus, including the two-color interferometer and radio frequency biasing scheme. OPO: optical parametric oscillator, BBO: β-barium borate crystal, BP: bandpass filter, DDS: direct digital synthesizer.

The pump and probe beams are focused on a common spot between the electrodes. The ω beam average power is typically 160 mW and the 2ω beam average power is 6 mW. Part of the probe beam is split off before the sample and used as a reference for balanced detection. The balance detection helps us cancel the noise induced by fluctuations in the probe beam. The spot size of the pump beams is roughly 25 μm, and the spot size of the probe beam half that. It is important to have a smaller spot for the probe beam, in order to make sure it only detects the phase-sensitive carrier-injection from the two-color pump. To detect only the contribution from QUIC processes, we dither ϕ_{21} using a mirror mounted on a piezoelectric transducer. A lock-in amplifier referenced to the dither frequency measures only the changes in the probe transmission T due to changes in ϕ_{21}; the signal is proportional to $dT/d\phi_{21}$. This detection scheme works fine for our experiment, since we're interested in observing field-induced QUIC, instead of doing an absolute measurement. Using another mirror mounted on a piezoelectric transducer, we slowly ramp the phase parameter by more than 2π and average the data over approximately 100 ramp cycles.

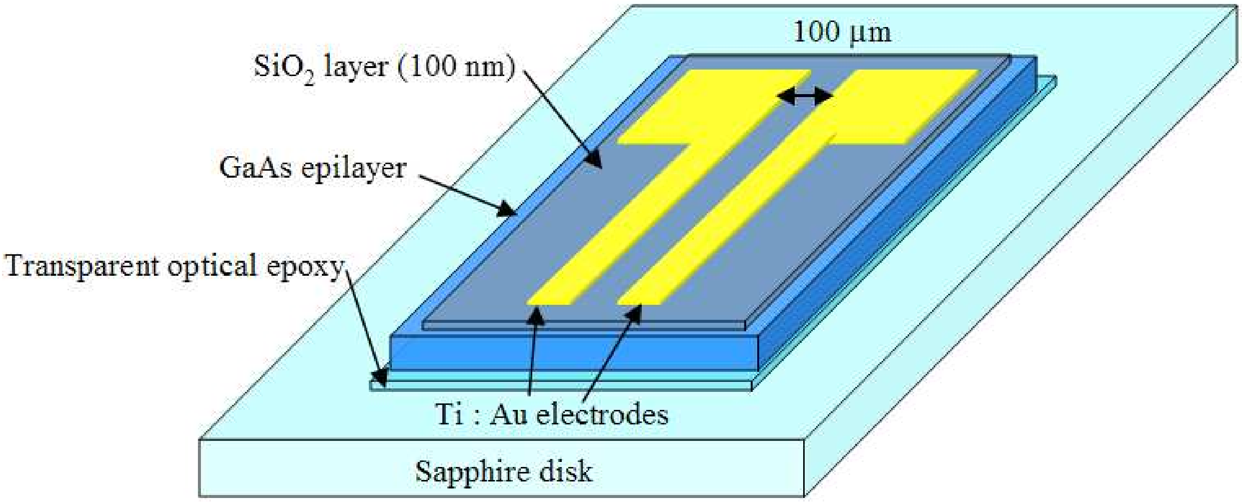

Figure 5.3. GaAs epilayer attached to a transparent sapphire disk by epoxy with insulated electrodes.

We use a 1 μm thick, undoped GaAs epilayer grown by molecular beam epitaxy. The GaAs sample is attached to the sapphire disk using transparent epoxy, and the substrate is then removed by chemical etching. A 100 nm thick insulating SiO_2 layer is deposited on the surface. More details about the thin sample can be found in Appendix C. Using photolithography, Au electrodes separated by 100 μm are then patterned onto the sample. A schematic plot of the GaAs sample structure is shown in Figure 5.3. To apply an effective dc electric field E_{dc}, we use a radio frequency (RF) bias synchronized to $f$rep. As mentioned numerous times previously, this technique results in an effectively uniform electric field in the plane of the sample [24] while avoiding highly nonuniform trap-enhanced fields [9]. We derive a harmonic of f_{rep} from a photodiode and use it as a clock for direct digital synthesis (DDS) of a synchronized, variable phase bias waveform at f_{rep}. A resonant LC circuit passively enhances the voltage across the electrodes. Detailed information about the RF bias system was given in Chapter 2. The phase of the waveform is optimized so that the peak of the waveform occurs when the optical pulse arrives at the sample. The sign of the field may be reversed by changing the phase of the RF signal by π using the DDS. Linear electroabsorption on the sample studied here, with analysis of the spectra as described in Chapter 3, at the same bias voltage and optical power, show that we achieve fields of approximately 20 kV/cm. Two samples were studied: one with the RF field pointing along a <001> crystal direction and the other with the field along <011>.

5.5 All-optical measurement results and discussion

The primary result of the all-optical measurement of electric field induced phase-dependent population control is shown in Figure 5.4. When there is no bias applied (blue dotted line), the transmitted probe power shows no modulation at the dither frequency as the phase parameter $\phi_{21} = \phi_{2\omega} - 2\phi_{\omega}$ is swept by the slow ramp piezo. Only when the uniform electrical field [24] generated by the RF bias is applied do we clearly observe the change in probe transmittance as a function of the phase parameter ϕ_{21}, with both positive (solid black line) and negative bias (dashed red line). Here the electric field $E_{\text{dc}} \parallel$ <001> crystal direction. For light at ω and 2ω normally incident on the (100) GaAs sample, for which population control enabled by the crystal symmetry is forbidden [36], we observe modulation of the transmitted probe beam *only* when the external bias is applied.

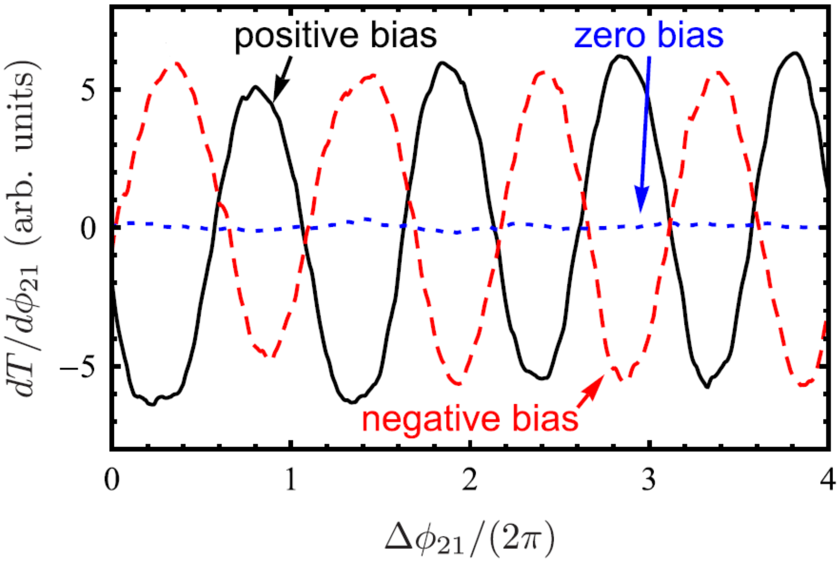

Figure 5.4. Modulation of the transmitted probe at the dither frequency as the phase parameter $\phi_{21} = \phi_{2\omega} - 2\phi_{\omega}$ is slowly swept. The signal for $E_{\mathrm{dc}} \parallel$ <001> is shown for positive (solid black), negative (dashed, red) and zero (blue, dotted) bias.

The signal scales as $P_{2\omega}^{1/2} P_{\omega}$ as predicted by the theory, where P_{ω} ($P_{2\omega}$) is the power of the ω (2ω) beam. The maximum observed modulation of the carrier density was 2%, which is within an order of magnitude of the theoretical prediction (the expected carrier density modulation from Eq. (5.21) is 0.6%). For a variety of reasons, it is nearly impossible to extract absolute efficiencies from the experiment. In an optically thin sample, the fractional change in the pump-probe transmission would equal the fractional change in the carrier density. Due to the fact that the thickness of our sample is comparable to the coherence length (~1.2 μm [37]) between the ω and 2ω beams, the amplitude of the modulation varies as a function of depth, complicating the analysis. Also, a cascaded process arising from electric field-induced second harmonic generation (EFISH) [70] followed by optical interference causes a change in the rate of carrier injection that depends on the relative phase ϕ_{21}. This is a two-step process in which second harmonic generation of ω generates a field at 2ω which then interferes optically with the light at 2ω. Like population control, this process leads to a change in the injected carrier density that depends on ϕ_{21}, and thus would produce an identical signal in the experiment. In this case, the second harmonic generation would be electric field-induced [70]. However, in a bulk semiconductor like the one studied here, there is ample reason to expect that the direct process previously described in terms of the multi-photon Franz-Keldysh effect [71] is dominant. In future experiments, it could be distinguished from the direct coherent control processes by using a layered structure [73]. Other complicating factors like multiple reflection and phase walkoff inside the sample make quantitative comparison of the experimental results and theoretical calculations challenging. Considering all these experimental issues and the simplified theoretical assumptions, the agreement between the theory calculation and the experimental data is reasonable. We have observed additional evidence of field induced QUIC in experiments on low-temperature grown GaAs and Er-doped GaAs that use electrical [27,69] rather than optical detection. Biasing the electrodes used to read out the injected photocurrent results in an enhancement in the signal that is inconsistent with current injection alone.

The magnitude of the bias can be controlled by adjusting the output amplitude of the DDS. The bias dependence results of the population control signal are shown in Figure 5.5, where the amplitude of the differential transmission signal is plotted as a function of the bias voltage for $E_{\mathrm{dc}} \parallel$ <001> (blue dots) and $E_{\mathrm{dc}} \parallel$ <011> (red squares). The lines are linear fits to the data points. The signal is consistent with the theoretical prediction in Eq. (5.20) of a linear dependence on bias, for both positive and negative bias (the latter is not shown).

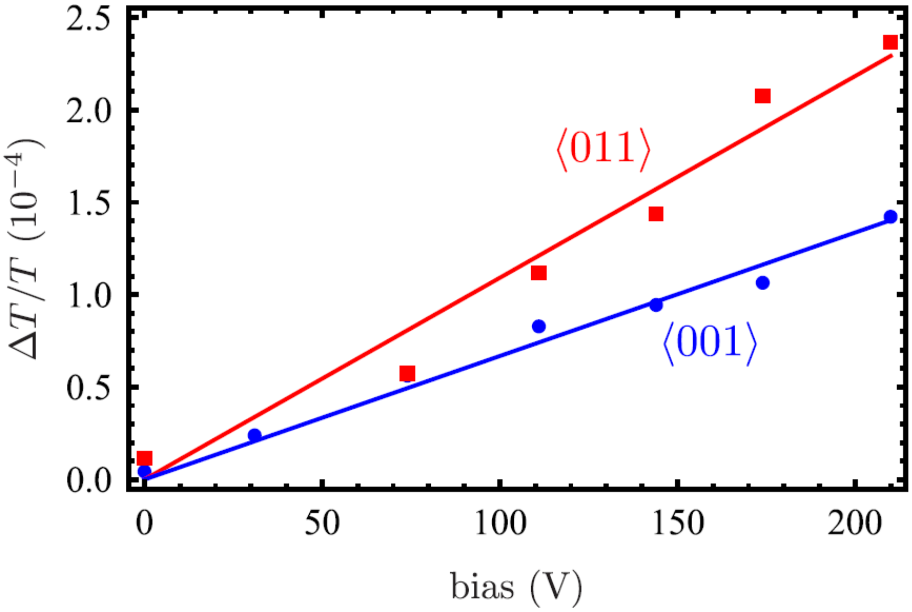

Figure 5.5. Amplitude of the signal as a function of bias voltage for $E_{dc} \parallel$ <001> and $E_{dc} \parallel$ <011>. The lines are linear fits.

Two quarter waveplates were used in the two-color interferometer as shown in Figure 5.2. By double passing the ω and 2ω beam through them, the quarter waveplates act as half waveplates here. By rotating these waveplates, the dependence of the population control signal on the polarization of the optical fields was also studied. Due to the polarization dependent reflection at the interfaces of the prisms in the interferometer, it is unfortunately not feasible to continuously adjust the polarization. Here we studied four different polarization configurations as shown in Figure 5.6, with the DC field along <110> crystal axis. The modulation of the probe transmittance is largest for all optical fields parallel to the applied electric field (blue). When the polarization of ω (green) or 2ω (red) or both of them (black) is rotated by ninety degree, the probe modulation signal falls by more than a factor of five.

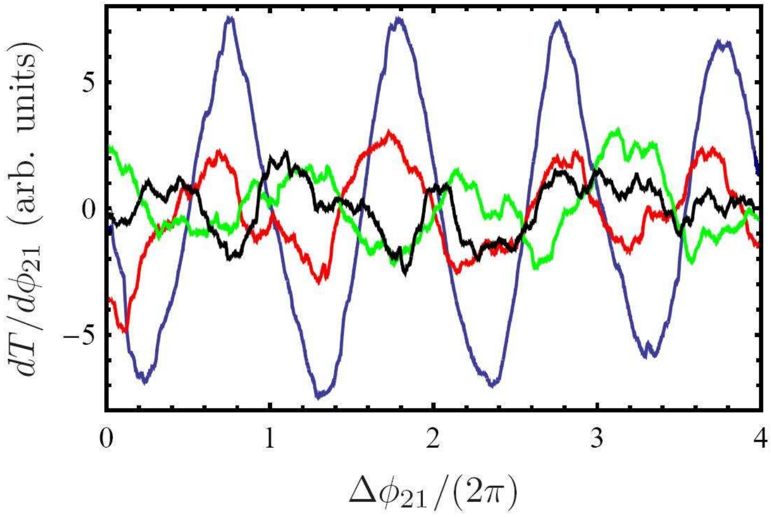

Figure 5.6. Polarization dependence of the signal for $E_{\mathrm{dc}} \parallel$ <110>: $E_{2\omega}$, $E_{\omega} \parallel E_{\mathrm{dc}}$ (blue); $E_{2\omega} \perp E_{\mathrm{dc}}$, $E_{\omega} \parallel E_{\mathrm{dc}}$ (red); $E_{\omega} \perp E_{\mathrm{dc}}$, $E_{2\omega} \parallel E_{\mathrm{dc}}$ (green); and $E_{2\omega}$, $E_{\omega} \perp E_{\mathrm{dc}}$ (black).

The results of the polarization dependence are consistent, within the noise, with the theoretical calculations using a 14-band $k \cdot p$ model [53,70], which predict that the signal should be smaller by a large factor for $E_{\omega} \perp E_{\mathrm{dc}}$ and zero when $E_{2\omega} \perp E_{\mathrm{dc}}$. The strong polarization dependence of field-induced population control is related to the contribution of intraband matrix elements to the two-photon absorption pathway, which leads to an enhanced efficiency when $E_{\omega} \parallel E_{\mathrm{dc}}$. This enhancement also plays a role in the polarization dependence of the two-photon Franz-Keldysh effect [85]. As in the one-photon FKE, the oscillation period depends weakly on the DC field direction because of band warping [74]. The $\chi^{(2)}$-enabled process is predicted to be affected weakly by the DC field, leading to oscillations in $\eta_I^{jkl}(\omega)$. In our experiment, polarization impurity causes a small component of the beam to be polarized parallel to the DC field, and we attribute the non-zero signal for $E_{2\omega} \perp E_{dc}$ seen in Figure 5.6 to that experimental imperfection, which is a particular problem for the 2ω beam because of the $P_{2\omega}^{1/2}$ dependence. The polarization dependence for the DC field along <100> (not shown) is noisier but essentially the same as the data for the DC field along <110> in Figure 5.6. We have also observed a DC field induced modulation of the transmitted 2ω beam that depends on the relative phase ϕ_{21}, which was observed in the analogous process enabled by $\chi^{(2)}$ [36].

5.6 All-electrical measurement of field-induced population control

In addition to the all-optical pump-probe detection, the modulation of carrier-density through QUIC can also be measured electrically, which is a more practical technique for applications. It has been proved that the two-color population control in a (111)-oriented GaAs can produce an easily measureable change in the photocurrent across a biased metal-semiconductor-metal structure [69]. Here we present the results of an electrical measurement for field-induced population control in a (100)-oriented low temperature grown GaAs (LT-GaAs), and compare the results with the all-optical detection.

In order to prevent the quick relaxation of the QUIC current due to a screening DC field created by separation of carriers, we use a LT-GaAs sample, which has a subpicosecond carrier lifetime and a high breakdown threshold [41]. Because of the short lifetime, the carriers get “frozen” in space before the field can pull them back, resulting in a larger signal in QUIC current injection experiments [28]. A pair of Au electrodes is patterned on the surface of the LT-GaAs sample, providing a series of gaps between the electrodes from 6 μm up to 150 μm, as shown in Figure 5.7. In order to detect the change in the photocurrent read out from the electrodes, our Au electrodes are in direct contact with the LT-GaAs (the insulated electrodes sample could not be used for this experiment).

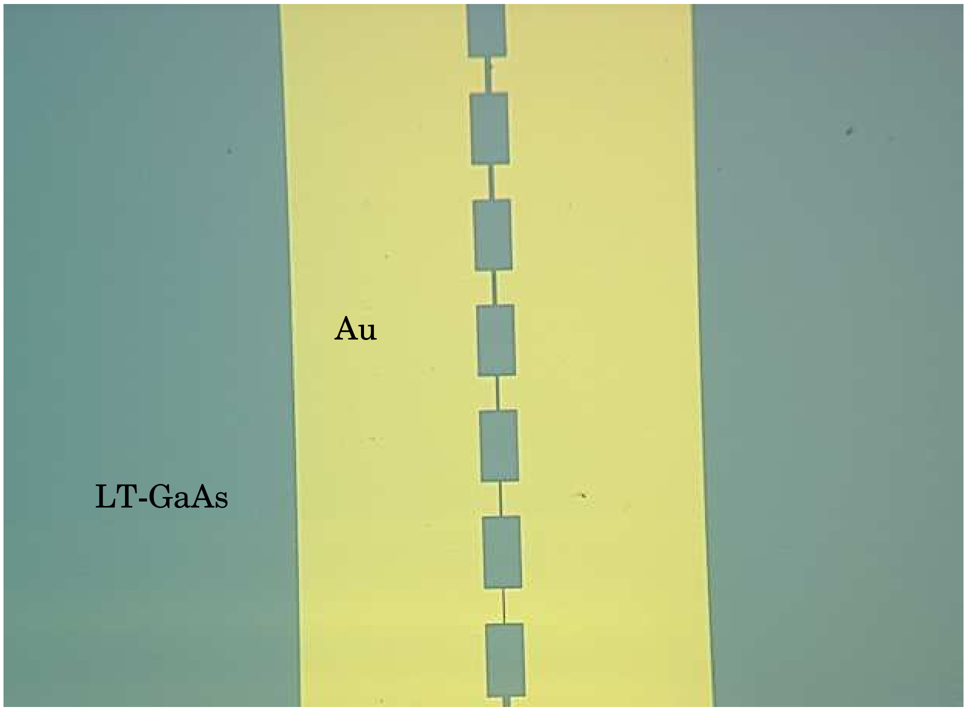

Figure 5.7. Electrode structure. Multiple gaps are shown; the electrode structure provides gaps ranging from 6 up to 150 μm.

We apply a DC bias across the electrodes and measure the photocurrent from the same electrodes as a function of the phase between the two-color excitation beams. Reading out the photocurrent using electrodes has been used previously in QUIC of ballistic current injection [27,28,33,75,76] and population control [69] experiments. In our case the signal is a combination of two processes: QUIC current injection [27], which ballistically injects a photocurrent that depends on $\phi_{21} = \phi_{2\omega} - 2\phi_{\omega}$, and field-induced modulation of the carrier injection rate [71], which modulates the carrier density and thus the photocurrent through the biased structure. The average current injected by QUIC in the absence of a field is < 500 pA. We use a circuit with separate transimpedence amplifiers for low frequency and high frequency components to detect the modulated photocurrent. This design keeps the DC bias across the sample constant while greatly amplifying signals at high frequencies. The gain of the DC transimpedence amplifier is 1 kΩ and the gain of the AC transimpedence amplifier is 1 MΩ, with a low frequency cutoff of 50 Hz.

A mode-locked Er-doped fiber laser produces 150 fs pulses at 1550 nm at a repetition rate of 26 MHz. The output is stretched using dispersion compensating fiber, amplified, and then compressed using a grating compressor. The average power at the output of the compressor is approximately 80 mW. The light is doubled and the harmonics split using a prism-based interferometer. The interferometer setup is very similar to the one shown in Figure 5.2. One major difference is that in the all-optical experiment, where a mirror mounted on a piezoelectric transducer is used to modulate ϕ_{21}, here an acousto-optic modulator (AOM) provides the phase modulation. Inside the interferometer, the 775 nm light (the 2ω beam) is frequency shifted using an AOM by $f_{\mathrm{AOM}} \approx 78$ MHz, and then recombined with the ω beam. The frequency shift of the 2 ω beam is equivalent to a linear phase ramp. The phase parameter ϕ_{21} is typically modulated at approximately 20 kHz. The amplified signal is measured using a lock-in amplifier referenced to $f_{\mathrm{det}} = 3f_{\mathrm{rep}} - f_{\mathrm{AOM}}$. The reference signal is generated using an RF phase detector.

The AOM technique has many advantages over implementations using a moving mirror to dither the phase. The phase modulation ramps constantly over 2π, and the modulation frequency can be varied over a wide range simply by varying f_{AOM}, with no complications arising from resonances in the piezoelectric transducer. The bandwidth limit caused by the capacitance of the electrode structure has been found to be one of the limiting factors in carrier-envelope phase detectors [77], and a two-pulse setup using an AOM could be used to optimize a carrier-envelope detection system with no need for a carrier-envelope phase stabilized source. Also, due to periodic tilting of the mirror on the piezoelectric transducer as it shakes, a DC offset has been encountered in previous experiments [78]; this artifact does not arise when an AOM is used to modulate the phase.

The recombined ω and 2ω beams are focused on the sample surface using a microscope objective. A glass slide is placed in the beam to sample some of the light that reflects from the sample, allowing imaging of the sample surface and precise placement of the laser spot. At the sample, the maximum power available is typically 30 mW at 1550 nm and 400 μW at 775 nm. In all of the data presented using electrical detection, the optical fields are linearly polarized along the DC field direction.

By adjusting the bias field applied on a 10 μm gap of the LT-GaAs sample between two electrodes and detecting the modulated photocurrent as a function of ϕ_{21}, a bias dependence of the QUIC signal (black) and the phase of the electrically detected signal (red dashed) were measured; both are shown in Figure 5.8. Unlike the linear bias dependence measured by the all-optical detection, shown in Figure 5.5, the bias dependence measured by the electrical detection is not monotonic. As the magnitude of the bias is increased from zero, the signal decreases to nearly zero first, then increases rapidly, for both positive and negative bias. The phase of the signal reverses at the same time that the signal dips to near zero. The signal is greatly enhanced at a bias of ±2 V. The maximum fractional modulation of the photocurrent by QUIC is 5×10^{-3}, about a quarter as large as the signal observed in the all-optical experiment [71], where an electric field of approximately 20 kV/cm was present. This is consistent with the electric field calculated from the voltage and electrode spacing of 10 μm.

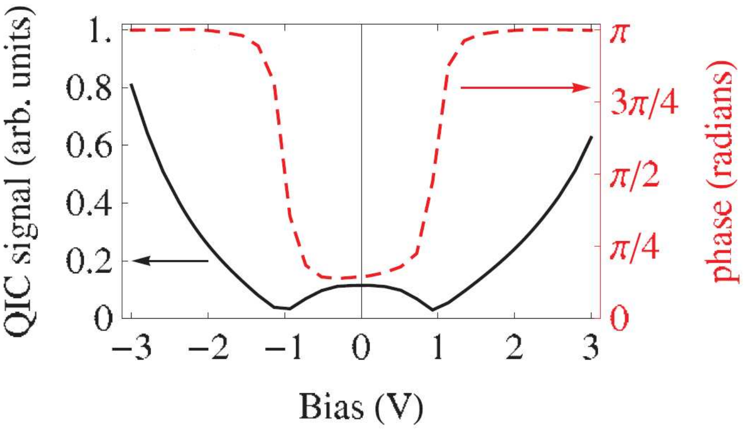

Figure 5.8. Bias dependence of field induced QUIC population control, measured by the electrical detection. Black line shows non-monotonic dependence of the signal magnitude. Dashed red line shows the phase of the signal which flips by nearly π when the magnitude dips near zero.

The photocurrent signal includes two components which are roughly π out of phase. One is a bias-independent signal, which mainly comes from ballistic current injection via QUIC [27]; the other one depends on the magnitude of the bias, which essentially comes from field-induced population control. Although the field-induced population control signal is supposed to be linear in the electric field and thus the bias, the direction of the photocurrent is the same sign as the bias, resulting in an even symmetry of the bias dependence. From Figure 5.8, the even symmetry of the bias-dependent photocurrent agrees with our interpretation in terms of field-induced population control.

In previous studies of either the $\chi^{(2)}$ enabled population control [69], or the quantum interference control of ballistic current injection [78], in case of no bias, the QUIC signal is enhanced when the laser beam is focused near an electrode edge. When a bias is applied, the field-induced QUIC signal also shows strong dependence on the laser spot position. Figure 5.9 shows the bias dependence for three different laser spot positions on a sample with 10 μm electrode spacing. This electrode spacing produces the optimal signal-to-noise ratio at zero bias. The spot size in this data is approximately 6 μm. When the laser spot is centered between the electrodes (the data in Figure 5.8 and the green curve in Figure 5.9), the bias dependence is symmetric. But when the laser spot is focused on one side (red curve) of the structure or the other (blue curve), the enhancement of the signal is greater for either positive or negative bias.

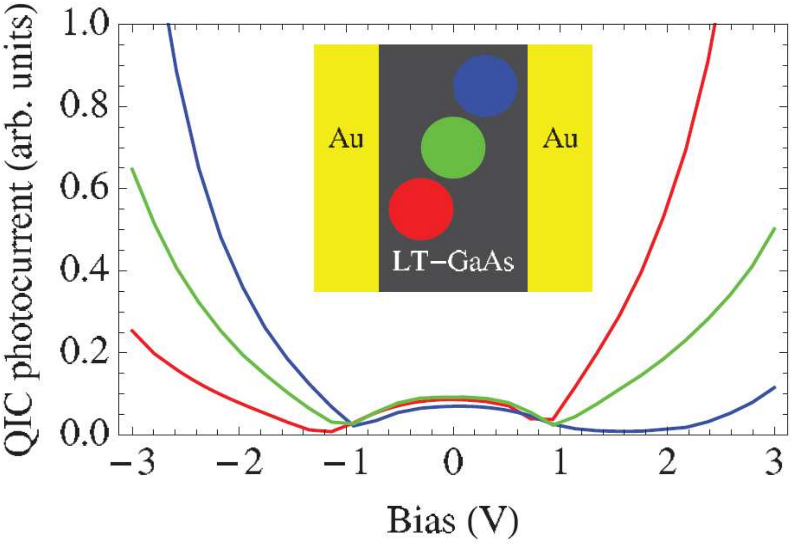

Figure 5.9. Bias dependence of field-induced QUIC signal on three different laser spot positions for 10 μm electrode spacing.

The connection between the bias and spatial dependence is somewhat clearer in a sample with wider spaced electrodes. Results are shown for a sample with electrodes spaced by 150 μm in Figure 5.10. The ϕ_{21}-dependent photocurrent is shown as a function of bias voltage and the position of the laser spot. Regardless of the bias, the signal is strongest when the laser spot, which in this case is approximately 12 μm wide, is focused near the electrode edges. Depending on which electrode the laser spot is near, we observe an enhancement of the signal for positive or negative bias. For a bias of the opposite sign, the signal magnitude is independent of bias.

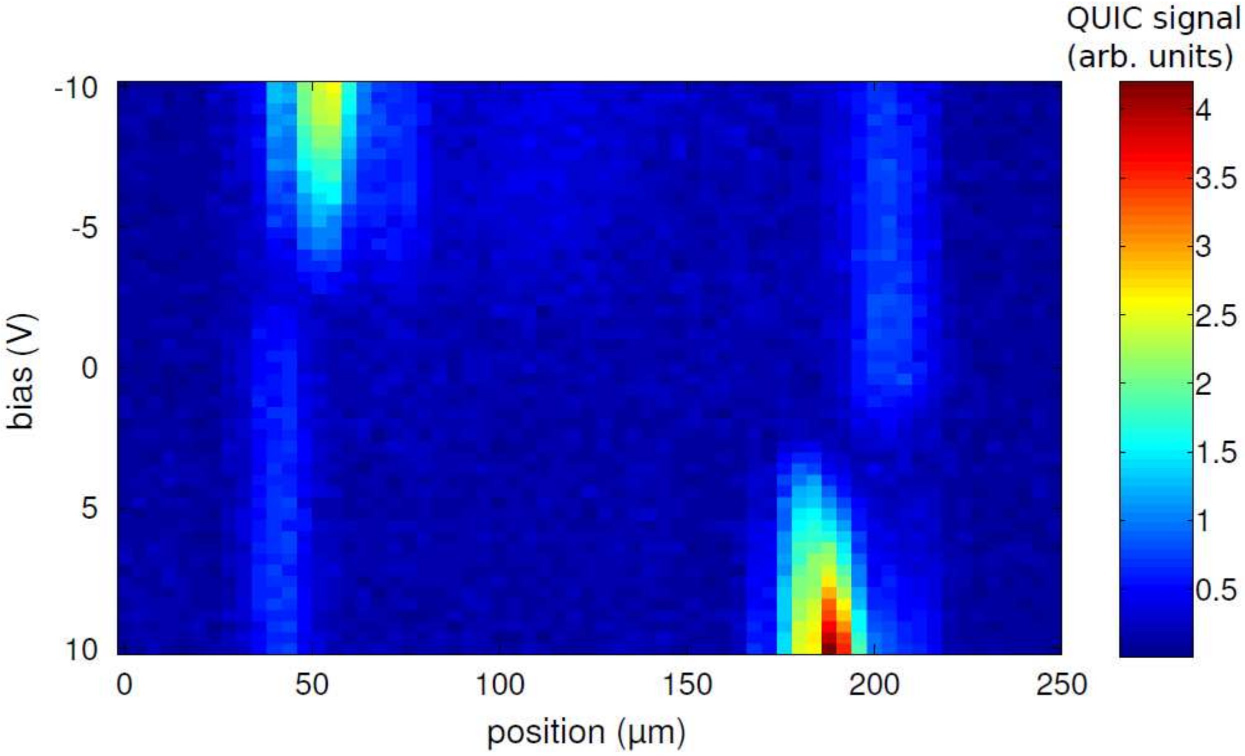

Figure 5.10. Map of the field-induced QUIC signal magnitude as a function of bias and the position of the laser spot for 150 μm electrode spacing. The edges of the electrodes are at 40 and 190 μm.

The bias dependence when the laser spot is positioned near an electrode is shown in Figure 5.11. Data for two laser spots are shown, separated by 12 μm. For the spot closer to the electrode (solid lines), a dip in the amplitude (black) is observed at -2.5 V, and as the bias is swept through that voltage, the phase (red) changes by approximately 0.63π. The data for the spot farther from the electrode (dashed lines) shows no discernible dip in the amplitude (black), and the phase (red) changes by approximately π/2. The data for the laser spot focused near the other electrode displays the same behavior, but at positive rather than negative bias. For a wide electrode spacing, the observed phase shift is closer to the value of π/2 predicted by the theory [79] if we identify the bias-independent signal as current injection and the rest as field-induced population control.

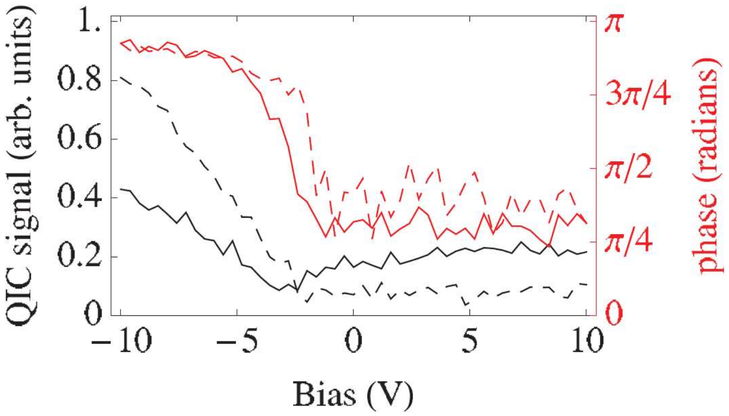

Figure 5.11. Bias dependence of QUIC signal in a sample with 150 μm electrode spacing, for two laser spots spaced by 12 μm: nearer the electrode (solid) and farther away (dashed). The amplitude (black) and phase (red) of the QUIC signal are shown.

We have observed the same general trends when using an OPO and tuning ℏω from 0.72 eV to 0.83 eV, showing that this effect is not localized to any particular photon energy. We have also observed the same bias dependence in an Er-doped GaAs sample [76]. With a widely spaced electrode structure and higher voltage, we have also observed field-induced QUIC in a semi-insulating (SI) GaAs sample. In SI-GaAs, no signal could be seen at zero bias. In all experiments, we observe the strongest signal near the electrode edges.

From the electrical measurement, the symmetric distribution of the photocurrent signal in bias dependence is consistent with a combination of ballistic current injection and field-induced population control. However, many questions remain about the interpretation of the data. The phase shift observed experimentally, which varies depending on the electrode spacing and the laser spot position, doesn't agree with the $\pi/2$ phase shift predicted by the theory of current injection and population control [79]. The enhancement of the photocurrent signal near the electrode edge could be partially explained by the enhancement of electric field near electrode edge due to a combination of the trap-enhanced field and the photo-Dember effect (separation of electrons and holes generates a transient electric field). A better model of the carrier dynamics in the metal-semiconductor-metal structure is required to fully explain the experimental results.

5.7 QUIC of photocurrent injection in Er-doped GaAs

Quantum interference control of ballistic current injection in bulk semiconductor has been used to measure and stabilize the phase evolution of the pulses from a mode-locked laser [33,34]. However, the relatively small signal-to-noise ratio limits the application of this technique. In order to gain a larger QUIC signal, a semiconductor with a short carrier lifetime is preferred, because the short lifetime prevents internal discharge of the charge built up by the QUIC current during the time between laser pulses [28]. The most commonly used material for QUIC of photocurrent is low-temperature grown GaAs (LT-GaAs), which has a subpicosecond carrier lifetime.

Gallium arsenide with erbium doping or embedded ErAs nanoparticles (GaAs:Er) is another material with an ultrashort carrier lifetime. Since it can be grown using molecular beam epitaxy (MBE) at standard temperatures, the GaAs:Er has the advantage of being able to be more easily incorporated in heterostructures, which is widely used in today's electronics industry. Also GaAs:Er is expected to have better crystal structures for the GaAs, and hence better usability. In this section, we compare the carrier lifetime and the size of the QUIC signal from three types of samples: an Er-doped GaAs (GaAs:Er), a LT-GaAs, and a semi-insulating GaAs (SI-GaAs), and show experimental results that prove the QUIC signal from a GaAs:Er is comparable to that in a LT-GaAs, and much stronger than that in a SI-GaAs.

The LT-GaAs and GaAs:Er samples were grown using MBE, by Dr. Richard Mirin at NIST Boulder. The LT-GaAs sample consists of a 1.8-μm layer of GaAs grown at 400 ^{o}C on a semi-insulating GaAs substrate with no buffer layer. The GaAs:Er sample consists of 6 μm of Er-doped GaAs grown on top of a 500-nm thick $Al_{0.8}Ga_{0.2}As$ layer on a GaAs substrate. The Er concentration is 6×10^{18} cm^{-3}, as measured by secondary ion mass spectroscopy (SIMS) on a reference sample. As the penetration depth of above-bandgap light in GaAs is on the order of 1 μm, the signal from each sample is essentially entirely due to the LT-grown or Er-doped region.

We performed a standard optical pump-probe experiment to measure the carrier lifetime of each sample. A mode-locked Ti:sapphire laser with 860 nm wavelength and a repetition rate of 76 MHz was used as our light source. The pulse width of the laser was about 150 fs. The average output power of the laser is around 1.3 W, we only use a small portion of it in order to prevent damage to the sample. Light from the laser was split into pump and probe beams using a beam splitter, with roughly 30 mW average power in each beam. The pump beam was chopped at 1.5 kHz by a mechanical chopper, and that frequency was used as the reference frequency of the lock-in amplifier. The reflected probe beam was detected with a photodiode, the pump and probe beams were cross polarized, and a polarizer was used before the detector to minimize the background from scattered pump light.

Time delay between the pump and probe beam is controlled by a retroreflector mounted on a translation stag driven by a stepper motor in the probe beam path. Changes in the reflected probe beam power were recorded as a function of time delay between pump and probe beam. Figure 5.12 shows the results of the pump-probe experiment for each sample.

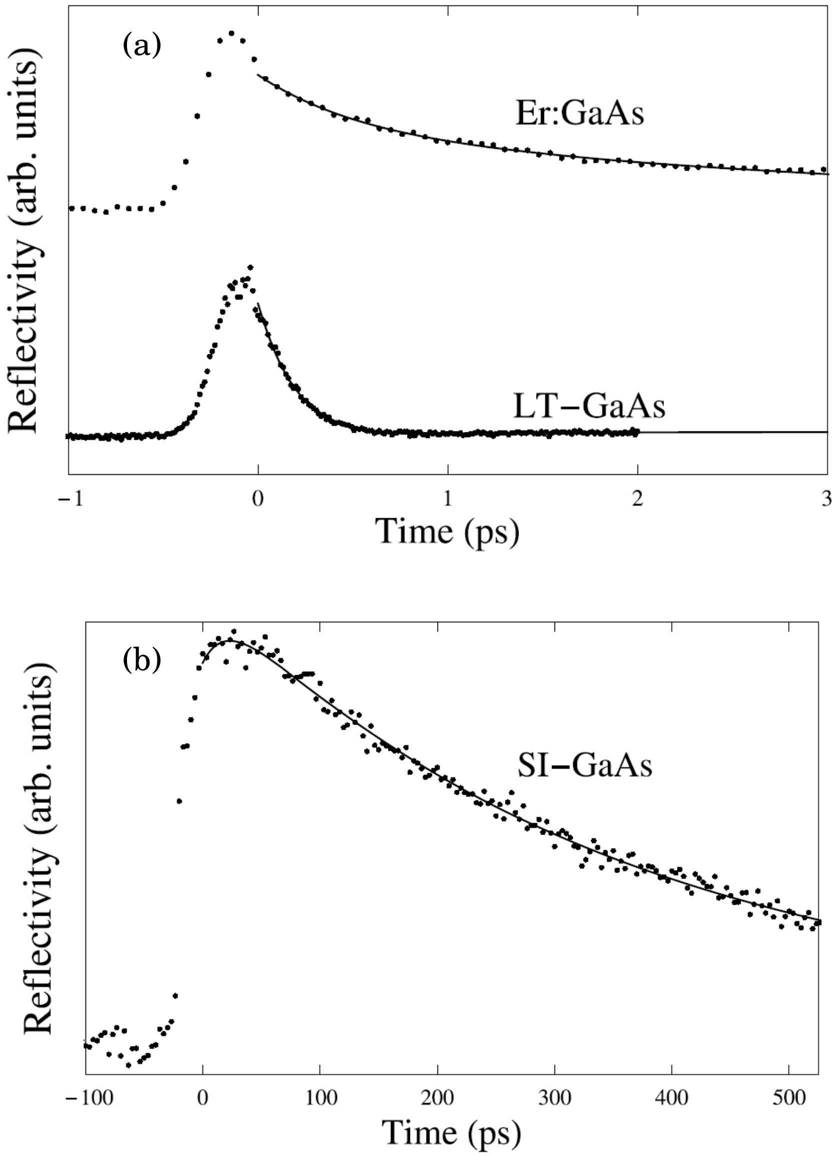

Figure 5.12. Pump-probe results. The points are the measured reflectivity as a function of time delay, and the solid lines are fits of the data (after the coherent

artifact when the pump and probe pulses overlap in time) to $A_1 \exp(-t/\tau_1) + A_2 \exp(-t/\tau_2) + B$. (a) Results for GaAs:Er and LT-GaAs. (b) Results for SI-GaAs.

In order to calculate the carrier lifetime, pump-probe data from the three samples are fit to an exponential decay model. The signal from LT-GaAs could be fit using a single exponential with a decay constant of 280 fs. The signal from the GaAs:Er sample required two exponentials for a good fit, with τ_1 = 500 fs and τ_2 = 4.5 ps. We ascribe the carrier lifetime as the longer of the two decay constants. The measured lifetimes in both LT-GaAs and GaAs:Er are much shorter than in SI-GaAs, which was measured to be 354 ps. These results are in reasonable agreement with previous studies of similar samples [80,81].

We patterned Au electrodes on the surface of the samples using standard photolithographic techniques. The electrode structure is similar to the one shown in Figure 5.7, which provides gaps between electrodes of various widths. The GaAs:Er sample had gaps from 2 μm to 6 μm, while the LT-GaAs sample had gaps from 8 μm to 26 μm. While ideally we would have had the same gap width to compare the results in GaAs:Er and LT-GaAs, the signal depends only weakly on the gap width between 6 μm and 8 μm, so we compare the signal from the 6 μm gap on the GaAs:Er sample to the signal from the 8 μm gap on the LT-GaAs sample.

QUIC current injection is measured using the prism interferometer setup which is similar to the one shown in Figure 5.2. Here we only use the interferometer part to modulate the phase ϕ_{21} and measure QUIC current electrically through a transimpedance amplifier as described in the third paragraph of section 5.6, without the requirement of a probe beam and external bias.

Sample	Lifetime	Gap width	QUIC signal
GaAs:Er	4.5 ps	6 μm	0.6 mV
LT-GaAs	280 fs	8 μm	1.6 mV
SI-GaAs	354 ps	30 μm	0.7 mV
LT-GaAs	280 fs	30 μm	347 mV

Table 5.1. Summary of data for the samples studied.

The quantum interference signal was optimized by moving the sample with respect to the focusing lens. This optimizes the focus and the position of the laser spot with respect to the electrodes. As observed in the previous experiment [78], the QUIC current is very sensitive to the position of the laser spot. We found the maximum QUIC signal when the laser spot is focused near electrode edge, this result consists with the previous study [78]. The peak-to-peak voltage of the QUIC signal from GaAs:Er with a 6 μm gap and from LT-GaAs with an 8 μm gap were recorded, we found that they were roughly comparable. As a control, we measured the signal from a semi-insulating GaAs sample with a 30 μm gap and found that the signal was 500 times smaller than from an equivalent LT-GaAs sample. The data is summarized in Table 5.1. The results prove that GaAs:Er is a suitable material with good signal-to-noise ratio for QUIC of ballistic current injection. The smaller signal from the GaAs:Er sample compared to the LT-GaAs sample is related to its slightly longer carrier lifetime, which can be shorten by heavier Er doping.

5.8 Summary

In this chapter, we discussed quantum interference control of ballistic currents carrier population in a semiconductor. We started with a brief introduction about the theory of both QUIC of ballistic current and coherent control of carrier population. Then our main experimental results were presented. First we showed the all-optical measurement of the electric field-induced population control in bulk GaAs. The linear bias dependence of the population control signal and the polarization dependent results show the largest signal when the optical fields are parallel to the applied electric field, consistent with theoretical predictions. We also presented the experimental scheme and results of the electrical measurement of field-induced population control. The phase shift and the spatial dependence of the electrically detected signal were discussed. In the last part we showed the experimental results of ballistic current injection via QUIC in an erbium doped GaAs sample, and compared the results with that from a low-temperature grown GaAs. This showed that Er-doped GaAs is suitable substitute for LT-GaAs for semiconductor-based carrier-envelope phase detection.

CHAPTER 6

Conclusion

This thesis contains a detailed description of our radio-frequency (RF) bias technique and the main results of three different projects related to the linear and nonlinear optical properties of gallium arsenide. The RF bias technique, presented in Chapter 2, is an essential method that helps us achieve a uniform electric field in a bulk GaAs sample with transverse electrode M-S-M structure. By combining a fast oscillating bias in the radio frequency range applied to electrodes insulated from the GaAs sample with a pulsed light source, a uniform electric field between the transverse electrodes can be produced. In addition to the RF bias system, a heterodyne detection technique that can guarantee a wide range of reference frequencies for lock-in detection with good signal-to-noise performance is also developed.

The first project, discussed in Chapter 3, presents experimental results of electroreflectance (ER) using both the conventional DC bias and the RF bias technique. Spatially resolved ER data proves that by using the RF bias combined with the insulated electrode GaAs sample, we successfully minimize the trap-enhanced electric field and obtain a uniform transverse electric field. Results of electroabsorption experiment from a thin GaAs epilayer with DC bias are also included in this chapter. Possible future work includes: 1. one could study the odd Franz-Keldysh effect, which appears for certain crystal orientation and optical field directions, using a transverse geometry; 2. one could go to low temperatures using the RF bias. The FK oscillations would be stronger; 3. study higher conductivity samples, for which the RF technique is the only way to get an ER signal.

The second project, presented in Chapter 4, involves THz generation from a photoconductive emitter. We adopt the RF bias system, which gives a uniform electric field distribution in the GaAs emitter, to generate THz radiation. The uniform field in the emitter allows use of a large excitation spot to minimize the ultrafast carrier screening. The emitted THz radiation is detected by an electro-optical sampling system, and compared with results from a DC biased emitter. The RF technique clearly shows improved optical power-to-THz conversion efficiency, and a great potential for further improvement. In addition, THz generation from a low-temperature grown GaAs photoconductive emitter with DC bias is also discussed. Possible future directions include: 1. increase the bias field by narrowing the electrodes or increasing the bias voltage, to see if the THz field can be further improved; 2. study the dynamic of the DC field in the semiconductor, understanding it might help optimize the technique.

The third project, discussed in Chapter 5, is focused on electric field-induced quantum interference control of photoexcited carrier population in bulk GaAs. We show theory predictions and experimental evidence that a constant electric field enables control of the photocarrier injection rate by interference of one- and two-photon absorption in GaAs. Results from an all-optical measurement and an electrical measurement scheme are presented. Furthermore, quantum interference control of ballistic current injection in an erbium-doped GaAs is discussed. Possible future work: 1. study the wavelength dependence of the field-induced QUIC and compare with the theory; 2. do more experiments to understand the spatial dependence of the QUIC signal using electrical detection.

Together, these results serve as useful tools for understanding electro-optic properties and physical processes such as carrier transport in semiconductor materials.

Bibliography

[1] W. Franz, "Einfluß eines elektrischen Feldes auf eine optische absorptionskante," Z. Naturforsch. A 13, pp. 484, 1958.

[2] L. V. Keldysh, "The effect of a strong electric field on the optical properties of insulating crystals," *Sov. Phys. JETP* 7, pp. 788, 1958.

[3] D. E. Aspnes, "Linearized Third-Derivative Spectroscopy with Depletion-Barrier Modulation," *Phys. Rev. Lett.*, vol. 28, no. 14, pp. 913, Apr. 1972.

[4] D. E. Aspnes and A. A. Studna, "Schottky-Barrier Electroreflectance: Application to GaAs," *Phys. Rev. B*, vol. 7, no. 10, pp. 4605, May 1973.

[5] S. F. Pond and P. Handler, "Flatband Electroreflectance of Gallium Arsenide. I. Experimental Results," *Phys. Rev. B*, vol. 6, no. 6, pp. 2248, 1972.

[6] M Cardona, *Modulation spectroscopy*, Academic Press, 1969

[7] V. Rehn and D. S. Kyser, "Transverse Electroreflectance," *Phys. Rev. Lett.*, vol. 18, no. 20, pp. 848, May 1967.

[8] J. K. Wahlstrand, J. A. Pipis, P. A. Roos, S. T. Cundiff, and R. P. Smith, "Electrical measurement of carrier population modulation by two-color coherent control," *Appl. Phys. Lett.*, vol. 89, no. 24, pp. 241115–3, Dec. 2006.

[9] S. E. Ralph and D. Grischkowsky, "Trap-enhanced electric fields in semi-insulators: The role of electrical and optical carrier injection," *Appl. Phys. Lett.*, vol. 59, no. 16, pp. 1972–1974, Oct. 1991.

[10] D. Grischkowsky, S. Keiding, M. van Exter, and C. Fattinger, "Far-infrared time-domain spectroscopy with terahertz beams of dielectrics and semiconductors" *J. Opt. Soc. Am. B*, vol. 7, no. 10, pp. 2006-2015, 1990.

[11] H. Harde, R. A. Cheville, and D. Grischkowsky, "Terahertz studies of collision-broadened rotational lines," *J. Phys. Chem.,* vol. 101, no. 20, pp. 3646-3660, 1997.

[12] D. M. Mittleman, R. H. Jacobsen, and M. C. Nuss, “T-ray imaging,” *IEEE J. Sel. Top. Quantum Electron.,* vol. 2, no. 3, pp. 679-692, 1996.

[13] S. Hunsche, M. Koch, I. Brener, and M. C. Nuss, “THz near-field imaging,” *Opt. Commun.,* vol. 150, no. 1-6, pp. 22-26. 1998.

[14] Q. Wu, T. D. Hewitt and X.-C. Zhang, “Two-dimensional electro-optic imaging of THz beams,” *Appl. Phys. Lett*., vol. 69, no. 8, pp. 1026-1028, 1996.

[15] R. A. Cheville, R. W. McGowan and D. R. Grischkowsky, “Late-time target response measured with terahertz impulse ranging,” *IEEE Trans. Antennas Propag*., vol. 45, no. 10, pp. 1518-1524, 1997.

[16] X.-C. Zhang, Y. Yin, and X. F. Ma, “Coherent measurement of THz optical rectification from electrooptic crystals,” *Appl. Phys. Lett.,* vol. 61, no. 23, pp. 2764-2766, 1992.

[17] A. Nahata, A. S. Weling, and T. F. Heinz, “A wideband coherent terahertz spectroscopy system using optical rectification and electro-optic sampling,” *Appl. Phys. Lett.,* vol. 69, no. 16, pp. 2321-2323, 1996.

[18] A. Bonvalet, M. Joffre, J. L. Martin, and A. Migus, “Generation of ultrabroadband femtosecond pulses in the midinfrared by optical rectification of 15 fs light-pulses at 100 MHz repetition rate,” *Appl. Phys. Lett.,* vol. 67, no. 20, pp. 2907-2909, 1995.

[19] M. van Exter and D. R. Grischkowsky, “Characterization of an optoelectronic terahertz beam system,” *IEEE Trans. Microwave Theory Tech*., vol. 38, no. 11, pp. 1684-1691, 1990.

[20] J. T. Darrow, B. B. Hu, X.-C. Zhang, and D. H. Auston, “Subpicosecond electromagnetic pulses from large-aperture photoconducting antennas,” *Opt. Lett*., vol. 15, no. 6, pp. 323-325, 1990.

[21] C. Weiss, R. Wallenstein, and R. Beigang, “Magnetic-field-enhanced generation of terahertz radiation in semiconductor surfaces,” *Appl. Phys. Lett*., vol. 77, no.25, pp. 4160-4162, 2000.

[22] D. S. Kim and D. S. Citrin, “Enhancement of terahertz radiation from photoconductors by elliptically focused excitation,” *Appl. Phys. Lett*., vol. 87, no. 6, pp. 061108, 2005.

[23] D. S. Kim and D. S. Citrin, “Coulomb and radiation screening in photoconductive terahertz sources,” *Appl. Phys. Lett*., vol. 88, no. 16, pp. 161117–3, Apr. 2006.

[24] J. K. Wahlstrand, H. Zhang, and S. T. Cundiff, “Uniform-field transverse electroreflectance using a mode-locked laser and a radio-frequency bias,” *Appl. Phys. Lett.*, vol. 96, no. 10, pp. 101104, 2010.

[25] E. Dupont, P. B. Corkum, H. C. Liu, M. Buchanan, and Z. R. Wasilewski, “Phase-Controlled Currents in Semiconductors,” *Phys. Rev. Lett.*, vol. 74, no. 18, pp. 3596, May 1995.

[26] R. Atanasov, A. Hache, J. L. P. Hughes, H. M. van Driel, and J. E. Sipe, “Coherent Control of Photocurrent Generation in Bulk Semiconductors,” *Phys. Rev. Lett.*, vol. 76, no. 10, pp. 1703, Mar. 1996.

[27] A. Hache, Y. Kostoulas, R. Atanasov, J. L. P. Hughes, J. E. Sipe, and H. M. van Driel, “Observation of Coherently Controlled Photocurrent in Unbiased, Bulk GaAs,” *Phys. Rev. Lett.,* vol. 78, no. 2, pp. 306, Jan. 1997.

[28] A. Hache, J. E. Sipe, and H. M. van Driel, “Quantum interference control of electrical currents in GaAs,” *Quantum Electronics, IEEE Journal of*, vol. 34, no. 7, pp. 1144–1154, 1998.

[29] Y. Kerachian, P. A. Marsden, H. M. van Driel, and A. L. Smirl, “Dynamics of charge current gratings generated in GaAs by ultrafast quantum interference control,” *Phys. Rev. B*, vol. 75, no. 12, pp. 125205, Mar. 2007.

[30] H. Zhao, E. J. Loren, A. L. Smirl, and H. M. van Driel, “Dynamics of charge currents ballistically injected in GaAs by quantum interference,” *J. Appl. Phys.,* vol. 103, no. 5, pp. 053510–9, Mar. 2008.

[31] M. J. Stevens, A. L. Smirl, R. D. R. Bhat, A. Najmaie, J. E. Sipe, and H. M. van Driel, “Quantum Interference Control of Ballistic Pure Spin Currents in Semiconductors,” *Phys. Rev. Lett.*, vol. 90, no. 13, pp. 136603, Apr. 2003.

[32] P. Roos, X. Li, J. Pipis, and S. Cundiff, “Solid-state carrier-envelope-phase noise measurements with intrinsically balanced detection,” *Opt. Express*, vol. 12, no. 18, pp. 4255–4260, 2004.

[33] T. M. Fortier, P. A. Roos, D. J. Jones, S. T. Cundiff, R. D. R. Bhat, and J. E. Sipe, “Carrier-Envelope Phase-Controlled Quantum Interference of Injected Photocurrents in Semiconductors,” *Phys. Rev. Lett.*, vol. 92, no. 14, pp. 147403, Apr. 2004.

[34] P. A. Roos, X. Li, R. P. Smith, J. A. Pipis, T. M. Fortier, and S. T. Cundiff, “Solid-state carrier-envelope phase stabilization via quantum interference control of injected photocurrents,” *Opt. Lett.*, vol. 30, no. 7, pp. 735–737, 2005.

[35] R. P. Smith, P. A. Roos, J. K. Wahlstrand, J. A. Pipis, M. B. Rivas, and S. T. Cundiff, “Optical Frequency Metrology of an Iodine-Stabilized He-Ne Laser Using the Frequency Comb of a Quantum-Interference-Stabilized Mode-Locked Laser,” *Journal of Research of the National Institute of Standards and Technology*, vol. 112, pp. 289–296, 2007.

[36] J. M. Fraser, A. I. Shkrebtii, J. E. Sipe, and H. M. van Driel, “Quantum Interference in Electron-Hole Generation in Noncentrosymmetric Semiconductors,” *Phys. Rev. Lett.*, vol. 83, no. 20, pp. 4192, Nov. 1999.

[37] J. M. Fraser and H. M. van Driel, “Quantum interference control of free-carrier density in GaAs,” *Phys. Rev. B*, vol. 68, no. 8, pp. 085208, 2003.

[38] C. Van Hoof, K. Deneffe, J. De Boeck, D. J. Arent, and G. Borghs, “Franz--Keldysh oscillations originating from a well-controlled electric field in the GaAs depletion region,” *Appl. Phys. Lett.*, vol. 54, no. 7, pp. 608–610, Feb. 1989.

[39] R. A. Forman, D. E. Aspnes, and M. Cardona, “Transverse electroreflectance in semi-insulating silicon and gallium arsenide,” *Journal of Physics and Chemistry of Solids*, vol. 31, no. 2, pp. 227–246, Feb. 1970.

[40] D. S. Kyser and V. Rehn, “Piezoelectric effects in electroreflectance,” *Solid State Communications*, vol. 8, no. 18, pp. 1437–1441, Sep. 1970.

[41] M. Ruff, D. Streb, S. U. Dankowski, S. Tautz, P. Kiesel, B. Knupfer, M. Kneissl, N. Linder, G. H. Dohler, and U. D. Keil, “Polarization dependence of the electroabsorption in low-temperature grown GaAs for above band-gap energies,” *Appl. Phys. Lett.*, vol. 68, no. 21, pp. 2968–2970, May 1996.

[42] N. Katzenellenbogen and D. Grischkowsky, “Efficient generation of 380 fs pulses of THz radiation by ultrafast laser pulse excitation of a biased metal-semiconductor interface,” *Appl. Phys. Lett.*, vol. 58, no. 3, pp. 222-224, 1991.

[43] D. S. Kim and D. S. Citrin, “Efficient terahertz generation using trap-enhanced fields in semi-insulating photoconductors by spatially broadened excitation,” *J. Appl. Phys.*, vol. 101, no. 5, p. 053105–8, Mar. 2007.

[44] J. Santana and B. K. Jones, “Semi-insulating GaAs as a relaxation semiconductor,” *J. Appl. Phys.*, vol. 83, no. 12, pp. 7699–7705, Jun. 1998.

[45] O. A. Ryabushkin, E. I. Lonskaya, A. E. Sotnikov, and M. A. Chernikov, “Novel modulation reflectance spectroscopy of semiconductor heterostructures,” *physica status solidi (a)*, vol. 202, no. 7, pp. 1282–1291, 2005.

[46] D. E. Aspnes, “Electric-Field Effects on Optical Absorption near Thresholds in Solids,” *Phys. Rev.*, vol. 147, no. 2, p. 554, Jul. 1966.

[47] D. E. Aspnes, “Electric Field Effects on the Dielectric Constant of Solids,” *Phys. Rev.*, vol. 153, no. 3, p. 972, Jan. 1967.

[48] D. E. Aspnes and J. E. Rowe, “Resonant Nonlinear Optical Susceptibility: Electroreflectance in the Low-Field Limit,” *Phys. Rev. B*, vol. 5, no. 10, p. 4022, May 1972.

[49] H. Shen and M. Dutta, “Franz--Keldysh oscillations in modulation spectroscopy,” *J. Appl. Phys.*, vol. 78, no. 4, pp. 2151–2176, 1995.

[50] K. Tharmalingam, “Optical Absorption in the Presence of a Uniform Field,” *Phys. Rev.*, vol. 130, no. 6, p. 2204, Jun. 1963.

[51] J. Callaway, “Optical Absorption in an Electric Field,” *Phys. Rev.*, vol. 134, no. 4A, p. A998, May 1964.

[52] D. E. Aspnes, *Handbook of Semiconductors*, edited by T. S. Moss, North-Holland, Amsterdam, 1980.

[53] J. Hader, N. Linder, and G. H. Dohler, “k.p theory of the Franz-Keldysh effect,” *Phys. Rev. B*, vol. 55, no. 11, pp. 6960, Mar. 1997.

[54] K. Reimann, “Table-top sources of ultrashort THz pulses,” *Reports on Progress in Physics*, vol. 70, no. 10, pp. 1597–1632, 2007.

[55] Daniel M. Mittleman and R. Alan Cheville, “Terahertz Generation and Applications”.

[56] C. Winnewisser, P. Uhd Jepsen, M. Schall, V. Schyja, and H. Helm, “Electro optic detection of THz radiation in LiTaO3 LiNbO3 and ZnTe,” *Appl. Phys. Lett.*, vol. 70, no. 23, pp. 3069-3071, 1997.

[57] G. Gallot and D. Grischkowsky, “Electro-optic detection of terahertz radiation,” *J. Opt. Soc. Am. B*, vol. 16, no. 8, pp. 1204–1212, 1999.

[58] J. H. Kim, A. Polley, and S. E. Ralph, “Efficient photoconductive terahertz source using line excitation,” *Opt. Lett.*, vol. 30, no. 18, pp. 2490–2492, 2005.

[59] G. Zhao, R. N. Schouten, N. van der Valk, W. T. Wenckebach, and P. C. M. Planken, “Design and performance of a THz emission and detection setup based on a semi-insulating GaAs emitter,” *Rev. Sci. Instrum.*, vol. 73, no. 4, pp. 1715–1719, Apr. 2002.

[60] A. Dreyhaupt, S. Winnerl, T. Dekorsy, and M. Helm, “High-intensity terahertz radiation from a microstructured large-area photoconductor,” *Appl. Phys. Lett.*, vol. 86, no. 12, p. 121114–121114–3, Mar. 2005.

[61] B. B. Hu, E. A. de Souza, W. H. Knox, J. E. Cunningham, M. C. Nuss, A. V. Kuznetsov, and S. L. Chuang, “Identifying the Distinct Phases of Carrier Transport in Semiconductors with 10 fs Resolution,” *Phys. Rev. Lett.*, vol. 74, no. 9, p. 1689, Feb. 1995.

[62] G. Rodriguez and A. J. Taylor, “Screening of the bias field in terahertz generation from photoconductors,” *Opt. Lett.*, vol. 21, no. 14, pp. 1046–1048, Jul. 1996.

[63] G. S. Smith, *An introduction to classical electromagnetic radiation,* Cambridge University Press, Cambridge, 1990, pp 358-378

[64] J. Zhang, Y. Hong, S.L. Braunstein and K.A. Shore, “Terahertz pulse generation and detection with LT GaAs photoconductive antenna,” *IEE Proc.-Optoelectron*, vol. 151, no. 2, pp. 98-101, 2004.

[65] D. A. Turton, G. H. Welsh, J. J. Carey, G. D. Reid, G. S. Beddard, and K. Wynne, “Alternating high-voltage biasing for terahertz large-area photoconductive emitters,” *Rev. Sci. Instrum.*, vol. 77, no. 8, pp. 083111–5, 2006.

[66] Gregor Segschneider, Frank Jacob, Torsten Lo¨ffler, and Hartmut G. Roskos, “Free-carrier dynamics in low-temperature-grown GaAs at high excitation densities investigated by time-domain terahertz spectroscopy,” *Phys. Rev. B*, vol. 65, no. 12, pp. 125205, 2002.

[67] R. D. R. Bhat and J. E. Sipe, “Optically Injected Spin Currents in Semiconductors,” *Phys. Rev. Lett.*, vol. 85, no. 25, p. 5432, Dec. 2000.

[68] M. J. Stevens, R. D. R. Bhat, J. E. Sipe, H. M. van Driel, and A. L. Smirl, “Coherent control of carrier population and spin in (111)-GaAs,” *physica status solidi (b)*, vol. 238, no. 3, pp. 568–574, 2003.

[69] J. K. Wahlstrand, J. A. Pipis, P. A. Roos, S. T. Cundiff, and R. P. Smith, “Electrical measurement of carrier population modulation by two-color coherent control,” *Appl. Phys. Lett.*, vol. 89, no. 24, pp. 241115–3, Dec. 2006.

[70] C. H. Lee, R. K. Chang, and N. Bloembergen, “Nonlinear Electroreflectance in Silicon and Silver,” *Phys. Rev. Lett.*, vol 18, pp. 167, 1967.

[71] J. K. Wahlstrand, H. Zhang, S. B. Choi, S. Kannan, D. S. Dessau, J. E. Sipe, and S. T. Cundiff, “Optical Coherent Control Induced by an Electric Field in a

Semiconductor: A New Manifestation of the Franz-Keldysh Effect," *Phys. Rev. Lett.*, vol. 106, no. 24, p. 247404, Jun. 2011.

[72] Y. H. Lee, A. Chavez-Pirson, S. W. Koch, H. M. Gibbs, S. H. Park, J. Morhange, A. Jeffery, N. Peyghambarian, L. Banyai, A. C. Gossard, and W. Wiegmann, "Room-Temperature Optical Nonlinearities in GaAs," *Phys. Rev. Lett.*, vol. 57, no. 19, p. 2446, Nov. 1986.

[73] M. J. Stevens, R. D. R. Bhat, X. Y. Pan, H. M. van Driel, J. E. Sipe, and A. L. Smirl, "Enhanced coherent control of carrier and spin density in a zinc-blende semiconductor by cascaded second-harmonic generation," *J. Appl. Phys.*, vol. 97, no. 9, pp. 093709–7, May 2005.

[74] J. K. Wahlstrand and J. E. Sipe, "Independent-particle theory of the Franz-Keldysh effect including interband coupling: Application to calculation of electroabsorption in GaAs," *Phys. Rev. B*, vol. 82, no. 7, p. 075206, 2010.

[75] N. Laman, A. I. Shkrebtii, J. E. Sipe, and H. M. van Driel, "Quantum interference control of currents in CdSe with a single optical beam," *Appl. Phys. Lett.*, vol. 75, no. 17, pp. 2581–2583, Oct. 1999.

[76] R. L. Snider, J. K. Wahlstrand, H. Zhang, R. P. Mirin, and S. T. Cundiff, "Quantum interference control of photocurrent injection in Er-doped GaAs," *Applied Physics B: Lasers and Optics*, vol. 98, no. 2, pp. 333–336, Feb. 2010.

[77] P. A. Roos, X. Li, J. A. Pipis, T. M. Fortier, S. T. Cundiff, R. D. R. Bhat, and J. E. Sipe, "Characterization of carrier-envelope phase-sensitive photocurrent injection in a semiconductor," *J. Opt. Soc. Am. B*, vol. 22, no. 2, pp. 362–368, 2005.

[78] P. Roos, Q. Quraishi, S. Cundiff, R. Bhat, and J. Sipe, "Characterization of quantum interference control of injected currents in LT-GaAs for carrier-envelope phase measurements," *Opt. Express*, vol. 11, no. 17, pp. 2081–2090, 2003.

[79] R. D. R. Bhat and J. E. Sipe, "Excitonic effects on the two-color coherent control of interband transitions in bulk semiconductors," *Phys. Rev. B*, vol. 72, no. 7, p. 075205–14, 2005.

[80] S. Gupta, S. Sethi, and P. K. Bhattacharya, "Picosecond carrier lifetime in erbium-doped-GaAs," *Appl. Phys. Lett.*, vol. 62, no. 10, pp. 1128–1130, Mar. 1993.

[81] S. Gupta, M. Y. Frankel, J. A. Valdmanis, J. F. Whitaker, G. A. Mourou, F. W. Smith, and A. R. Calawa, "Subpicosecond carrier lifetime in GaAs grown by molecular beam epitaxy at low temperatures," *Appl. Phys. Lett.*, vol. 59, no. 25, pp. 3276–3278, Dec. 1991.

[82] R. L. Tober and J. D. Bruno, “Modulation effects near the GaAs absorption edge,” *J. Appl. Phys.*, vol. 68, no. 12, pp. 6388–6392, Dec. 1990.

[83] A. Jaeger and G. Weiser, “Excitonic electroabsorption spectra and Franz-Keldysh effect of In0.53Ga0.47As/InP studied by small modulation of static fields,” *Phys. Rev. B*, vol. 58, no. 16, p. 10674, Oct. 1998.

[84] L. Costa, M. Betz, M. Spasenovic, A. D. Bristow, and H. M. van Driel, “All-optical injection of ballistic electrical currents in unbiased silicon,” *Nat Phys*, vol. 3, no. 9, pp. 632–635, 2007.

[85] J. K. Wahlstrand, S. T. Cundiff, and J. E. Sipe, “Polarization dependence of the two-photon Franz-Keldysh effect,” *Phys. Rev. B*, vol. 83, no. 23, p. 233201, Jun. 2011.

Appendix A

RF bias and detection setup details

In this appendix the experimental details of the radio frequency (RF) bias and detection are provided.

A.1 The RF setup

Here we present a brief overview of the RF bias components and setup procedure. A schematic configuration of the RF bias and detection apparatus is shown in Figure A.1.

(1) Start with picking up the laser pulse train signal by a high speed photodetector PD1 (QQ062A2, designed by JILA electronics shop). The signal can be monitored by connecting the photodetector output to a RF spectrum analyzer.

(2) Amplify the output of PD1 using a RF amplifier AMP1 (Mini-Circuits ZFL-500 HLN or a similar product)

(3) Send PD1 output to a RF powersplitter PS1 (Mini-Circuits powersplitter ZSC-2-1). The PD1 output is split into two parts, part 1 is used to generate the RF bias across the sample and part 2 is used to generate a reference frequency for lock-in detection.

(4) Send part 1 of the pulse train signal through a band pass filter BP1 (K&L tunable band pass filter 5BT-250/500-5, 5 MHz bandwidth), which only selects the third order harmonic $3f_{\mathrm{rep}}$ of the laser repetition rate.

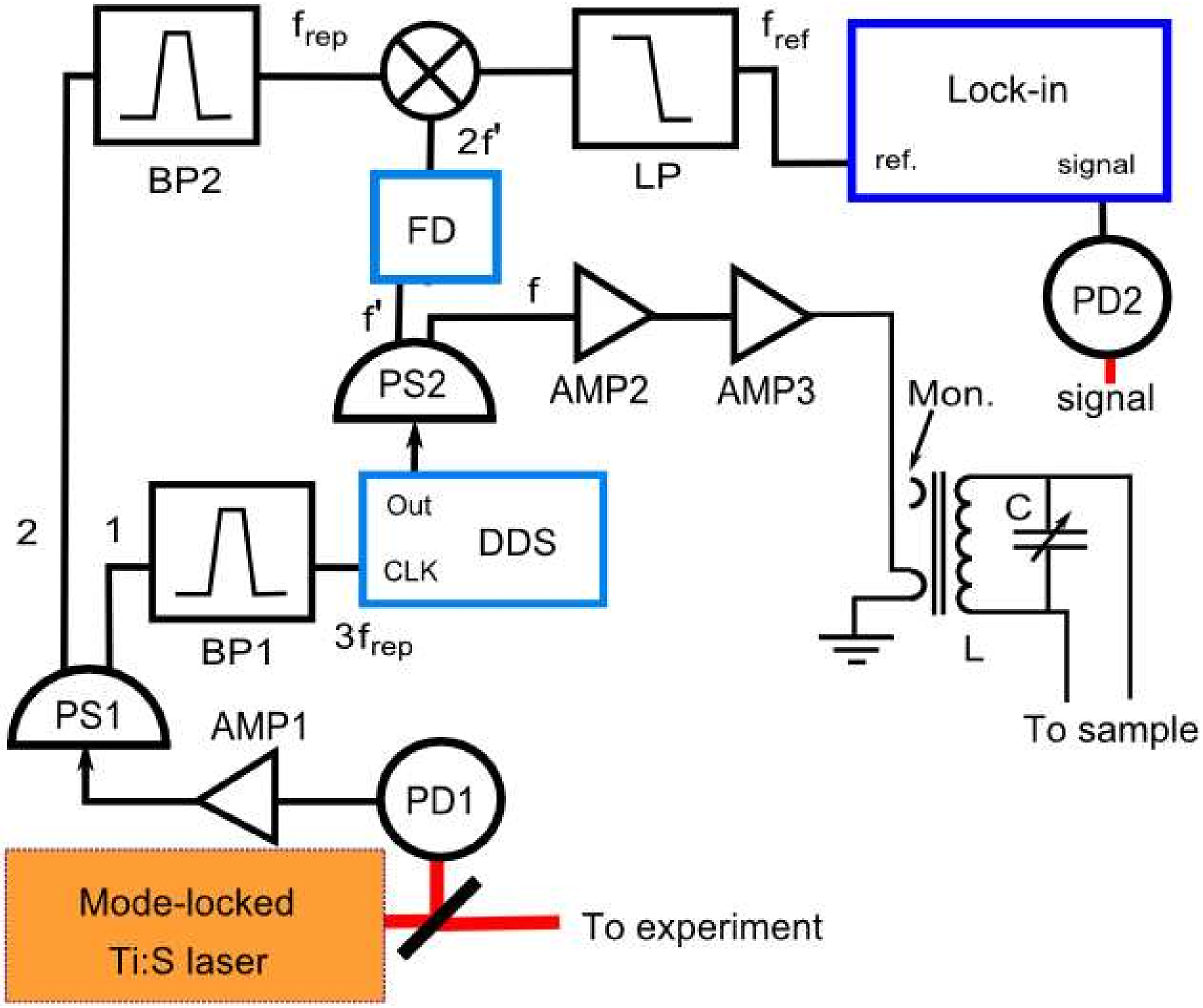

Figure A.1: Schematic configuration of RF bias and detection setup. BP: band pass filter, PD: photodetector, PS: powersplitter, AMP: RF amplifier, FD: frequency doubler (only for ER experiment), LP: low pass filter.

(5) Then use the $3f_{rep}$ signal as the clock signal (CLK input) of the direct digital synthesizer (DDS), and make sure the $3f_{rep}$ signal has amplitude

around 0 dBm by adding RF amplifiers or attenuators. See Section A.2 for DDS software control information.

(6) Split the DDS output into two by another powersplitter PS2, here the frequency is $f' = f_{rep} + 1$ kHz (or $\frac{1}{2}f_{rep}$ + 1kHz for ER). Send f' through RF amplifier AMP2 (Mini-Circuits ZFL-500 HLN) first and adjust the amplitude of f to be around 0 dBm by adding attenuators if necessary. Then the output of AMP2 is sent into another amplifier AMP3 (Mini-Circuits ZHL-1-2W, with 29 dBm gain and 2W maximum output power). Here make sure the amplitude of AMP2 output doesn't exceed 0 dBm to avoid potentially damaging the high power amplifier AMP3.

(7) The amplified output signal of AMP3 is used to drive the LC resonance circuit which amplifies the signal further, producing the high voltage RF across the sample. The capacitor used here is a sealed glass variable capacitor (TM90M), and the inductor is the secondary coil of an air-core transformer consisting of 22 turns of 20 gauge magnet wire wound on a toroid (Micrometal Inc. T50-0 for 76 MHz and 89 MHz, and T50-17 for 44.5 MHz).

(8) Back to part 2 of the output of PS1, send the signal through another band pass filter BP2 (K&L tunable band pass filter 5BT-63/125-5, 5 MHz bandwidth) and select the laser repetition rate f_{rep} this time, set f_{rep} to be one of the two inputs (labeled 'L' or 'R') of a frequency mixer (Mini-Circuits ZAD-1).

(9) From the output of PS2, $f' = f_{rep} + 1$ kHz (or $\frac{1}{2}f_{rep}$ + 1kHz for ER) is then set to be the other input of the mixer. For ER experiment which uses or $\frac{1}{2}f_{rep}$ + 1kHz for RF bias frequency, double f' using a frequency doubler FD (MiniCircuits FD-2+), for other experiments FD is not required. The output of the mixer (labeled 'I') after a low pass filter LP (MiniCircuits

BLP-5) is set as the reference frequency for lock-in detection, here f_{ref} = 1 kHz (or 2 kHz for ER).

A.2 DDS software control

The DDS we use in our experiments is an AD9854 CMOS 300 MSPS Quadrature DDS customer evaluation board made by Analog Devices, Inc. The circuit can be controlled using the AD9854 customer evaluation software which is available on the manufacturer's website.

(1) Connect the DDS circuit board to a computer with the AD9854 software installed and start the program, first checking the parallel port connection by selecting 'Parallel Port' -> 'Check Parallel Port Connection'. Always make sure the selected parallel port is properly connected to a DDS evaluation board.

(2) Click 'Clock and Amplitude' button as shown in Figure A.2. Type in a reference clock frequency first (the clock frequency needs to be three times the output frequency, i.e., 267 MHz clock frequency for an output around 89 MHz), hit 'Enter' button on the keyboard (every number typed in here needs to hit 'Enter' to make it valid), and choose 'Send CLK Info To DUT'. Then select output amplitude to be 'Output amplitude is always full scale' and click 'Send Amplitude Scaling Info To DUT'. One can also adjust the RF bias amplitude by choosing 'Output amplitude is programmable' and enter three hexadecimal numbers in 'Q-Channel Multiplier'. The last step is to uncheck the 'Comparator Power Down' in the 'Power Down' box, then click 'Send Control Info To DUT'.

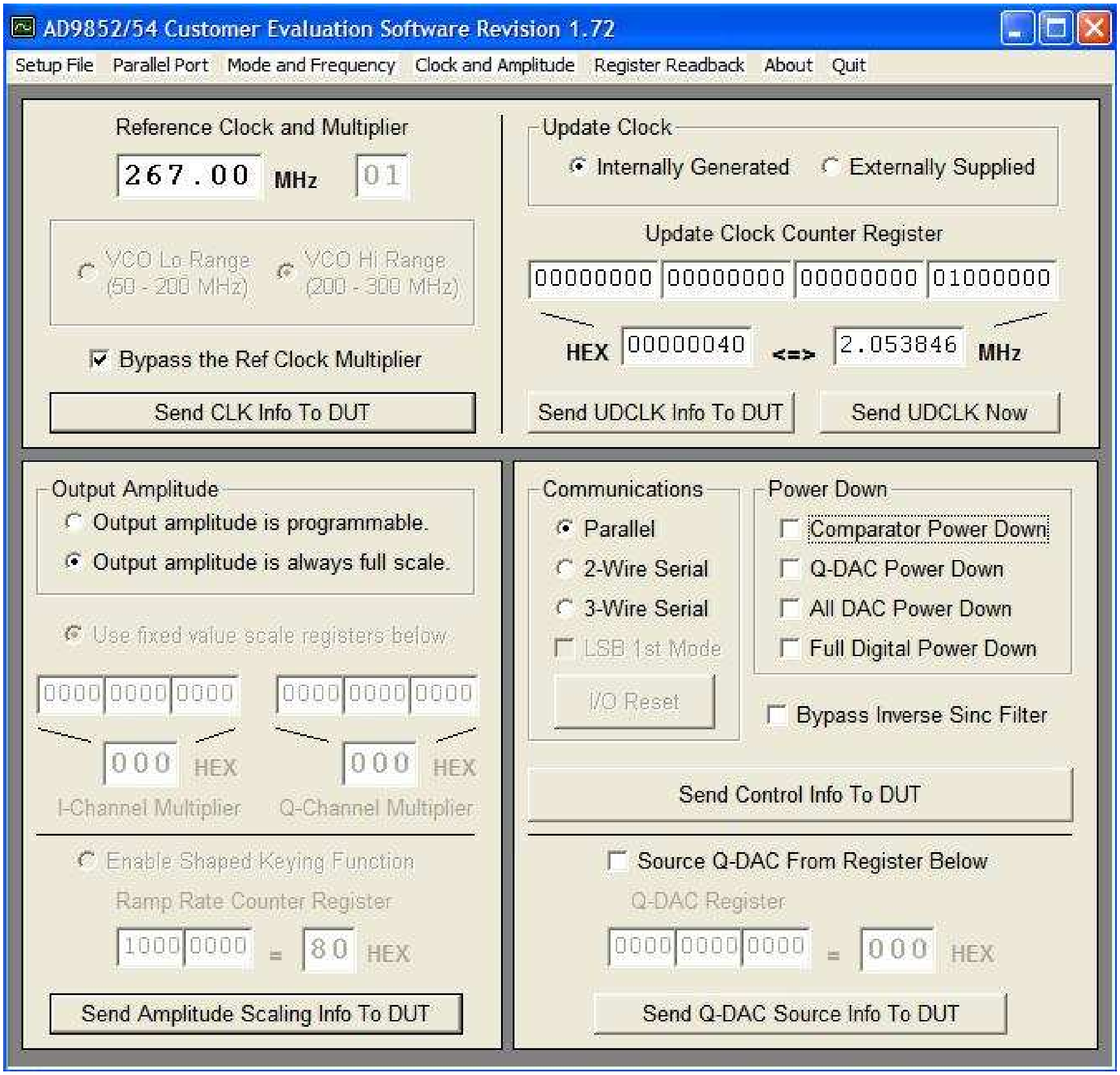

AD9852/54 Customer Evaluation Software Revision 1.72

Reference Clock and Multiplier
267.00 MHz 01
○ VCO Lo Range (50 - 200 MHz)
● VCO Hi Range (200 - 300 MHz)
☑ Bypass the Ref Clock Multiplier

Update Clock
● Internally Generated
○ Externally Supplied
Update Clock Counter Register
00000000 00000000 00000000 01000000
HEX 00000040 <=> 2.053846 MHz

Output Amplitude
○ Output amplitude is programmable.
● Output amplitude is always full scale.
● Use fixed value scale registers below
0000 0000 0000 = 000 HEX I-Channel Multiplier
0000 0000 0000 = 000 HEX Q-Channel Multiplier
○ Enable Shaped Keying Function
Ramp Rate Counter Register
1000 0000 = 80 HEX

Communications
● Parallel
○ 2-Wire Serial
○ 3-Wire Serial
☐ LSB 1st Mode

Power Down
☐ Comparator Power Down
☐ Q-DAC Power Down
☐ All DAC Power Down
☐ Full Digital Power Down
☐ Bypass Inverse Sinc Filter

☐ Source Q-DAC From Register Below
Q-DAC Register
0000 0000 0000 = 000 HEX

Figure A.2: Clock and amplitude control

(3) Click ‘Mode and Frequency’ button and enter 44.501 MHz for ER, or 89.001 MHz for THz generation, or 76.000 MHz for coherent control, as shown in Figure A.3. The phase of DDS output signal can also be adjusted with respect to the DDS clock signal, by typing in four

hexadecimal numbers in ‘Phase Adjust #1’ box. The final step is to click ‘Send Mode, Frequency, Phase Info to DUT’ button.

More detailed information about the DDS circuits can be found in AD9854 DDS user’s manual.

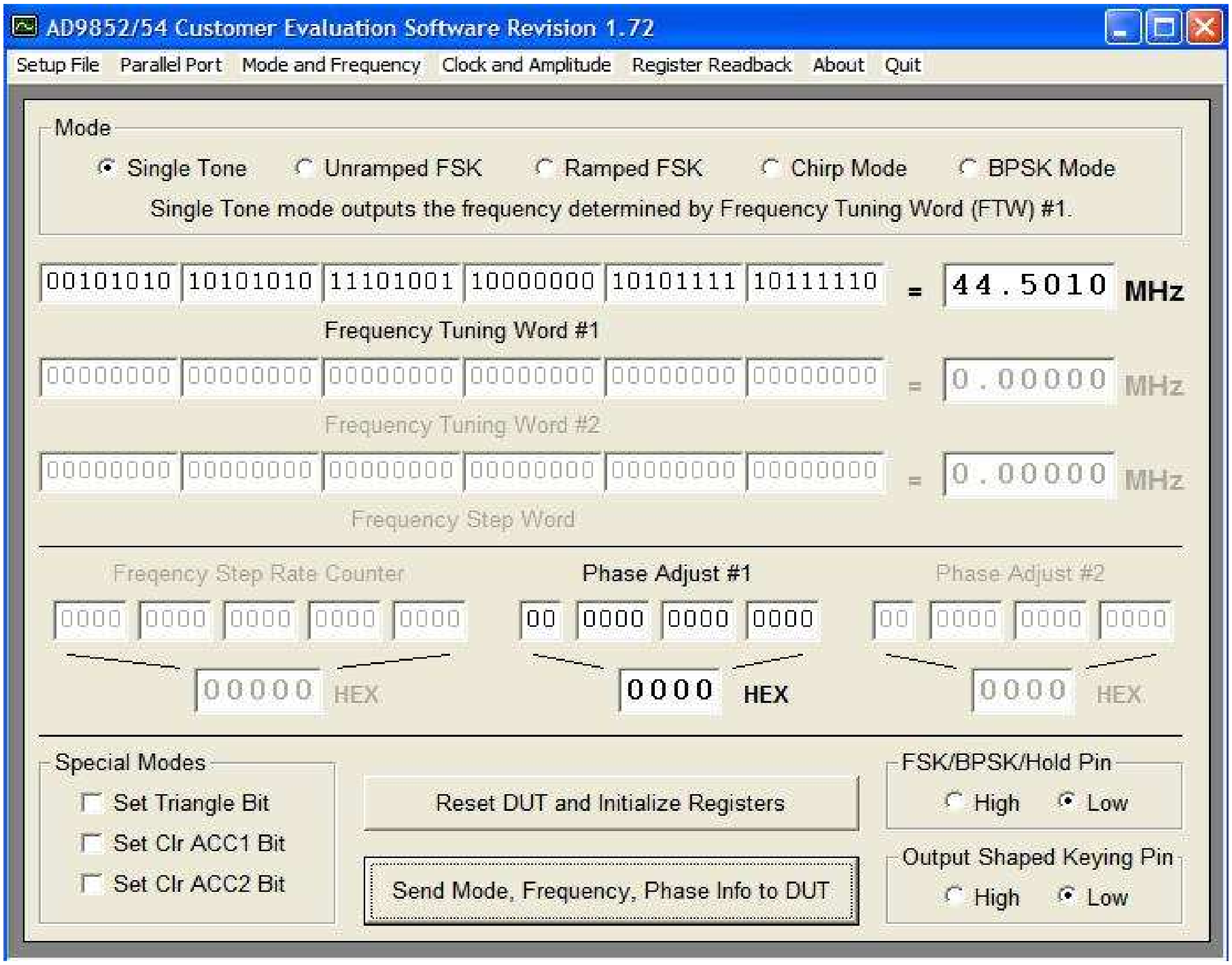

Mode

● Single Tone ○ Unramped FSK ○ Ramped FSK ○ Chirp Mode ○ BPSK Mode

Single Tone mode outputs the frequency determined by Frequency Tuning Word (FTW) #1.

00101010 10101010 11101001 10000000 10101111 10111110 = 44.5010 MHz

Frequency Tuning Word #1

00000000 00000000 00000000 00000000 00000000 00000000 = 0.00000 MHz

Frequency Tuning Word #2

00000000 00000000 00000000 00000000 00000000 00000000 = 0.00000 MHz

Frequency Step Word

Freqency Step Rate Counter: 0000 0000 0000 0000 0000 — 00000 HEX

Phase Adjust #1: 00 0000 0000 0000 — 0000 HEX

Phase Adjust #2: 00 0000 0000 0000 — 0000 HEX

Special Modes

☐ Set Triangle Bit

☐ Set Clr ACC1 Bit

☐ Set Clr ACC2 Bit

FSK/BPSK/Hold Pin: ○ High ● Low

Output Shaped Keying Pin: ○ High ● Low

Figure A.3: Mode and frequency control.

Appendix B

Photolithography for metal electrodes

In this appendix the patterning of metal electrodes by photolithography is described. We use negative photoresist NR7-1500PY.

(10) Clean the sample substrate with acetone and deionized (DI) water. Bake the sample on a hot plate at $150\,^{0}C$ for 15 minutes; this helps remove water from the sample surface.

(11) Place the substrate on the spin coater, put a few drops of the negative photoresist on the sample surface, and set the spin to be 3000 rpm for 40 seconds.

(12) Prebake the sample with photoresist on the hot plate for 90 seconds at $150\,^{0}C$.

(13) Start the photolithography machine (Karl Suss, Mode MJB-3) in the following order: a) turn on the main power supply; b) turn the two switches on for compressed gas; c) turn on the lamp power supply; d) hit the ‘power’ button on the control panel.

(14) Put the photomask on the holder of the lithography machine with its coating side down and push the ‘vacuum mask’ button on the control panel.

(15) Place the substrate on the sample plate of the photolithography machine; turn the z knob clockwise first, to lower the sample plate in order to prevent the sample from crushing against the mask. Align the

position of the sample with respect to the mask by adjusting the two knobs that control x and y direction of the sample plate.

(16) Pull the lever on the left side of the photolithography machine clockwise. Adjust the z knob counterclockwise to make contact between the mask and the sample surface. Slowly and carefully raise the sample up until some interference fringes can be seen on the sample surface. This indicates a good contact between the sample and the mask.

(17) Push the lever on the left side of the photolithography machine counterclockwise until the contact indicator on the control panel is on. Adjust the exposure time to be 30 seconds, hit the 'exposure' button.

(18) After exposure, lower the sample plate using the z knob and take the sample out. Turn off the photolithography machine in reverse order of the procedure in (4).

(19) Postbake the sample with the hot plate for 90 seconds at $100\,^{0}C$.

(20) Dip the sample in MF-CD-26 developer for 2~5 seconds, then rinse with DI water and check the pattern under a microscope.

(21) After metal deposition (done by David Alchenberger in the Keck Lab), soak the sample in acetone for about 15 minutes to lift off the exposed part, rinse with DI water again, and check the pattern under a microscope.

Appendix C

Thin GaAs sample preparation

In this appendix the preparation of the 1 μm thick GaAs sample is described. The sample consists of a 1 μm thick, undoped GaAs epilayer grown on top of a semi-insulating GaAs substrate by molecular beam epitaxy. The epilayer and the substrate are separated by a thin AlGaAs stop-etching layer roughly 100 nm thick.

C.1 Mechanical lapping

(22) Attach the polished surface of the sample to a ½ inch transparent sapphire disk (made by Meller Optics, Inc.) by either clear wax or optical epoxy (Norland Optical Adhesive 81). The optical epoxy requires UV cure for one or two hours.

(23) Thin the sample down to a few microns thick by using the lapping tool (as shown in Figure C.1, it helps thin the sample by a fixed amount by adjusting the screw on top) and the lapping paper (Precision Surfaces International, PSI-1612-11 lapping film sheets), which is like sand paper with a very fine grit.

C.2 Wet etching (gloves and safety glasses required)

(1) Get 100~200 mL of hydrogen peroxide (H_2O_2) solution from the fridge in Keck lab.

(2) Get 10~15 mL ammonium hydroxide (NH_3:OH) from the flammable cabinet in Keck lab.

Figure C.1: The lapping tool.

(3) Prepare two beakers and rinse them with DI water first. Then fill one of them with DI water, and use it to rinse the pH probe and the neutral solution flask (remove the neutral solution bottle from the flask first) of the pH meter (Fisher Scientific, Accumet Model 20) in the Keck lab until the reading of the pH meter is stabilized around 7.

(4) Add 100~200 mL H_2O_2 solution to the other beaker, put the probe and the neutral solution flask into the beaker until the reading of the pH meter is stable.

(5) Use a pipette to add NH_3:OH solution into the H_2O_2 solution slowly. Add a few drops each time, shake the beaker slowly and wait until the reading of the pH meter is stable. Keep adding NH_3:OH solution until the pH value of the solution reaches around 8.1.

(6) Store the solution in a Nalgene bottle for transportation (the wet etching process needs to be performed in a fume hood in a different room), and lightly cover the bottle (gas may be produced and needs a way to escape the bottle to avoid building up pressure).

(7) Clean the probe and the flask using DI water, and reattach the neutral solution bottle to the flask.

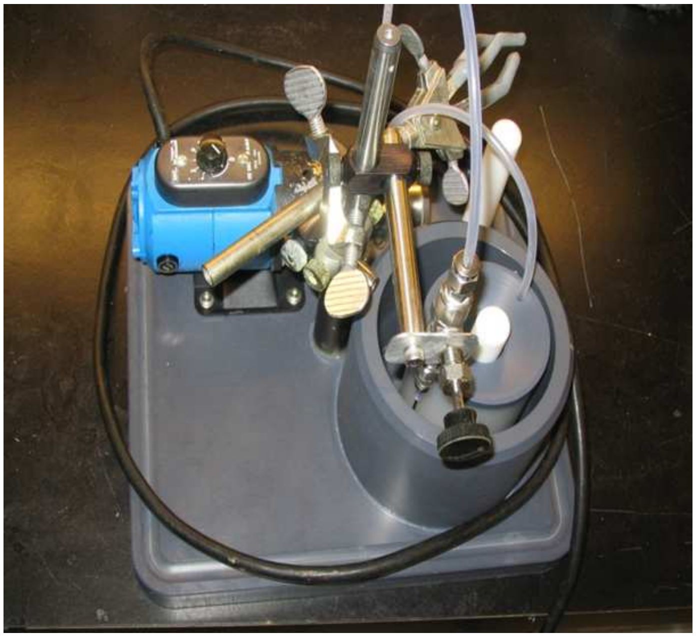

Figure C.2: The wet etching tool.

(8) In a fume hood, pour the etchant solution into the etchant container of our etching tool (shown in Figure C.2), and put ice around the etchant

container to keep the temperature low. Fix the sample on the sample holder, point the syringe needle towards the sample and start etching until the AlGaAs stop-etching layer is reached.

(9) Rinse the sample, clean the etching tool, label the used etchant as hazardous waste and store in the Satellite Accumulation Area.